3-D Unsteady Simulation of a Modern High Pressure Turbine Stage: Analysis of Heat Transfer and Flow

Dissertation

Presented in Partial Fulfillment of the Requirements for the Degree of Doctor of Philosophy in the Graduate School of The Ohio State University

By

Vikram Shyam, M.S.
Graduate Program in Aerospace Engineering

The Ohio State University

2010

Dissertation Committee:

Jen-Ping Chen, Advisor

Ali A. Ameri

Meyer J. Benzakein

Jeffrey P. Bons

Henry R. Busby

Copyright by

Vikram Shyam

2010

Abstract

This is the first 3-D unsteady RANS simulation of a highly loaded transonic turbine stage and results are compared to steady calculations and experiments. A low Reynolds number k-ε turbulence model is employed to provide closure for the RANS system. Phase-lag is used in the tangential direction to account for stator-rotor interaction. Due to the highly loaded characteristics of the stage, inviscid effects dominate the flowfield downstream of the rotor leading edge minimizing the effect of segregation to the leading edge region of the rotor blade. Unsteadiness was observed at the tip surface that results in intermittent 'hot spots'. It is demonstrated that unsteadiness in the tip gap is governed by both inviscid and viscous effects due to shock-boundary layer interaction and is not heavily dependent on pressure ratio across the tip gap. This is contrary to published observations that have primarily dealt with subsonic tip flows. The high relative Mach numbers in the tip gap lead to a choking of the leakage flow that translates to a relative attenuation of losses at higher loading. The efficacy of a new tip geometry is discussed to minimize heat flux at the tip while maintaining choked conditions. Simulated heat flux and pressure on the blade and hub agree favorably with experiment and literature. The time-averaged simulation provides a more conservative estimate of heat flux than the steady simulation. The shock structure formed due to stator-rotor interaction is analyzed. A preprocessor has

also been developed as a conduit between the unstructured multi-block grid generation software GridPro and the CFD code TURBO.

Dedication

Dedicated to P,D and E who are aptly named....

Acknowledgments

I thank Dr. Ali Ameri and Dr. Jen-Ping Chen for their tireless efforts to guide me through this process. I am also grateful to Dr. James Heidmann of NASA Glenn Research Center, Dr. Meyer Benzakein of The Ohio State University and to AVETEC for funding various segments of this research effort. I acknowledge Dr. Wai-Ming To of The University of Toledo, Mr. Robert Boyle and Dr. Mark Celestina of the NASA Glenn Research Center for their numerous useful insights and discussions. The simulations and post processing described and presented in this work were performed at The Ohio Super Computing Center and NASA Glenn research center. I acknowledge the time and effort of the members of my committee Dr. Ali Ameri, Dr. Jeffrey Bons, Dr. Meyer Benzakein, Dr. Henry Busby and Dr. Jen-Ping Chen, my advisor. Finally, I would like to recognize the early guidance given to me by Dr. Michael Foster and Dr. James Scott (professors emeriti, The Ohio State University).

Vita

May 1999...................D.A.V. Senior Secondary School, Madras, India

2002...........................Intern, General Electric Aircraft Engines, Evendale, OH

2003...........................B.S. Aerospace Engineering, The Ohio State University

2003 to 2005..............Graduate fellow, Aerospace Engineering, The Ohio State University

2005...........................M.S. Aerospace Engineering, The Ohio State University

2006 to present..........Coop, NASA Glenn Research Center, Cleveland, OH

Publications

Shyam, V., Foster M., R., "The Effect Of Rapid Rotation On A Vertical Bridgman Furnace At Large Rayleigh Number", Journal of Mechanics and Applied Mathematics, May 2007

Fields of Study

Major Field: Aerospace Engineering

Table of Contents

List of Tables

List of Figures

Nomenclature

C_P	specific heat capacity at constant pressure
ρ	density
h	heat transfer coefficient
q	rate of heat flux
k	conductivity
T	temperature
P	pressure
n	distance normal to wall or solid surface
$\Pr$	Prandtl number
μ	coefficient of viscosity
$\bar{a}$	normalized value of variable a (usually normalized by a_{ref})
ξ,η,ζ	computational coordinates
i	index of computational coordinate ξ

j	index of computational coordinate η
k	index of computational coordinate ζ
x,y,z	coordinates in physical space
k	turbulent kinetic energy
ω	specific dissipation
ε	turbulent dissipation
Ω	vorticity magnitude
$\vec{n}$	unit normal vector to surface
$\vec{V}$	velocity vector
γ	ratio of specific heats C_p/C_v
c	speed of sound
e	internal energy
w	work
C_f	skin friction coefficient
Nu	Nusselt number
d,D	diameter of film cooling hole

DR density ratio $\frac{\rho_c}{\rho_\infty}$

u axial velocity

L length of film cooling hole

M blowing ratio $\frac{\rho_c u_c}{\rho_\infty u_\infty}$

Tu turbulent intensity

VR jet to mainstream velocity ratio $\frac{u_c}{u_\infty}$

η film effectiveness $\eta = \frac{T_\infty - T_{aw}}{T_\infty - T_c}$

μ_T turbulent viscosity

θ dimensionless air temperature $\eta = \frac{T_\infty - T}{T_\infty - T_c}$

CFD Computational Fluid Dynamics

CFL Courant-Friedrichs-Lewy number

St Stanton Number

n normal distance from surface

P static pressure normalized by reference pressure

Re	Reynolds Number
S	normalized distance along blade surface at a given span, with S=0 at leading edge.
	Entropy
V	magnitude of velocity vector, $\vec{V}$
|*Z*|	absolute value of z-coordinate in blade to blade direction.
R	radius measured from axis of rotation.
$\Re$	Recovery factor
Δ	percent difference

Subscripts:

ref	Reference conditions
wall	at solid surface (no slip boundary)
phantom	cell center of phantom cell adjacent to boundary
inlet	Inlet to the rotor
steady	Refers to solution variables resulting from a steady simulation
time-averaged	Refers to solution variables obtained by time-averaging the results of an unsteady simulation

max	maximum value
min	minimum value
∞	free stream
c	coolant
aw	at adiabatic wall
w	at isothermal wall
in	cell center adjacent to boundary inside computational domain
x	derivative with respect to x
y	derivative with respect to y
z	derivative with respect to z

Chapter 1: Introduction

1.1 Importance of heat transfer prediction for turbine engine design

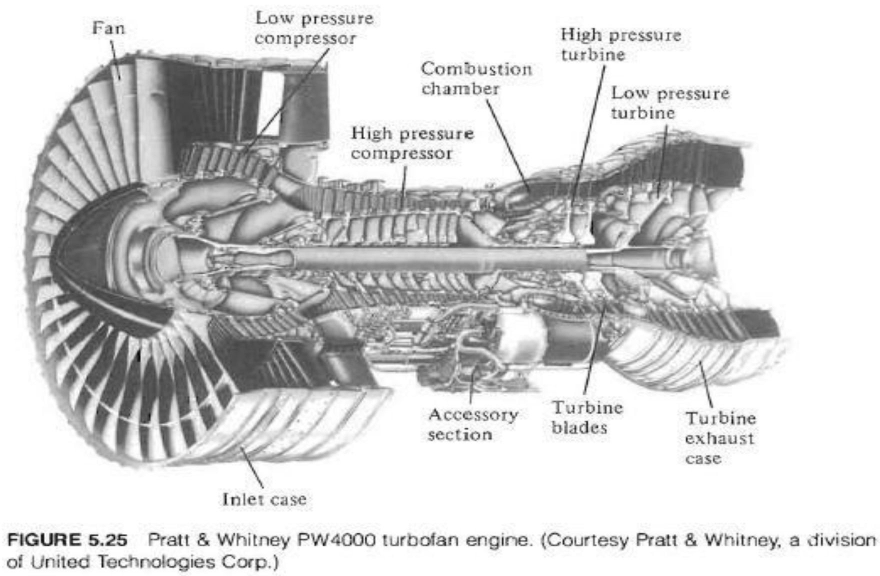

Figure 1.1 A modern Gas turbine engine [2]

A gas turbine engine is a device that converts the chemical energy of fuel to kinetic energy either to propel an aircraft or to generate electricity or perform work of some sort [1] [2]. A picture of a gas turbine engine is shown in figure 1.1 [2]. The components of a gas turbine engine operate at a higher efficiency than any system that occurs in nature [4] . It generates a large amount of power for its size and is therefore an excellent choice for propelling aircraft. The main components of an aircraft jet engine are the compressor, the combustor and the turbine. These are collectively known as the core. The compressor compresses the air entering the engine core and slows it down to a velocity that is amenable to combustion in the combustor. In the combustor, fuel is injected and mixed with the air and combusted. The high-energy combustion mixture passes through the turbine. Here it is accelerated to high velocity to produce thrust.

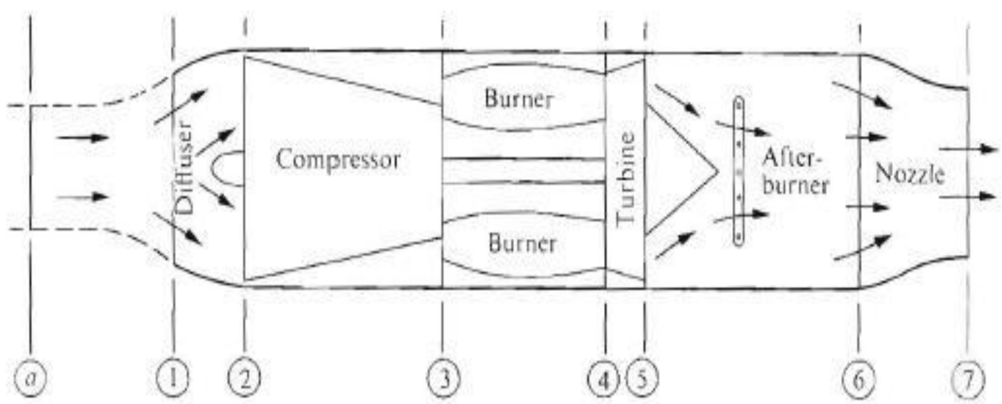

FIGURE 5.14 Schematic diagram of a turbojet engine.

Figure 1.2 Schematic of gas turbine engine showing components [2]

Figure 1.2 shows a sectioned view of the important components of a modern jet engine. Books such as [1], [2] and [3] provide detailed descriptions of the workings of jet engines and only a brief summary of basic concepts is provided here. The efficiency of a jet engine is linked to the turbine inlet temperature and it is for this reason that one of the aims of engine design is to maximize the turbine inlet temperature. The temperature at the exit of a modern jet engine combustor can reach values of approximately 2000K. This is well in excess of the thermal limits (approximately 1500K [1]) of materials used for stator vanes and rotor blades in the turbine section of the core. In order to operate at these high temperatures, typically at take-off, the turbine components are cooled by bleeding relatively cooler air from the compressor through holes in the surface of the turbine stators and rotors. The aerodynamics and heat transfer in the turbine stage are highly unsteady. This is due to several factors. First, the fluid exiting the combustor stage is not necessarily represented by a flat temperature profile. The combustor exit temperature profile is dependent on mixing in the combustor and can lead to thermal unsteadiness in the wake of the high pressure stator. Second, the relative motion of the rotor and the stator contributes to unsteadiness. The stator wakes are periodically chopped by the downstream rotors. If the flow is transonic, shock interactions may occur leading to secondary unsteady effects particularly near the leading edge of the rotors. These effects are further elaborated on in section 1.3. It is important to quantify and qualify the thermal load on the blades in order to efficiently and effectively cool them. Even a modest 10K rise in blade metal temperature can lead to a sharp decline in the longevity of the blade through thermal fatigue and creep (by approximately half [1]). Another significant concern in turbine rotors is aerodynamic loss due to tip leakage. This phenomenon occurs because the high pressure on the pressure side (concave) drives flow through the tip gap towards the low pressure suction side. In addition, the blade surface in the tip region is subjected to heating. This heating is thought to be largely dependent on blade geometry. Several authors have concluded that heat transfer in the tip gap region is a steady phenomenon. One of the observations made in the current work indicates that the tip heat transfer is not strictly steady. It is possible that for subsonic flows through the turbine, the absence of shocks in the tip gap diminishes the effect of unsteadiness in comparison to transonic flows. It is also possible that the mechanism for heat transfer in the tip gap changes from viscous interactions for subsonic flows to a combination of viscous and inviscid effects associated with supersonic flow. In order to understand these effects it is important to study heat transfer and the manner in which it is affected by shocks, boundary layer thickness and free stream conditions. A brief introduction to these concepts follows.

1.2 Heat transfer

Heat transfer is an interaction in which energy is transferred from one system to another. The energy is transferred from the higher temperature system to the lower temperature system through several possible mechanisms. These are convection, conduction and radiation. Convection occurs in fluids through both diffusion and advection. Diffusion is the random motion of particles that results in no net or bulk fluid motion while advection is the physical transport of fluid molecules. In this manner the higher temperature fluid interacts with its surroundings in order to achieve thermal equilibrium. The transfer of energy to and from a system results in a change to the internal energy of the system. This interaction is governed by the first law of thermodynamics or the energy equation in fluid dynamics. The heat transfer rate is often characterized by a non-dimensional quantity know as the Stanton number. It is defined as [5]

$$St = \frac{h}{C_P \cdot \rho \cdot V} \qquad 1.1)$$

$$h = \frac{q_{wall}}{T_{wall} - T_{ref}} \qquad 1.2)$$

$$q_{wall} = -k \cdot \left.\frac{dT}{dn}\right|_{wall} \qquad 1.3)$$

$$\Pr = \frac{\mu_{wall} \cdot C_P}{k} \qquad 1.4)$$

$$\therefore \mu_{wall} = \frac{\Pr \cdot k}{C_P} \qquad 1.5)$$

Substituting 1.3 in 1.2 and then substituting 1.2 and 1.5 into 1.1 leads to

$$St = \frac{-\left.\frac{dT}{dn}\right|_{wall}}{T_{wall} - T_{ref}} \cdot \frac{\mu_{wall}}{\rho \cdot V \cdot \Pr} \qquad 1.6)$$

The variables in equation 1.6 can be non-dimensionalized using appropriate reference variables to give

$$St = \frac{-\left.\frac{d\overline{T}}{d\overline{n}}\right|_{wall}}{\overline{T}_{wall} - \overline{T}_{ref}} \cdot \frac{\overline{\mu}_{wall}}{\overline{\rho} \cdot \overline{V} \cdot \Pr} \cdot \frac{\mu_{ref}}{\rho_{ref} \cdot n_{ref} \cdot V_{ref}} \qquad 1.7)$$

This quantity is a non-dimensional heat flux and is used to quantify the thermal load on viscous surfaces in the high pressure turbine as done in Chapter 5. If the surfaces are maintained at a fixed temperature (isothermal) the heat flux provides an indication of the temperature in the free stream. Areas with large heat flux will require more cooling. Given a free stream temperature, the heat flux is inversely proportional to the thickness of the boundary layer.

1.3 Shock-boundary layer interaction

A boundary layer is the thin region near a solid boundary over which a fluid travels. In a macroscopic sense, it is a result of the surface interaction with an adjacent layer of the fluid that causes the adjacent fluid to 'stick' to the surface or to be brought to rest. The stationary particles on the surface slow down the neighboring fluid particles creating a velocity profile that looks like figure 1.3. This effect is due to viscosity that is a frictional property of the fluid and is represented by the coefficient of viscosity, μ. At low Reynolds numbers, the fluid flows in layers over the bounding surface and this is known as laminar flow.

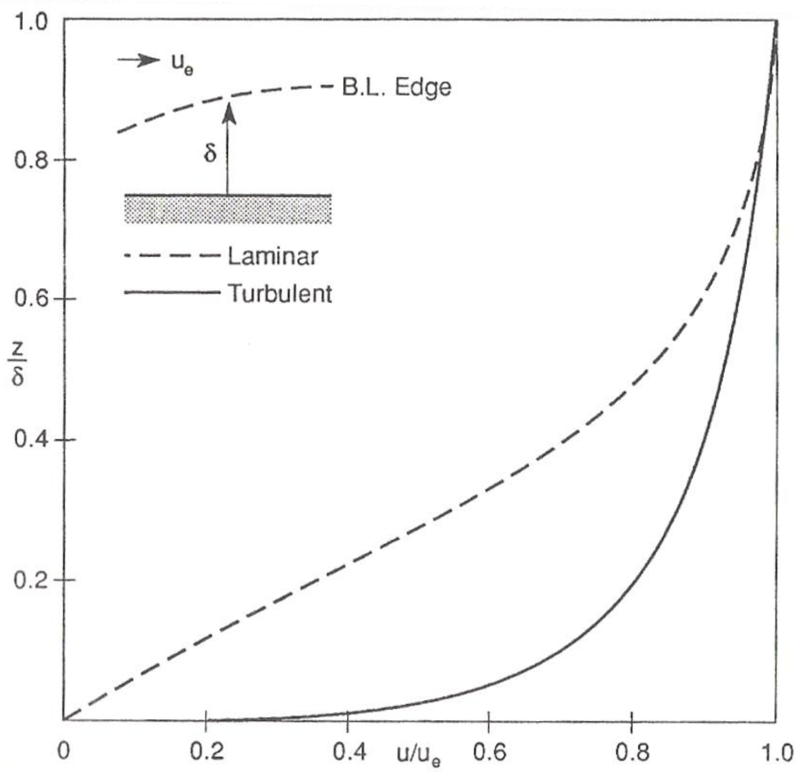

Fig. 1.5 Typical velocity profiles on a flat plate at zero incidence for laminar and turbulent boundary layers.

Figure 1.3 Velocity profiles in boundary layer [5]

However, in the case of turbomachinery flows, the Reynolds number of the fluid is often high enough that the fluid molecules no longer remain confined to layers and mix through diffusion and convection in a direction other than the streamwise direction. This is known as turbulent flow and is characterized by the bulk eddying motion of the fluid molecules in addition to their diffusive random motion. These eddies are of various length scales ranging from the dominant length scale of the flow to much smaller length scales that dissipate their kinetic energy to the bounding surface through viscous interactions. The additional degrees of freedom are accompanied by a thickening of the boundary layer along with higher heat transfer. The surface heating is increased due to the larger velocity gradients in a turbulent boundary layer that lead to higher wall shear stress. This is a viscous effect that also leads to higher skin friction coefficients. Also, the increased diffusivity causes an increase in mass, heat and momentum transfer in the flow as compared to laminar flows. The rate at which kinetic energy, k ,is converted to heat is the rate of dissipation, ε. It is assumed that turbulent flow can be described as the sum of a mean flow and local fluctuations as,

$$u_i(\vec{x},t) = \overline{u}_i(\vec{x}) + u_i'(\vec{x},t) \qquad 1.8)$$

where u_i *(i=1,2,3)* are the components of the fluid velocity and $\vec{x}$ is the vector location of the fluid at which it is being observed. The quantities with an overbar represent the steady or mean flow values while the primed quantities represent fluctuating values. The additional shear stress due to turbulence is given by

$$\tau_{ij} = -\rho \cdot \overline{u_i' u_j'} \qquad 1.9)$$

This brief summary of turbulence is provided to better understand the equations presented in chapter 2 and the discussion in chapter 5. A more detailed analysis of turbulence and turbulence modeling can be found in [6] and [7].

Figure 1.4 [8] shows a picture of shocks interacting with different types of boundary layers. The incoming free stream fluid is supersonic. Any change in flow area (due to changes in viscous surface geometry, due to development of boundary layer or due to formation of shear layers that restrict flow area) can lead to the formation of an oblique shock. The shock causes the boundary layer to thicken due to the effect of compressibility (high density gradient). This in turn can lead to a reduction in heat flux to the surface. Depending on the downstream geometry the shock can reflect as another oblique shock or a series of expansions and compressions could follow. In figure 1.4a the shock causes a region of separation in the laminar boundary layer and reflects as another oblique shock. The intermediate compression and expansion fans are caused by the change in boundary layer geometry and are significantly weaker than the incident shock. Figures 1.4b and 1.4c show a similar phenomenon in turbulent flow. Subsonic flows do not have a similar mechanism that impacts heat transfer. Another important difference between subsonic and supersonic flows is the manner in which the boundary layer develops as a function of Reynolds number. For a supersonic laminar boundary layer, the boundary layer thickness varies as [9],

$$\frac{\delta}{x} \alpha \frac{M_\infty^2}{\sqrt{\mathrm{Re}_x}} \qquad 1.10)$$

For a subsonic laminar boundary layer, the boundary layer width varies as [5],

$$\frac{\delta}{x} \alpha \frac{1}{\sqrt{\mathrm{Re}_x}} \qquad 1.11)$$

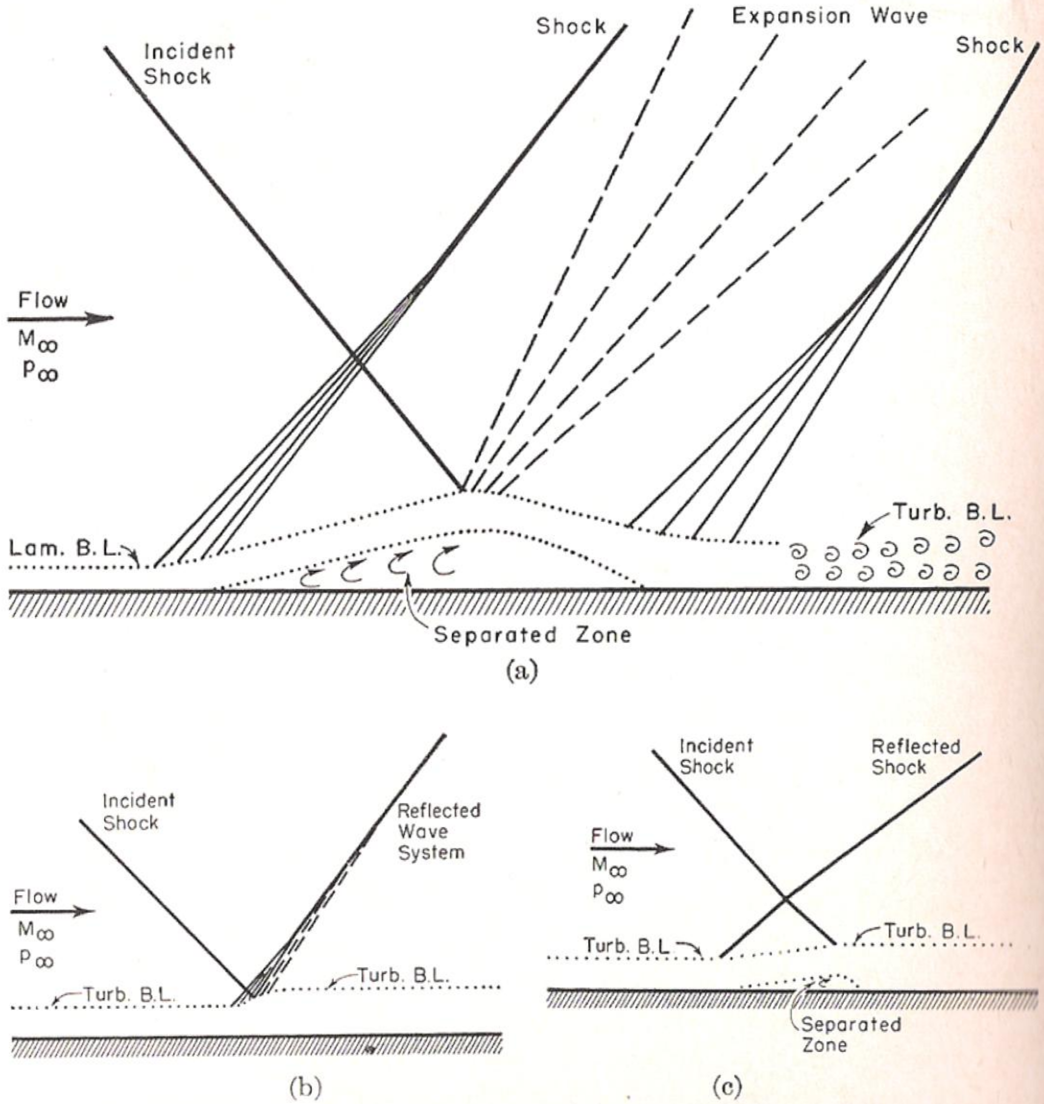

FIG. 28.11. Typical features observed in reflection of shock from walls with boundary layers.

(a) Laminar boundary layer.
(b) Turbulent boundary layer.
(c) Turbulent boundary layer with separated zone.

Figure 1.4 Shock-boundary layer interaction [8]

This means that as the Mach number of a supersonic flow increases, the boundary layer thickness increases. A subsonic boundary layer develops purely as a function of Reynolds number. Therefore, a highly loaded turbine blade will be subjected to inviscid effects that are otherwise not present, for example, at the tip. This discussion will be used to interpret results in chapter 5.

1.4 High pressure turbine stage

Unsteady stator-rotor interaction:

It is well known that flow through the high pressure turbine is highly unsteady. This is primarily due to the interactions of the passing wake and, in the case of transonic stages, shock structures. This unsteadiness is particularly important to film cooling applications at the rotor leading edge. It is therefore important to understand the nature of unsteadiness with regard to both pressure and heat transfer at the leading edge as well as the rotor tip.

Hodson and Dawes [10] studied the effect of unsteadiness on exit profiles emerging from a two dimensional multi-blade row compressor cascade subject to unsteady wakes at the inlet. They detailed the distortion of the wake through chopping, stretching and shearing by the neighboring blade row. The vortex structure between blades downstream of the unsteady wake, they suggest, tends to push the flow from the pressure side to the suction side. This pushes the stagnation point closer to the crown of the blade rather than the leading edge.

Denos et al. [11] also observed this effect and noted that the stator trailing edge shock moves from the crown of the rotor towards the leading edge with the passage of the wake from the upstream stator. For their study, Denos et al. [11] used the implicit time marching code MDFLOS3D that solves the unsteady Favre-averaged Navier-Stokes equations in a quasi-three-dimensional manner. Only the rotor mid-span was analyzed. A similar effect of the vane trailing edge shock was noted by Giles [12].

Shang and Epstein [13] found that a non-uniform inlet profile resulting from hot streaks results in a segregation effect that would push hot gas preferentially towards the pressure side of the blade. They simulated the effect of hot streaks passing through the stage and were therefore able to easily follow the high entropy streaks through the passage. Ameri et al. [14] also noted the effect that segregation might have on blade heat transfer. A velocity triangle is shown in figure 1.5. The velocity triangle at the top of figure 1.5 represents the velocity at the inlet to the rotor for a steady simulation that has a uniform pressure and temperature profile at the inlet. The relative velocity is the result of subtracting the tangential velocity from the absolute velocity. The diagram at the bottom of figure 1.5 shows velocities in the stator wake at the inlet to the rotor for an unsteady simulation. As a reference, an airfoil from a rotor is provided to the right of figure 1.5. All images in the figure are not to scale and angles and velocity magnitudes have been exaggerated for clarity. The segregation effect as described by Kerrebrock and Mikolajczak [15] occurs because the Mach number profile in the circumferential direction stays approximately constant while the rotor wake, having a lower temperature, forces the local absolute velocity to diminish. This produces a relative velocity which is at a shallower angle to the axial. Thus, the cooler wake flow and hotter free stream flow would be distributed at different angles in the rotor frame of reference. The wake fluid would direct the cooler fluid towards the suction side.

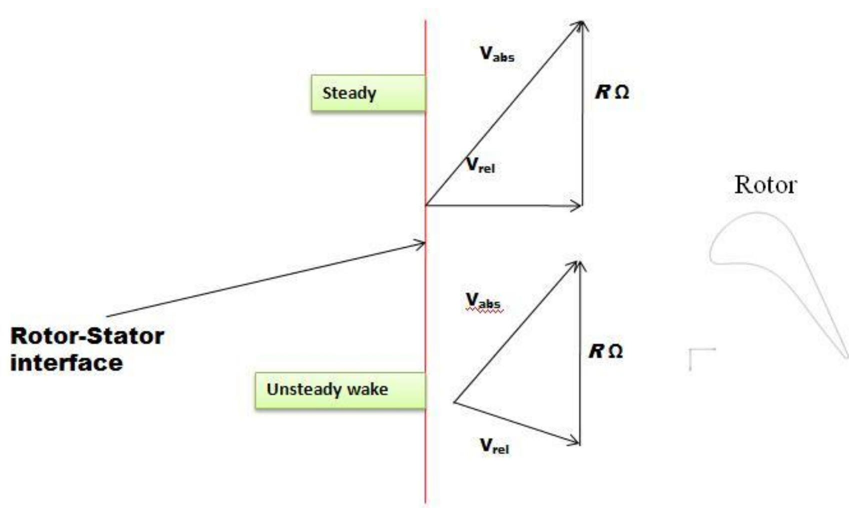

Figure 1.5 Velocity triangles in the stator wake for steady (top) and time-average of unsteady (bottom) simulations

This phenomenon of thermal segregation would be absent in the case of a steady simulation because a steady simulation typically implies a flat or uniform inlet profile in the tangential direction. Even if a steady simulation were performed with a non-uniform inlet profile, the relative frequency between the stator and rotor would lead to a mismatch in the inlet profiles between the steady and unsteady simulation. Therefore, it would be expected that a steady and an unsteady computation lead to different heat transfer patterns on the blade surface. The aforementioned simulations and theories were confined to stages where the flow was completely subsonic.

Bell and He [16] performed an experiment to study the tip leakage on an oscillating blade. They found that the unsteadiness in the tip gap flow field is primarily an inviscid effect by comparing their data to an inviscid simulation. Urbassik et al. [17] conducted experimental investigations on vane-rotor aerodynamic interactions and found that while unsteadiness is caused by a combination of shocks, potential fields and vane wake interactions, the upstream wake has little influence on rotor unsteadiness.

Ameri et al. [14] performed an unsteady, three dimensional simulation on the E^3 (Energy Efficient Engine) turbine blade geometry. They used a sinusoidal inlet profile to simulate an unsteady wake and assumed a 1:1 stator to rotor blade count. They found significant differences between the unsteady and steady heat transfer results in localized regions, particularly in the near tip and near hub regions on the suction side of the blade. Although a general rise in the level of heat transfer was predicted by the unsteady simulations compared to the steady simulations they found no substantial difference in the tip heat transfer. Tip heat transfer is however known to be highly dependent on airfoil geometry.

For the case considered in Chapter 5 that is the main focus of this thesis, Tallman et al. [18] and Luk [19] obtained steady state heat transfer and pressure results from CFD simulations using TACOMA [20] and TURBO [21] [22] [23] respectively. The former used a k-ω turbulence model while the latter used the k-ε model of Zhu and Shih [24] that is also used in this dissertation. The surface pressure and heat transfer results matched well with experiment for both cases. Both authors observed the presence of a shock between the trailing edge of a rotor blade and the suction surface of the adjacent rotor blade.

Van Zante et al. [25] performed simulations on a 2½ stage compressor and found that phase lagged boundary conditions are accurate for single-stage cases and do not account for stator-stator or rotor-rotor interaction for multi-stage cases. The current study involves a stator-rotor interaction within a single stage and is therefore able to employ the phase lag condition to accurately represent unsteadiness. It was also found [25] that owing to the storage of time history for the phase lag model, convergence requires more time than for the periodic model for multi-stage cases. However the advantage of using phase lag is that only one blade passage from each row is required for the simulation. Gerolymos et al. [26] also used phase lag (chorocronicity) to verify the ability of this boundary condition to predict shock interactions between two neighboring blade rows. They also provide a list of studies conducted by various authors on blade-row interaction.

Tip flow and heat transfer

As a result of the pressure distribution set up around the rotor blade, there is a pressure gradient in the tip gap of the rotor. The high pressure gas on the pressure side of the blade has a tendency to flow towards the low pressure suction side across the tip. The path of the tip flow depends on several parameters such as blade rotational rate, blade geometry (tapering, twist, camber, tip gap height and tip contouring) and flow inlet angle. No matter what the cause of the leakage flow, it results in a drop in efficiency.

A detailed literature review of the basic features of turbine tip flow and heat transfer has been conducted by Bunker [27] and Ameri [28]. Ameri [28] describes the primary flow features seen due to tip leakage: the pressure side separation bubble on the tip surface and the tip leakage vortex. The extent of the bubble and its reattachment are contingent on blade thickness, Mach number, Reynolds number and tip height [28] [29]. For subsonic flows, the percentage of inlet flow that constitutes the tip leakage is shown to grow linearly with tip gap height. Studies involving low Mach number flows show a recirculation zone above the tip gap exit due to relative casing motion [27] [28] [30]. In both [27] and [28] the importance of CFD in tip flow and heat transfer prediction is emphasized especially due to the difficulty of conducting experimental measurements in a rotating tip gap.

Ameri et al. [30] simulated the GE-E^3 high pressure turbine stage and studied the tip flow and heat transfer for a smooth tip and for a recessed tip. The cavity height of the recess was varied in the study to analyze the effect of recess depth on tip heat transfer. Two primary vortex structures were observed in the recess. It was found that the recess had negligible effect on loss and did not improve the heat transfer distribution on the tip as a whole.

Another study by Ameri et al. [31] investigated the effect of upstream casing recess on tip leakage and heat transfer and found that minimal tip heat transfer occurred for a recess height that is almost equal to tip clearance. They conclude that the recess has little effect on efficiency. This can be explained by approximating the effective tip gap geometry by a diverging-converging nozzle. Unless the tip gap height is extremely small, the flow will first be expanded and then recompressed before exiting to the suction side.

O'Dowd et al. [32] used several techniques to measure the heat transfer coefficient and adiabatic wall temperature on a transonic turbine blade tip (Rolls Royce Environmentally Friendly Engine.) Almost all their measurement techniques showed high heat flux and adiabatic wall temperature in the leading edge region of the tip and a thin band of low heat flux on the aft pressure side edge of the tip. The complexity of measuring accurately the heat flux in the tip gap is elaborated on and it is for this reason that CFD is of great benefit.

Hofer et al. [33] conducted an experimental study of leakage flow for a non-rotating linear turbine cascade. The study looked at the impact of cooling in the tip gap for two squealer geometries. They considered a full squealer tip and a suction side squealer tip and concluded that the suction side squealer resulted in higher heat transfer and loss coefficient. This is to be expected because at subsonic conditions, the suction side squealer tip effectively acts as a converging nozzle that accelerates flow through the tip. Hofer et al. [33] claim that neglecting the relative casing motion does not significantly alter the results because of previous studies like that of Krishnababu et al. [34]. The latter studied the effect of relative casing motion on tip heat transfer and tip leakage mass flow for two different tip gap heights. They concluded that the effect of relative casing motion is diminished for larger tip gap heights due to dominant inviscid effects.

More recently, Wheeler et al. [35] conducted a steady CFD simulation of tip flow for a transonic turbine rotor using Spalart-Allmaras and standard k-ε turbulence (with wall functions) models. They claim that at high speeds, the turbulence model has little effect on heat transfer prediction. However, due to the lack of grid refinement near the wall and the use of wall functions it is not clear that this is in fact the case. Using a quasi-3D approach, they observe a quicker reattachment of the separation bubble at higher Mach number. They also state that there is a drop in heat transfer coefficient due to decreased turbulent mixing at high Mach numbers and that the flow is dominated by local pressure gradients. As it is pointed out by Wheeler et al. [35], high speed flow through the tip gap chokes the flow and therefore provides an opportunity to raise the mass flow through the passage without added aerodynamic penalties.

Previous computational studies of high pressure turbines have dealt with two dimensional cascades [10], [36] or have assumed a periodic inlet boundary [13] to the rotor to simulate unsteadiness. In general, unsteadiness has been computed by compromising either the dimensionality of the flow or frequency of unsteadiness. This work is believed to be the first unsteady three dimensional CFD simulation of heat transfer on a highly loaded transonic turbine stage. Special attention is given to inviscid flow effects that have not been well documented for turbine blades. The code utilized is TURBO [23] and a brief description of TURBO is provided below. Unsteadiness is simulated using a phase lagged boundary condition in the pitch-wise direction. The implementation and theory behind this boundary condition can be found in several publications such as [21], [22] and [23]. In the following section a brief description of the CFD code TURBO is provided to aid in the understanding of subsequent code related discussion.

1.5 TURBO

TURBO is an unsteady, viscous, three dimensional RANS code. Appendix A lists the governing equations that are solved in the code and a more detailed listing of equations and methods used in the flow solver is available in [21], [22], [23], [25] and [37]. The governing equations of fluid motion are written in vector form and nondimensionalized using appropriate reference values such as speed of sound, diameter of blade tip, inlet temperature and inlet pressure. The physical domain is then transformed into a computational domain to simplify manipulations on boundary surfaces. A modified high order, upwind Roe scheme [38] is employed for spatial discretization with Newton sub-iterations to converge the solution at every time step. Due to the upwinding scheme used in this simulation there is no addition of artificial dissipation. The code is fully parallelized to use MPI (Message Passing Interface) [23], [37]. The code was designed to simulate axial flows and as such is designed to work with grids conforming to certain specifications. The specifications are listed below. Refer to figure 1.6 for the following discussion. In the following list, i, j and k are the indices of the computational coordinates.

- The inlet face must be at i_{min}
- The exit face must be at i_{max}
- The inlet and exit should be in the axial (x) direction.
- Periodic surfaces should be constant k surfaces
- The j index represents the radial direction with j_{min} being the hub surface and j_{max} the casing. In a rotating simulation only the j_{max} surface can be stationary.

Here, i_{min} refers to the minimum value of the computational coordinate, i, within a block and i_{max} refers to its maximum value. The same principle applies to the other two computational coordinates.

These specifications are major limitations when dealing with complicated flows such as flow over a blade with film cooling holes and plenums. The plenum inlets are rarely axial. Grids generated through various software do not always produce computational coordinate orientations that are consistent with the parameters listed above. TURBO would have to deal with grids of arbitrary orientation in both the physical and computational coordinates.

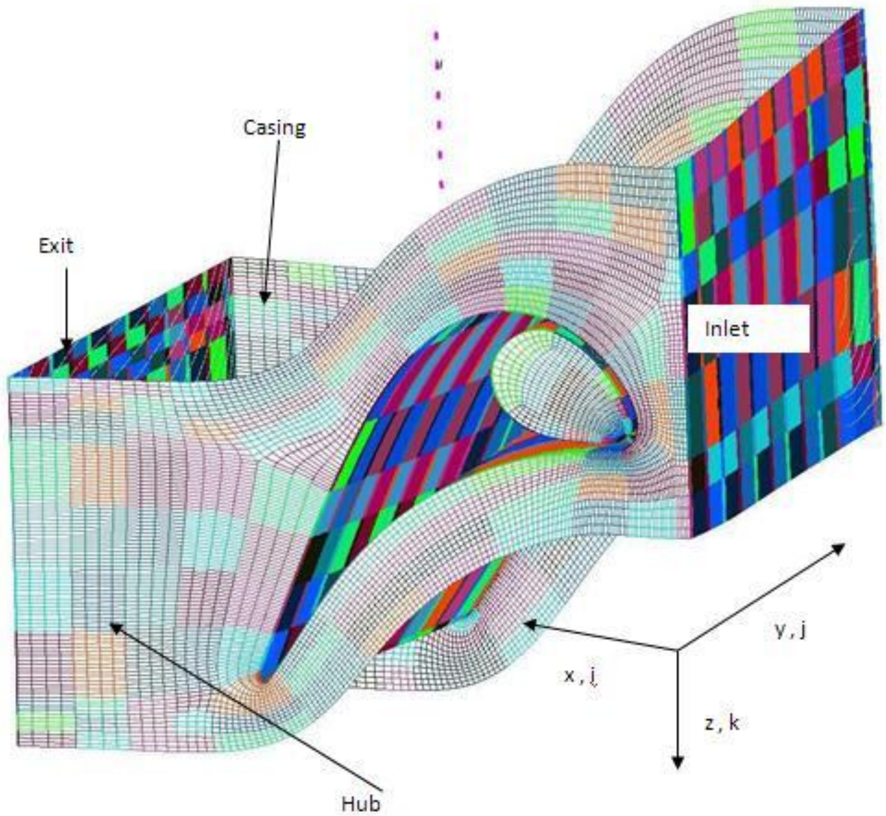

Figure 1.6 Example of a computational domain for a rotor blade

1.6 Thesis outline

The primary objective of this work is to increase the understanding of unsteady flow and heat transfer in a high pressure turbine stage. This work is intended to facilitate the use of structured grids generated by an unstructured-multiblock grid generation software and to extend TURBO's ability to predict heat transfer.

- Chapter 2 presents the implementation of Wilcox's k- ω turbulence model ([39] [6]) into TURBO and the addition of an isothermal wall boundary condition. Validation of the model and the new boundary condition for the case of flow over a flat plate are documented. In addition, chapter 2 describes several modifications to existing boundary conditions and the addition of a plenum inlet boundary condition for film cooling application.
- Chapter 3 provides a brief overview of the creation of a preprocessor to facilitate the use of H-O-H type grids generated by an unstructured multiblock grid generator called GridPro™. Details regarding the creation of the preprocessor are presented in appendix B.
- Chapter 4 describes work to further test the heat transfer capabilities of TURBO by simulating flow over a flat plate with a cooling hole. This simulation also served to compare the preexisting k-ε turbulence model [24] of TURBO to the newly implemented k-ω model [39] discussed in chapter 2.
- Chapter 5 presents an analysis of unsteady flow and heat transfer in a high pressure turbine stage.
- Conclusions and suggestions for future work are presented in Chapter 6.

Chapter 2: Validation of Isothermal Boundary Condition and k-ω Turbulence Model

2.2 Wilcox's k-ω turbulence model

Wilcox's k-ω turbulence model ([39] and [6]) was incorporated into TURBO by adding the appropriate source terms into the general 2–equation turbulence model equation that is already implemented in TURBO. The general two-equation model is given by [39],

$$
\begin{aligned}
&(\rho s_i)_{,t} + (\rho s_i u_j + q_{ij})_{,j} = H_i \\
&q_{ij} = -(\mu + \mu_T / \mathrm{Pr}_i) s_{i,j}, \; i = 1,2.
\end{aligned}
\qquad 2.1)
$$

Here, $s_1 = k$, $s_2 = \omega$ and $\mu_T = \alpha^* \rho k / \omega$. The source terms *H* are given by,

$$
\begin{aligned}
&H_k = \mu_T \Omega^2 - \frac{2}{3}\tau\rho k - \beta^* \rho k \omega \\
&H_\omega = \alpha\left(\mu_T \Omega^2 / k - \frac{2}{3}\tau\rho\right)\omega - \beta\rho\omega^2
\end{aligned}
\qquad 2.2)
$$

where Ω is the vorticity. The coefficients in the model are defined as follows,

$$\mathrm{Pr}_k = \mathrm{Pr}_\omega = 2.0, \quad \beta = 3/40, \quad \beta^* = 0.09F_\beta, \quad \alpha = (5/9)\left(F_\alpha / F_\mu\right)$$

$$F_\beta = \frac{5/18 + (\mathrm{Re}_T / R_\beta)^4}{1 + (\mathrm{Re}_T / R_\beta)^4}, \quad F_\alpha = \frac{\alpha_0 + \mathrm{Re}_T / R_\omega}{1 + \mathrm{Re}_T / R_\omega}, \quad F_\mu = \alpha_0 = \frac{\alpha_0^* + \mathrm{Re}_T / R_k}{1 + \mathrm{Re}_T / R_k}$$

$$\mathrm{Re}_T = \frac{\rho k}{\mu \omega}, \quad \alpha_0 = 0.1, \quad \alpha_0^* = 0.025, \quad R_\beta = 8, \quad R_\omega = 2.7, \quad R_k = 6.$$

The boundary conditions for a no slip surface are [39], $k = 0, \quad \omega = 100 \left.\frac{\partial u}{\partial y}\right|_{wall}$. An upper limit [39] of $(\omega_{\max})_{wall} = \frac{800}{\mathrm{Re}} \frac{\nu}{(\Delta y)^2}$ was imposed at the wall to avoid large eddy viscosities in leading edge regions.

2.3 Boundary Conditions

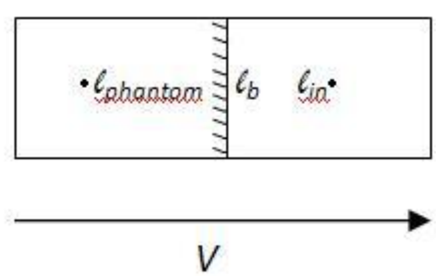

Figure 2.1 A computational boundary

Several modifications were made to TURBO to allow it to handle not only inlets and exits in different physical orientations (*x,y,z*) but also arbitrary computational (ξ,η,ζ) directions. Code was developed to study inlet and exit blocks and to determine whether or not the blocks are part of a flow passage with an identifiable hub and shroud. In the event of a hub and shroud being identified, the hub to shroud direction is specified as the direction for setting up radial profiles. If no hub to shroud direction is located, the code assigns uniform conditions at the inlet or exit. A plenum inlet boundary condition was added using general characteristic boundary conditions [40]. Figure 2.1 shows the stencil used for the plenum boundary condition. The symbol, ℓ, refers to an arbitrary computational index (i, j or k). It is assumed that the flow will enter the plenum inlet normal to the plenum inlet surface. The unit normal to the surface is given by [41]

$$\vec{n} = \frac{1}{\sqrt{\xi_x^2 + \xi_y^2 + \xi_z^2}} \left(\xi_x \hat{i} + \xi_y \hat{j} + \xi_z \hat{k} \right) \qquad 2.3)$$

Therefore the velocity component normal to the surface, just inside the computational domain is given by $u_{in} = \vec{V} \cdot \vec{n}$, where $\vec{V} = v_x \hat{i} + v_y \hat{j} + v_z \hat{k}$ is the velocity at ℓ_{in}. The non dimensional speed of sound, c_{in}, is calculated as $\left. \sqrt{\frac{\gamma p}{\rho}} \right|_{in}$.

The Riemann invariants at ℓ_{in} and ℓ_b are related as

$$R_{in} = u_{in} - \frac{2c_{in}}{\gamma - 1} = R_b = u_b - \frac{2c_b}{\gamma - 1}$$

$$\therefore u_b = R_b + \frac{2c_b}{\gamma - 1} \qquad 2.4)$$

The speed of sound at ℓ_b is calculated as follows:

$$\frac{T_0}{T_b} = 1 + \frac{\gamma - 1}{2} M_b^2$$

$$T_b = c_b^2; \quad M_b = \frac{u_b}{c_b}$$

$$\therefore c_b^2 = T_0 - \frac{\gamma - 1}{2} u_b^2 \qquad 2.5)$$

Now, substituting 1) in 2) leads to

$$c_b^2 = T_0 - \frac{\gamma - 1}{2} \left(R_b + \frac{2c_b}{\gamma - 1} \right)^2 \qquad 2.6)$$

This is a quadratic equation in c_b that is easily solved [41] and substituting back into 1) gives u_b. The individual velocity components, density and pressure at the phantom cell are then computed as

$$\vec{V}_b = \frac{u_b}{\sqrt{\xi_x^2 + \xi_y^2 + \xi_z^2}} \left(\xi_x \hat{i} + \xi_y \hat{j} + \xi_z \hat{k} \right)$$

$$\rho_b = \frac{\gamma P_0}{T_0} \qquad 2.7)$$

$$P_b = \frac{P_0}{\left(1 + \frac{\gamma - 1}{2} M_b^2 \right)^{1/\gamma - 1}}$$

It is also possible to specify multiple inlet pressures and temperatures through the input files (for cases having more than one inlet and/or exit). This will allow users to specify a plenum temperature and pressure that are different from the inlet pressure and temperature of the blade row. For film cooling applications where the plenum pressure is close to the main flow pressure and the density ratio is high, it is possible for backflow to occur during convergence. This can lead to failure of the simulation. To avoid this scenario, the speed of sound, c_b, in equation 2.6 was modified to $c_b = |c_b|$ and u_b in equation 2.7 was replaced by $|u_b|$ to force flow to enter the plenum normal to the plenum inlet face and therefore aid in convergence. Inlet and exit mass flux calculations were updated to accurately display mass flux regardless of the inlet and exit direction. Slip and no slip boundary conditions were also updated to enable them to handle directional generality. In addition, minor modifications in the treatment of viscous fluxes and in the calculation of pressure and energy in phantom cells were implemented.

To enable the study of heat transfer, an isothermal boundary condition has been implemented. The temperature at the phantom cell is calculated by assuming that the wall temperature is the average of the phantom cell temperature and the inside cell temperature. The wall temperature is specified as user input.

$$P_{in} = e - \frac{\gamma - 1}{2}\left(\left|\vec{V}\right|^2\right)$$

$$T_{in} = \frac{\gamma P_{in}}{\rho_{in}}$$

$$T_{phantom} = 2T_{in} - T_{wall}$$

$$\rho_{phantom} = \frac{\gamma P_{phantom}}{T_{phantom}}$$

2.4 Flat plate simulation

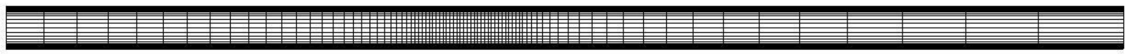

Figure 2.2 Mesh for 2D flow over flat plate

A two dimensional channel grid [41], shown in figure 2.2, was used to model flow over a flat plate by imposing a no slip boundary condition on only one of the two channel walls while maintaining a slip boundary on the other wall. The grid was divided into four blocks, as shown in figure 2.3, with each block containing 41 points in the *i*-direction (local *x* coordinate), 31 points in the *k*-direction (local negative *y* coordinate) and 2 points in the *j*-direction (local negative *z* coordinate).

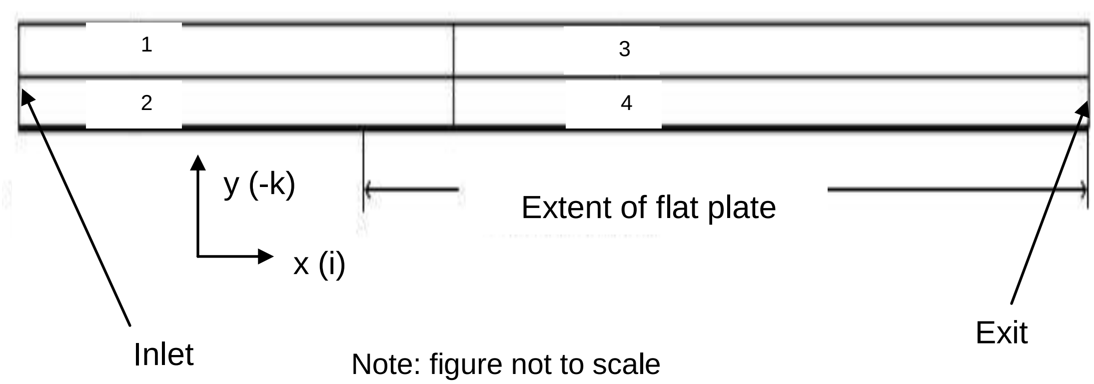

Figure 2.3 Block structure and extent of flat plate

Here, the positive *x* direction is taken to be the downstream direction. The leading edge of the flat plate is contained between (*i*=31, *k*=31, *j*=1) and (*i*=31, *k*=31, *j*=2) in block 2 and the trailing edge is contained between (*i*=41, *k*=31, *j*=1) and (*i*=41, *k*=31, *j*=2) in block 4. The flat plate is 1.46*m* long and the channel height is approximately 0.021*m*. The grid spacing ensures a *y*+ of approximately 1 at the first grid point away from the surface of the flat plate. No-slip boundary condition was imposed on the flat plate. Radial equilibrium was imposed on the exit plane while a characteristic variable inlet boundary was established on the inlet plane. The flow was initialized uniformly with a Mach number of 0.3 and a back pressure of 98000*Pa* with total pressure taken to be atmospheric. For the turbulence model, *k* and *ω* were specified at the inlet based on the inlet turbulence intensity, *Tu*, the inlet velocity, u_i and the turbulent length scale, l. The turbulent intensity at the inlet was specified to be 5%. The code was run at a Courant-Friedrichs-Levy (CFL) number of 5.0. The solutions obtained by running TURBO were deemed to be fully converged when successive iterations varied by less than 0.1% in velocity gradient and temperature gradient. For the case of an adiabatic flat plate, skin friction coefficients were computed based on wall shear stress and free stream dynamic pressure. For the case of an isothermal flat plate local Nusselt numbers were computed as [5],

$$Nu_x = \frac{hx}{k} = \frac{q_{wall}}{T_w - T_\infty} \cdot \frac{x}{k_{wall}}$$

For laminar flow, velocity profiles were compared to those of Blasius' [9] solution for both an isothermal and an adiabatic flat plate.

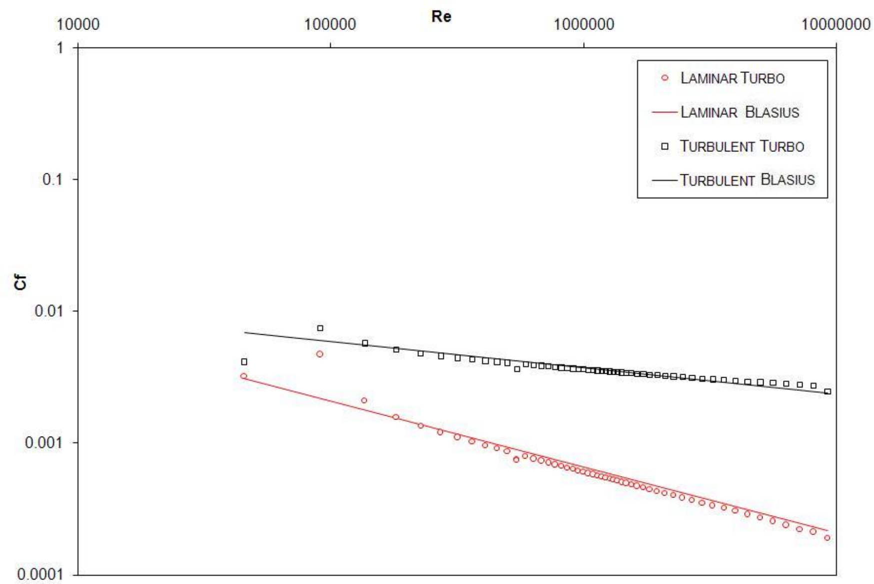

Figure 2.4 Logarithmic plot of local skin friction coefficient versus Reynolds number for an adiabatic flat plate.

Figure 2.4 shows that TURBO predicts fairly well, for Reynolds numbers between 10^5 and 10^7, the skin friction coefficient in both turbulent and laminar flow over a flat plate with no heat transfer at the surface. Small deviations can be attributed to compressibility effects that are neglected in the theoretical solution of Blasius. These compressibility effects become more obvious when the plate is held at a constant wall temperature, T_w, of 0.7 relative to the free stream (see figure 2.5). This is due to the strong dependence of kinematic viscosity on temperature. Further evidence of this can be seen in figure 2.6, where the wall temperature is held at 0.9 relative to the free stream. Agreement with theory is clearly much improved for both laminar and turbulent flow.

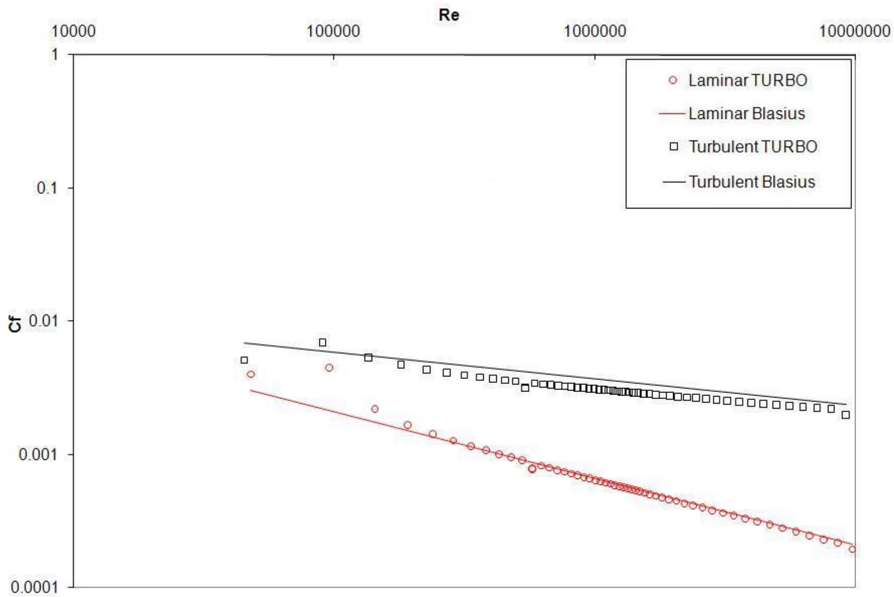

Figure 2.5 Logarithmic plot of local skin friction coefficient versus Reynolds number for Tw=0.7

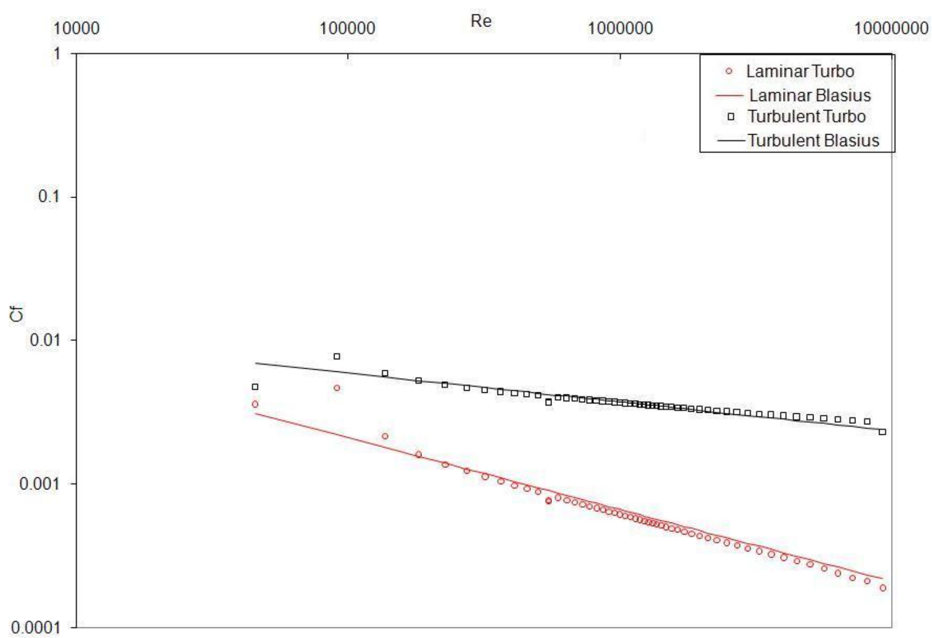

Figure 2.6 Logarithmic plot of local Nusselt number versus Reynolds number for Tw=0.7

Nusselt numbers for the case of T_w=0.9 matched well with theory, for $5 \cdot 10^5 < Re < 10^7$, showing the excellent heat transfer prediction of the k-ω turbulence model at least for the simple case of a flat plate. At a wall temperature of T_w=0.7, compressibility effects cause deviation of TURBO results from theory. Figures 2.7 and 2.8 show skin friction coefficient and Nusselt number respectively for T_w=0.9. Figures 2.9 and 2.10 show a velocity profile comparison with theory for laminar flow over an isothermal flat plate and over an adiabatic flat plate respectively. Here, $\eta = 0.5y(U_e / \nu x)^{0.5}$, is the Blasius similarity variable [5]. The anomalous spike circled in figure 2.7 and seen in the remaining figures occurs at a block interface and is a result of calculating derivatives across block interfaces (such as velocity gradient) using the post processor FIELDVIEW™.

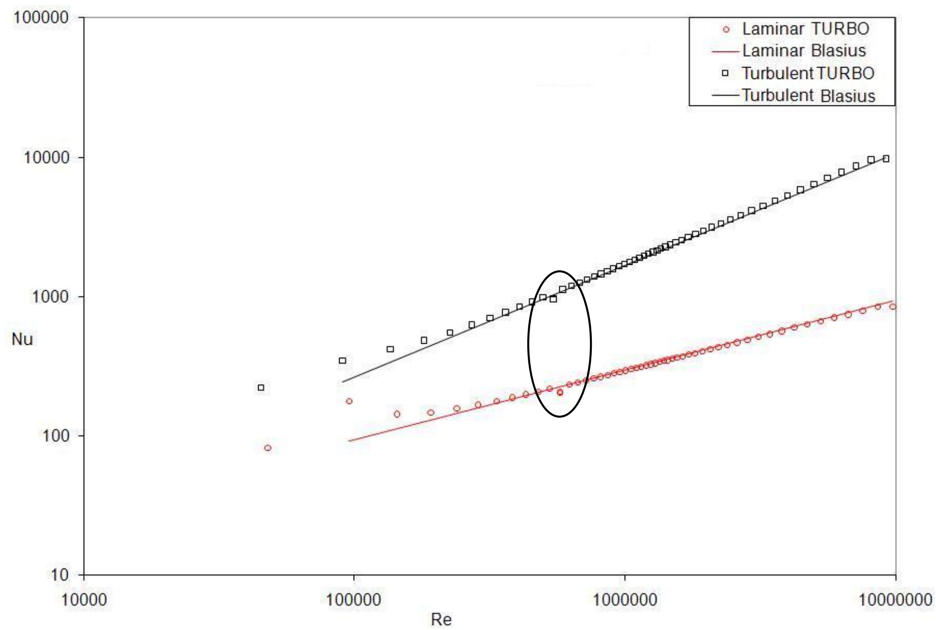

Figure 2.7 Logarithmic plot of local skin friction coefficient versus Reynolds number for Tw=0.9

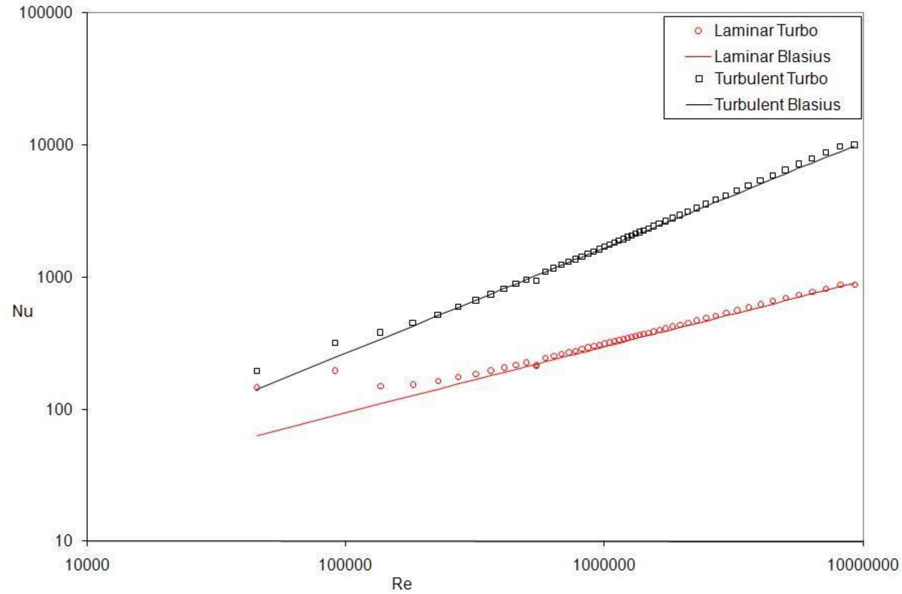

Figure 2.8 Logarithmic plot of local Nusselt number versus Reynolds number for Tw =0.9

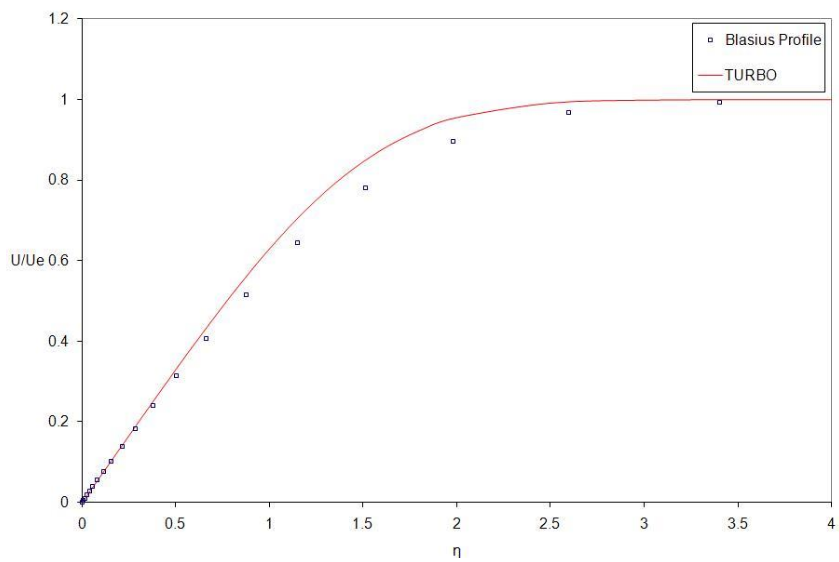

Figure 2.9 Velocity profile for laminar flow over an isothermal flat plate with Tw =0.7

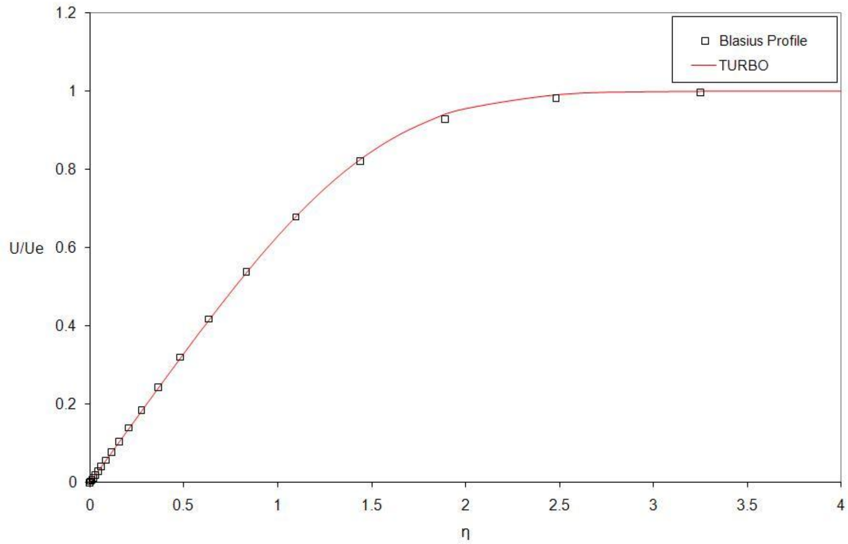

Figure 2.10 Velocity profile for laminar flow over an adiabatic flat plate

2.5 Conclusions

Wilcox's k-ω turbulence model [39] was successfully incorporated into TURBO and validated for the case of a flat plate. In addition, several modifications were made to the available boundary conditions in TURBO to facilitate future simulations of complex turbomachinery geometry such as film cooling. An isothermal wall boundary condition was also added and successfully validated for the case of a flat plate.

Chapter 3: Preprocessor

3.2 Introduction

The CFD code TURBO has traditionally been used to simulate flows in axial compressors. The computational domains are traditionally discretized using a grid generator that produces H-grids. The present work focuses on the high pressure stage of a turbine. The rotors of such stages usually have large turning angles [2]. For such geometries, better grid quality is achieved by generating H-O-H type grids instead of H-grids [41]. In order to generate O-H grids it was decided to utilize the grid generation software GridPro™. This would provide more control over the grid quality. In order to facilitate the use of grids generated by GridPro™ for use in TURBO, a preprocessor was created using the programming language FORTRAN.

The grid generation software GridPro™ generates unstructured multiblock grids (the grid within each block is structured but the block layout is unstructured) [42]. The computational coordinates (*i, j, k*) of the blocks are not ordered according to the specifications presented in section 1.5 and this introduces the need for a preprocessor. Moreover, the boundary conditions and connectivity files generated by GridPro^{TM} need to be converted to formats that are amenable to TURBO.

Starting with a GridPro^{TM} grid and connectivity file, the preprocessor accepts user inputs that detail boundary conditions and blade row information to produce input files [43] that can be utilized to run TURBO. Details of this procedure are given in appendix B. Although there are instances in which manual intervention is required (for example, when opposing faces in a block do not follow the same physical coordinate direction), the procedure is, to a great extent, automated.

3.3 Conclusions

The preprocessor was successfully tested for the geometry involved in the case of flow over a flat plate with a film cooling hole. The results of this simulation are presented in the following chapter while the use of the preprocessor to set up the case is shown in appendix B, section B.4. The same section also describes the use of the preprocessor to set up the geometry simulated in chapter 5.

Chapter 4: Comparison of Turbulence Models for Flow Over a Flat Plate With a Film Cooling Hole

4.2 Introduction

Several computations and experiments have been performed related to film cooling. This chapter briefly summarizes a simulation of flow over a flat plate with one cooling hole at an angle of 35° fed by a plenum. The geometry is shown in figure 4.1 and is the same geometry used in the experiments of Sinha et al. [44].

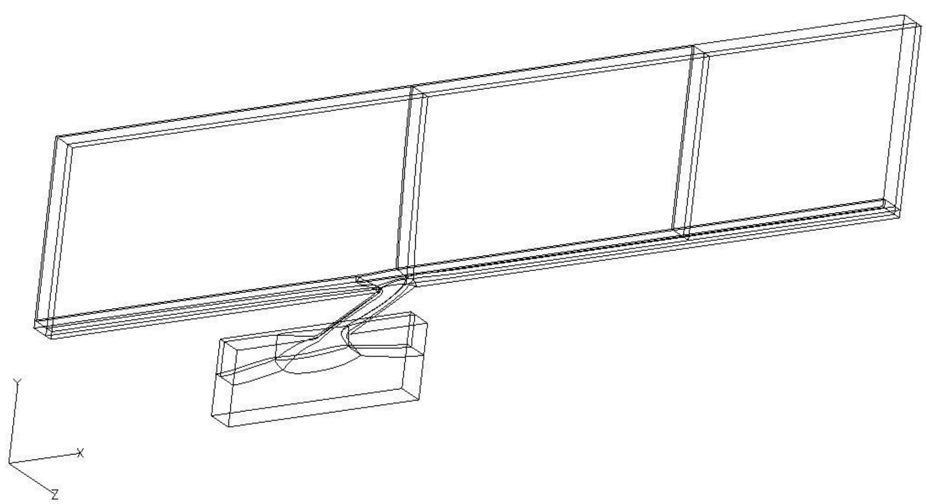

Figure 4.1 Computational domain

This geometry was chosen to further validate the heat transfer capability of TURBO, to compare the two turbulence models now available in TURBO and to test the newly developed preprocessor. Section C.4 in appendix C shows the process of setting up this case using the preprocessor.

It is not the intention of this work to analyze film cooling in any great detail. A more detailed literature survey can be found in [45]. Some salient observations from literature related to film cooling are cited here. Figure 4.2 shows the primary flow features of a jet in crossflow [46].

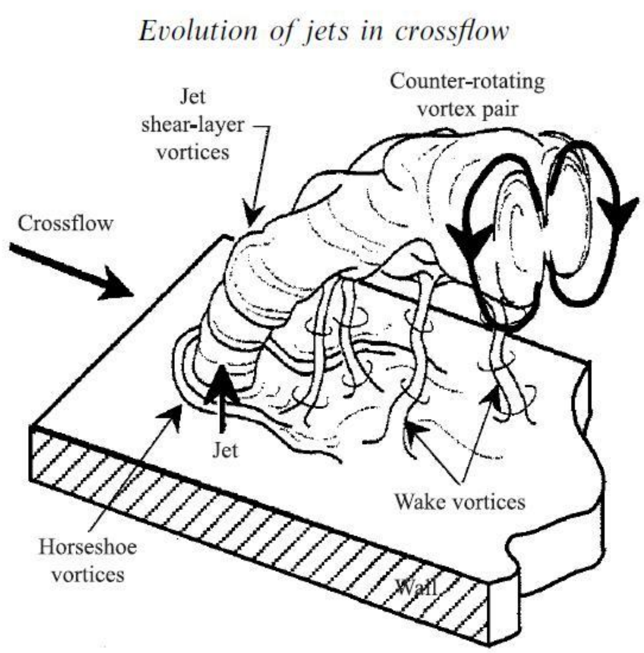

FIGURE 1. Structural features of jets in crossflow (adapted from Johnston & Khan 1997).

Figure 4.2 Features of a jet in crossflow [46]

The counter rotating vortex pair shown in the figure is also referred to as a pair of kidney shaped vortices. They are responsible for drawing the hot free stream gas into the cooler film cooling layer, thereby causing a drop in the effectiveness of the film cooling jet. Adiabatic film effectiveness, η, is defined as a non dimensional temperature ratio that compares the difference between the adiabatic wall temperature, T_{aw}, and the free stream temperature, T_∞, to the difference between the coolant temperature at the hole exit, T_c, and the free stream temperature.

$$\eta = \frac{T_\infty - T_{aw}}{T_\infty - T_c}$$

Ideally the adiabatic wall temperature should equal the coolant temperature producing an effectiveness of 1.0. However, due to the mixing induced by the vorticity downstream of the hole the effectiveness is seldom close to this ideal. The key parameters that characterize film cooling are blowing ratio, *M*, and density ratio, *DR*. The blowing ratio is the ratio of free stream mass flux to coolant mass flux, measured at the hole exit. Density ratio is the ratio of free stream to coolant density, measured at hole exit. The ratio of blowing ratio to density ratio is the velocity ratio. For low rates of coolant injection, the effectiveness rises with blowing ratio. This is because the coolant jet is able to penetrate further downstream and form a wider film. However, at a certain value of blowing ratio, the momentum of the coolant jet is too great to allow it to remain attached to the surface and it 'lifts off' [45]. This causes a reduction in effectiveness immediately downstream of the cooling hole. As the density ratio is increased (by extension the coolant temperature is reduced relative to the free stream), the effectiveness rises for a constant blowing ratio. Bons et al. [47] found that higher turbulence intensity increases effectiveness at high blowing ratios due to enhanced mixing that diminishes the effect of lift-off. They also found that at low blowing ratios, high turbulence intensity attenuates effectiveness.

Lemmon et al. [48] studied the formation of counter rotating vortices for the case of a 35° hole. They found that the vortices are the result of the interaction between the jet and the mainstream and not the boundary layer vorticity of the cooling hole. Sinha et al. [44] performed an experiment to quantify the film cooling effectiveness for the geometry shown in figure 4.1. They performed the experiment for blowing ratios ranging from 0.25 to 1.0 and density ratios of 1.2, 1.6 and 2.0. They found that centerline effectiveness scales with momentum ratio while laterally averaged effectiveness is dependent on density ratio and momentum ratio. The results of the film cooling simulation in this report are compared to the work of Sinha et al. [44] for the highest density ratio case (DR=2.0). It is hoped that this simulation will allow an evaluation of the heat transfer capability of the two turbulence models available in TURBO. For cases of low blowing ratio and high density ratio, turbulent CFD simulations should be able to predict the laterally averaged adiabatic film effectiveness downstream of the hole. In turbomachinery flows, this would indicate that the turbulence model is suitable for predicting heat flux in zones of separation and regions that feature high turbulent production such as the tip gap of a rotor. In addition, this simulation serves as a validation for the ability of TURBO to be used for film cooling simulations.

4.3 Simulation and results

In order to test the modifications made to TURBO, a simulation was run using a fine grid representing a flat plate with a cooling hole and plenum. Figure 4.3 shows the computational grid and boundary conditions. The boundaries not explicitly labeled in figure 4.3 were assigned slip boundary conditions. The cooling hole is inclined at 35° to the freestream as shown in figure 13. The domain was partitioned into 19 blocks and each block was run on a single processor. The flow was initialized as laminar with a Mach number of 0.0 and back pressure of approximately 97% of the inlet stagnation pressure. A converged solution obtained from this laminar flow simulation was then utilized as initialization for a turbulent flow simulation.

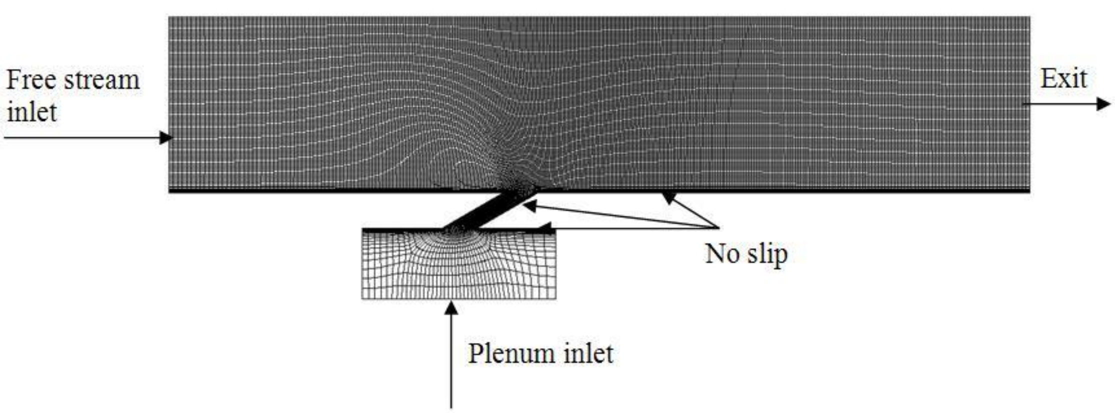

Figure 4.3 Mesh for 35° cooling hole

Table 1 shows the cases for which results are shown in this paper and the plenum inlet conditions corresponding to them.

Table 4.1 Test cases and plenum inlet conditions (normalized with inlet stagnation conditions)

Case	Plenum inlet Stagnation Pressure	Plenum Inlet Stagnation Temperature	Density ratio	Blowing Ratio
1	0.966	0.516	2.0	0.5
2	0.986	0.516	2.0	0.8

The two cases were run using both Wilcox's k-ω turbulence model [39] that has previously been described in this report and the low Reynolds number k-ε model [24]. Figure 4.4 shows span averaged film cooling effectiveness for cases 1 and 2. The data represented in this figures is that of Sinha et al [44]. Here, x=0.0 corresponds to the leading edge of the hole and x=1.0 is the trailing edge of the hole. Case 1 is represented by the color blue while case 2 is represented by the color red. The dashed lines are results of the k-ε simulation and the solid lines are the results of the k-ω simulation. The markers represent data.

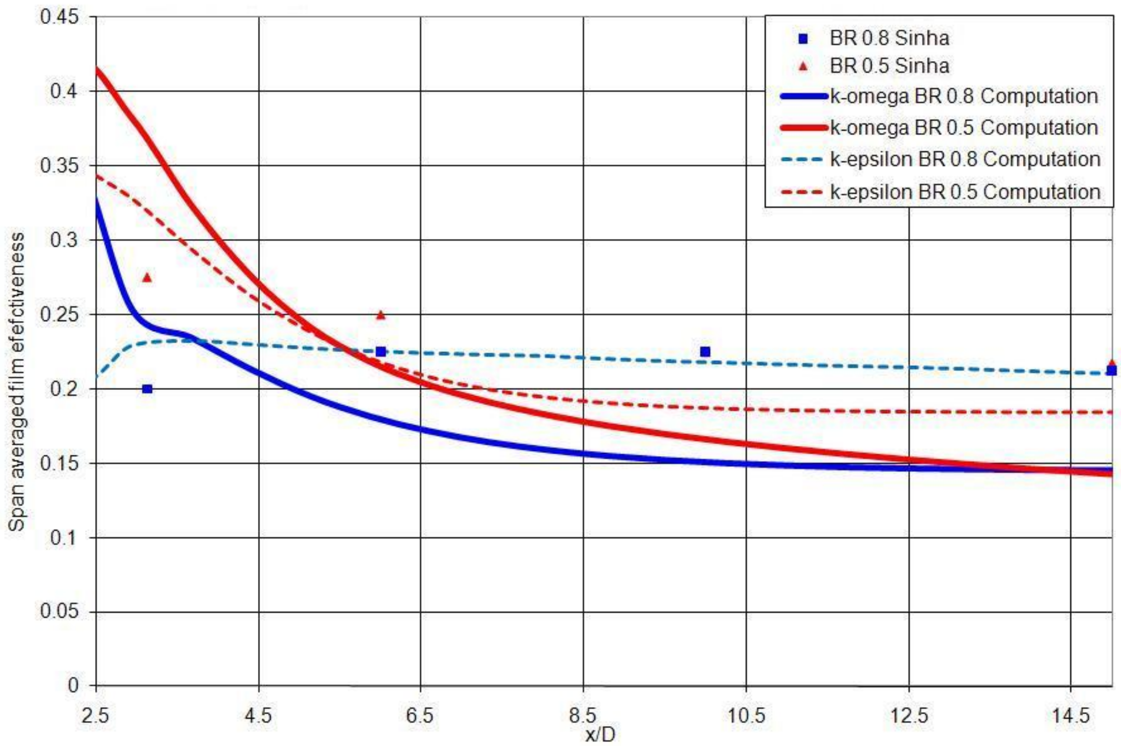

Figure 4.4 Span averaged effectiveness

The results obtained show qualitative agreement with experiments [44] and quantitative agreement with the film cooling work of other researchers such as El-Gabry et al [49]. The quantitative agreement between the k-ε model and data is superior to that of the k-ω model. Qualitatively, the k-ε model better predicts the trend of the data between x/D = 2.5 and x/D = 6.5. Similar behavior for the k-ω model is observed in the literature, for example, El-Gabry et al. [49]. The under prediction of the k-ω model is attributed to an excessive production of turbulence in regions of high rate of strain that leads to enhanced mixing in the wake of the coolant jet [39]. The effectiveness for case 1 predicted by the k-ε turbulence model could be lower than measured by experiment because the actual density ratio achieved by the simulation was 1.88. The curve for effectiveness would certainly shift up if the density ratio were increased. Figure 4.5 shows a cross section of the flow at x/d=3.0 for case 1 with the k-ε turbulence model to show the kidney shaped vortex. Figure 4.6 shows contours of non dimensional temperature for case 1 along the centerline for the k-ε simulation. The contour plot at the bottom of figure 4.6 is a rescaled plot from the work of Thole et al. [50]. The plot was rescaled to provide a better visual comparison with the results from case 1.

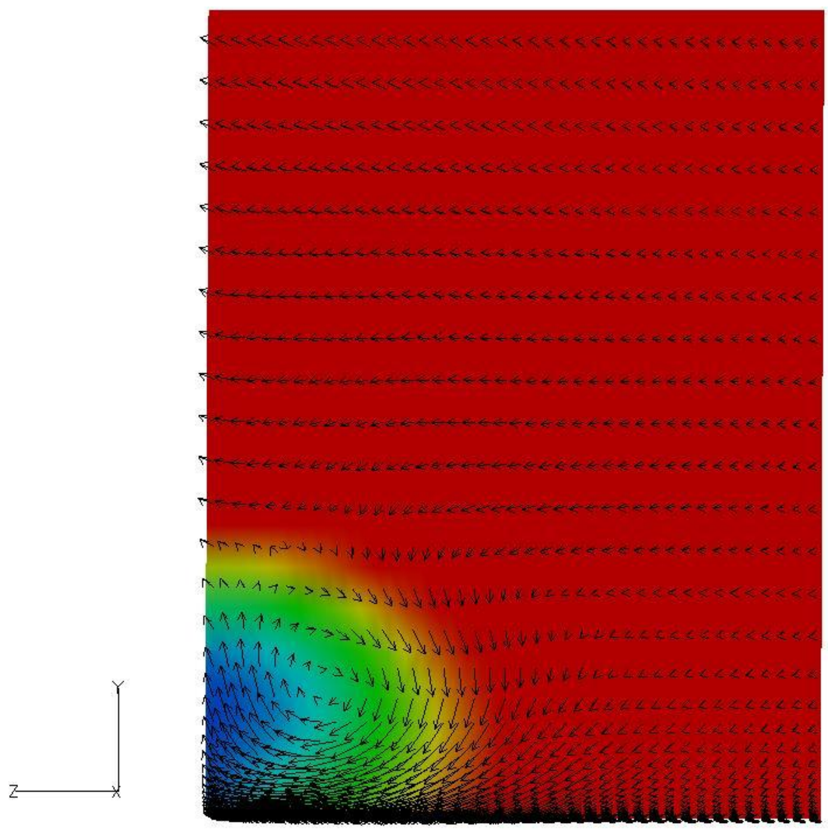

Figure 4.5 Kidney shaped vortex at *x/D*=5.5 (case 1)

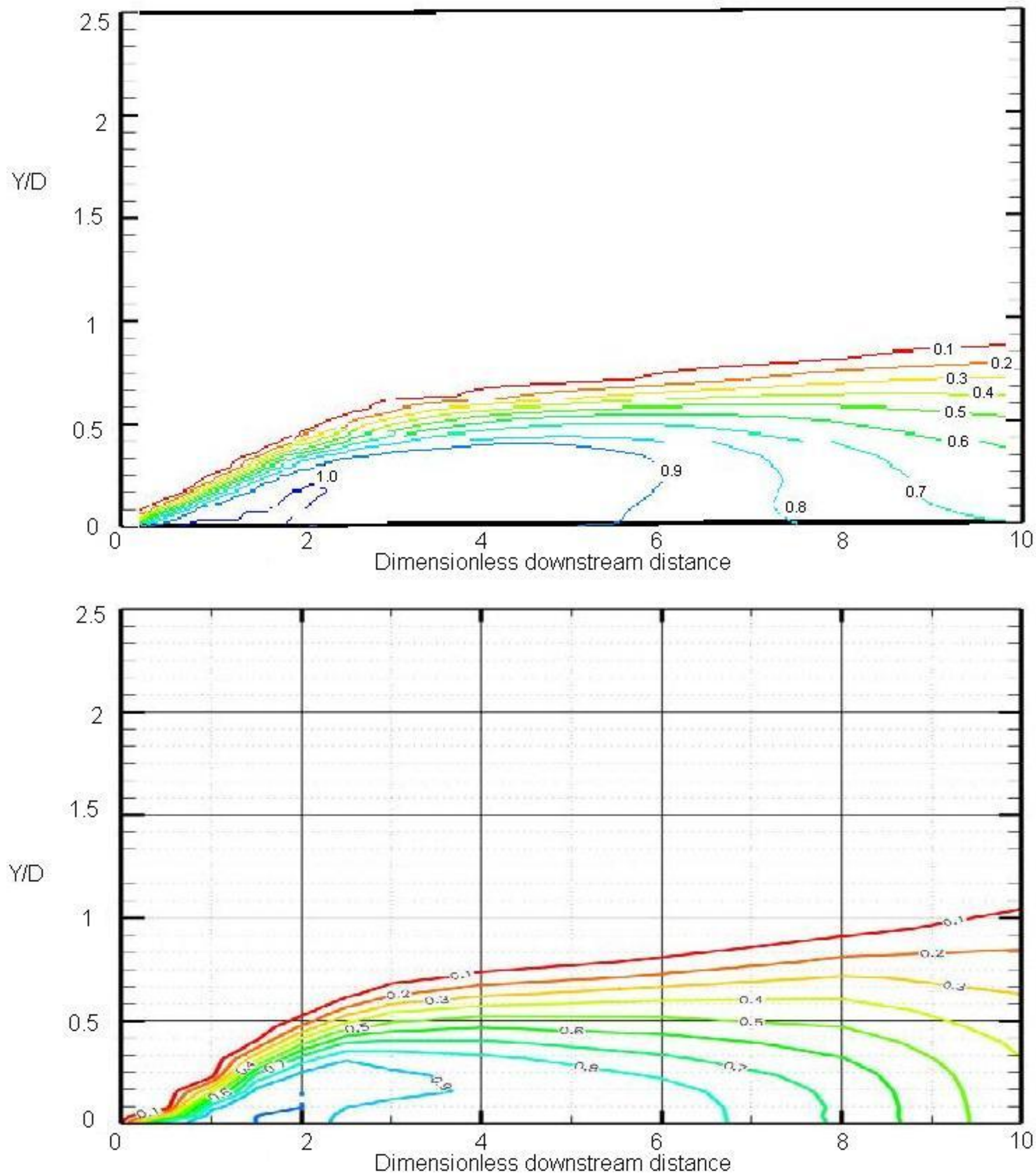

Figure 4.6 Comparison of centerline non dimensional temperature between experiment [50] (bottom) and simulation (top) for case 1 using k-ε turbulence model

4.4 Conclusions

Based on the results of this simulation it appears that the k-ε model is superior to the k-ω model for flows that involve rapid acceleration, high rates of strain and interaction of a jet with crossflow. A further comparison of the turbulence models for the case of a turbine stator vane is shown in appendix C. The k-ε model is found to provide a better fit to surface heat flux measurements than the k-ω model for the geometry of appendix C. In light of these conclusions, it was decided to utilize the k-ε model for the simulations of chapter 5. In addition to determining the choice of turbulence models this exercise was the first successful use of the preprocessor described in chapter 3 and appendix B.

Chapter 5: Unsteady Rotor-Stator Interaction

5.2 Details of numerical simulation

A highly loaded (pressure ratio across stage approximately 5.0) high pressure turbine stage [18] was used for this study. The stage consists of 38 stators and 72 rotors that rotate at approximately 9000 *rpm*. The rotor blade is highly three dimensional with a tip clearance 2.1% of the blade span. An O-H grid was generated using GridPro™ and results in $y^+<1$ near the wall. The domain was partitioned into 20 blocks for the rotor and 11 blocks for the stator. The grid consists of 2,461,740 cells of which 1,751,840 cells represent the rotor grid. In the radial direction 156 cells are used while 101 cells fill the rotor-to-rotor (circumferential) region. The grid density for the rotor passage is far greater than for the stator because there are more regions of interest that need to be resolved in the rotor passage. Figure 5.1 shows the grid on the rotor. Figure 5.2 shows the relative positions and sizes of the vane and rotor grids as well as the boundary conditions for the unsteady simulation. Previous studies such as the one by Green et al. [51] using coarser grids than the current grid have shown satisfactory results. Hence this grid is considered fine enough that no grid-refinement study was deemed necessary.

The unsteady simulation was run for approximately 11 complete revolutions of the rotor blade row. Convergence was monitored by observing mass-flow values at stator inlet and rotor exit. Surface heat transfer on the rotor blade was also monitored over several iterations. For the steady simulation, the solution was deemed converged when surface pressure and heat transfer, 1000 iterations apart, were nearly indistinguishable (percent difference under 0.1%). In both cases the solution was initialized ab initio.

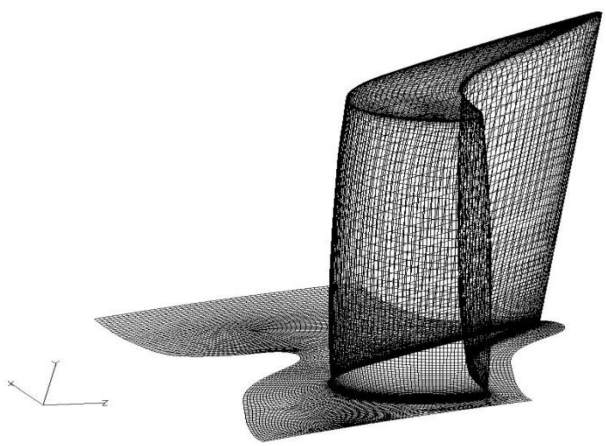

Figure 5.1 Rotor grid

The in-house developed preprocessor described in Chapter 4 was used to setup the case by converting GridPro™ connectivity and boundary information to a format compatible with TURBO. The Reynolds number of the flow is approximately $3x10^6$ per meter and is consistent with Tallman et al. [18]. An isothermal boundary condition (see Chapter 2) was used for all solid surfaces and the wall temperature was set to 0.7 times the reference temperature to simulate realistic flow conditions. Post processing and visualization in this study were realized through TecPlot™ and Fieldview™.

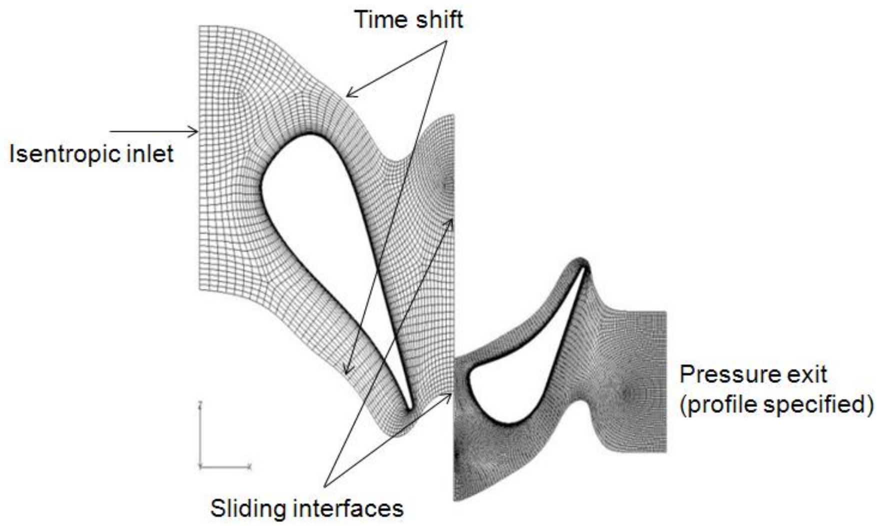

Figure 5.2 Boundary conditions

Steady simulation: For the steady simulation, the stator vane flow was first computed. At the vane inlet a temperature and pressure profile matching experimental conditions were imposed. The exit pressure profile was obtained from a coarse grid 1½ stage unsteady simulation [51]. The exit total pressure and temperature profiles obtained from the steady simulation of the vane were circumferentially averaged. The profiles thus obtained are radial and can be used as inlet profiles for the steady rotor simulation. Periodic boundaries were specified at the tangential boundaries. Results from this case can be found in Luk [19].

Unsteady simulation: An inlet profile of total temperature and total pressure upstream of the vane were specified based on the experimental data of Tallman et al. [18]. The radial static pressure distribution downstream of the blade was specified at the exit of the rotor blade row. This pressure distribution itself was a product of an unsteady computation for a 1½ stage simulation performed by Green [51]. Phase lag boundary condition was used in the tangential direction to account for unsteadiness and 31 time steps per period for the rotor were saved. This is approximately one fifth the number of time steps that were used to store time history information for phase lag. Phase lag assumes that a blade row is periodic with the frequency of wake passage of the neighboring blade row [23]. This requires that solution history be stored for one period of wake passing. At the stator-rotor interface, a sliding interface boundary condition was imposed. The code TURBO, in its present form, requires the grid lines at the stator exit and rotor inlet to match radially but does not require them to match in the tangential direction. Matching the radial grid lines at the interface can be achieved using the method shown in Chapter 3. The simulation took approximately 150,000 iterations to converge at a *CFL* of 5.0. Both simulations use the low Reynolds number k-ε model [24] (see appendix C and section 4.4 for turbulence model comparison.)

The results from the simulation are compared to the data presented in Tallman et al. [18] and to the steady simulations of Luk [19]. Tallman et al. [18] found that for the high pressure vane, downstream of the throat, steady CFD predictions matched well with experiment and therefore the effect of unsteadiness for this geometry is minimal. This was verified in the present work with the exception of density gradient oscillations due to reflection of the trailing edge shock from the downstream rotor. There was no significant change in time-averaged Stanton number or pressure and therefore, no results for the vane are presented here and the focus shall be on the high pressure rotor blade.

5.3 Rotor blade analysis

In the figures to follow, the abscissa is the normalized distance, *S*, along the blade surface with -1 to 0 representing the pressure surface from trailing edge to leading edge and 0 to 1 representing the suction surface from leading edge to trailing edge. This is shown in figure 5.3. Figures 5.4, 5.5 and 5.6 show the normalized pressure distribution along the blade surface at 5% span, 50% span and 90% span respectively.

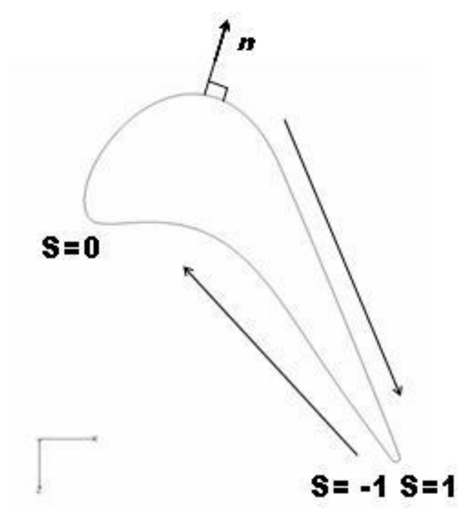

Figure 5.3 Rotor airfoil section showing non dimensional distance along blade surface

Figures 5.7,5.8 and 5.9 show Stanton number along the rotor blade surface at 15% span, 50% span and 90% span respectively. The Stanton number as presented is in reality a normalized wall heat flux. It is normalized by T_{wall} and T_{ref} which are both constants. A derivation of Stanton number is shown in section 1.2.

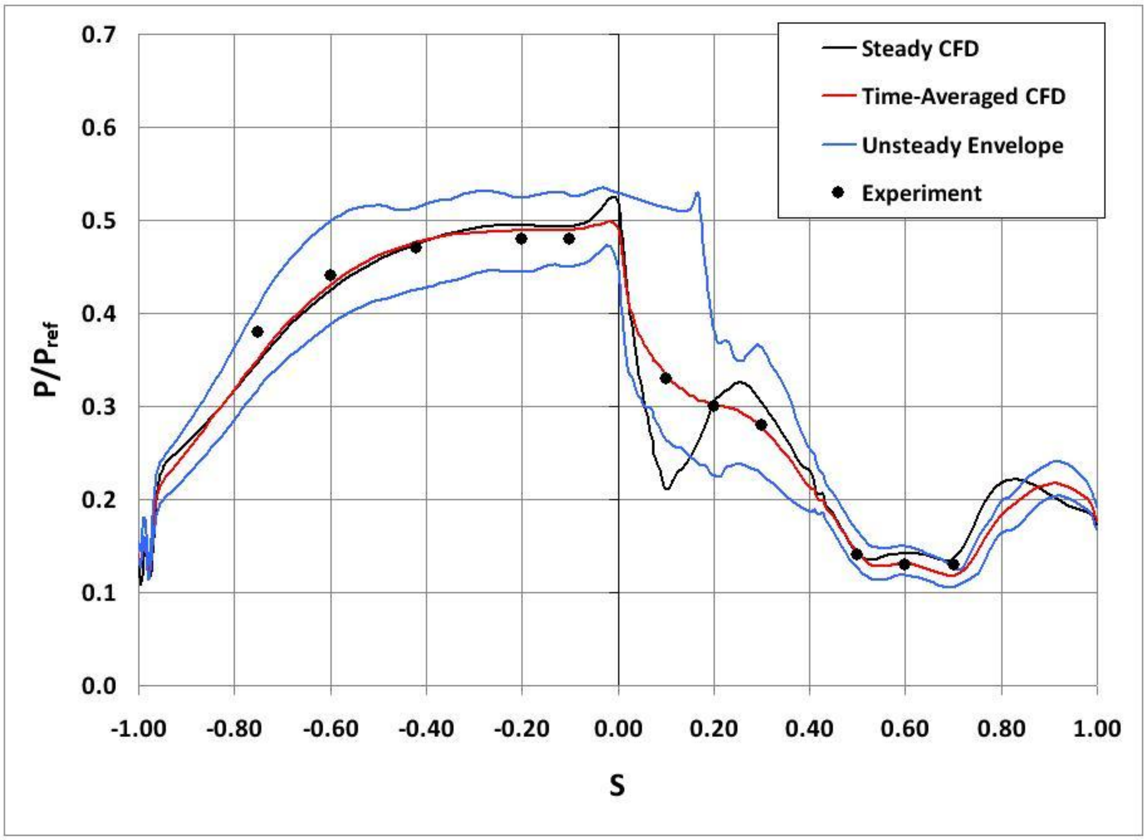

Figure 5.4 Pressure distribution at rotor 15% span

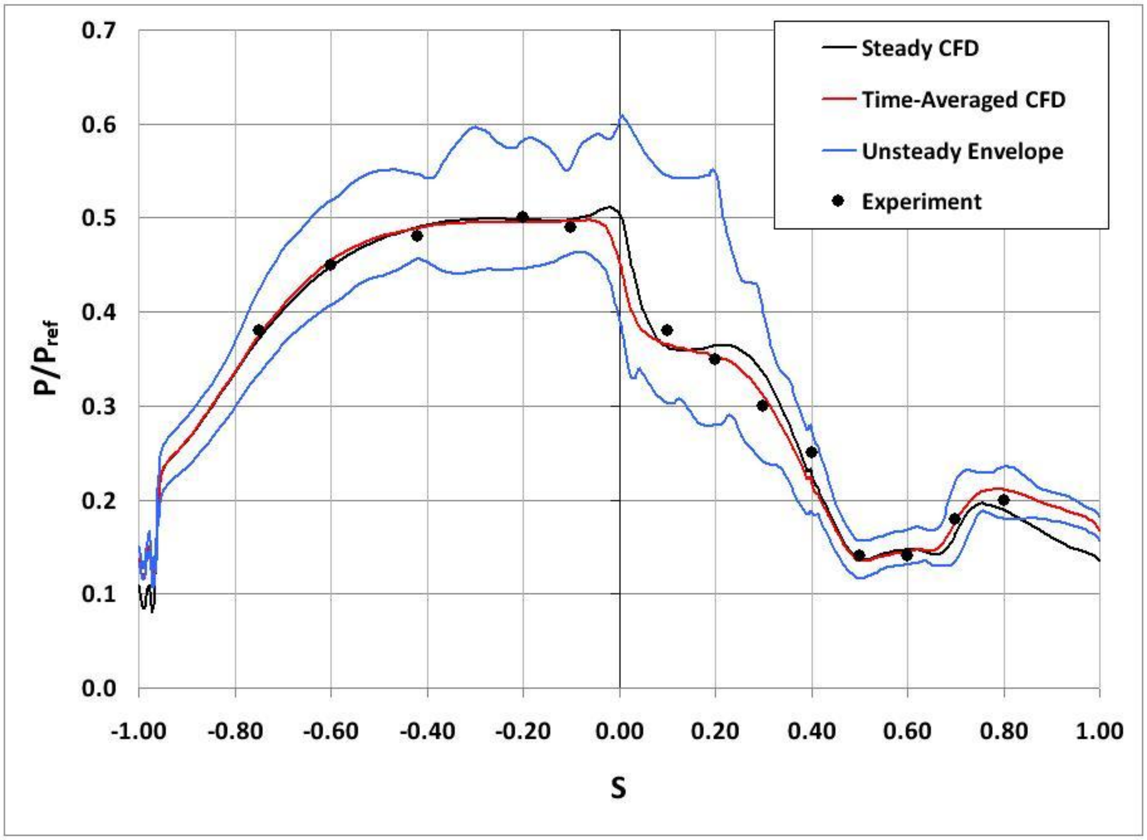

Figure 5.5 Pressure distribution at rotor 50% span

Overall, the time averaged pressure results match with the data better than the steady solution. In figure 5.4 at *S=0.1*, the time-averaged pressure profile captures the experimental data point that the steady solution misses. It appears from the thickness of the unsteady envelopes in figure 5.4 through 5.9 that at the 90% span the effect of unsteadiness is at its minimum. The widest envelopes are observed near the leading edge where the effect of the upstream wake is most prominent. There is also a wider unsteady envelop on the pressure side than on the suction side that is related to the wake fluid being more active.

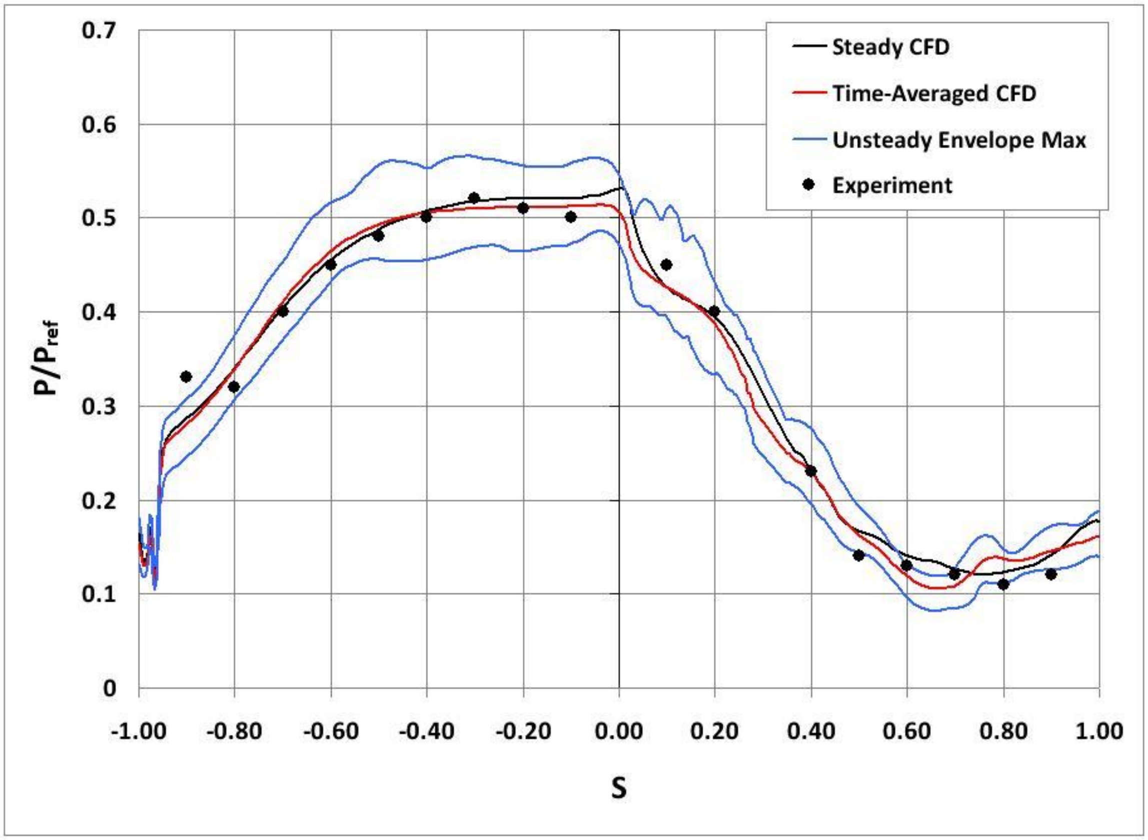

Figure 5.6 Pressure distribution at rotor 90% span

There is a shift in stagnation point to the pressure side for the time-averaged solution relative to the steady solution. This is due to the effect of the stator trailing edge wake. This is easily explained by looking at figure 1.6 that shows the segregation effect. While the relative velocity in the wake is oriented at a shallower angle for the time-averaged results compared to the steady results, the opposite is true of the free stream fluid. The free stream fluid is dominant due to the high Mach number of the flow and there is a net change in flow direction towards the pressure side. This is also why the wake fluid that is at a lower temperature than its steady analog does not have a significant effect downstream of the leading edge region, at least for the 0-90% span locations. As a result, the

Stanton number at the leading edge is lower for the time-averaged case but downstream of the leading edge, the Stanton number is higher for the time-averaged simulation. It appears that instead of segregating the cool and hot gas the flow has merely redistributed the thermal load. It is likely that thermal segregation would be more easily seen in simulations of turbine stages that are not as highly loaded or in simulations involving hot streaks. This would raise the entropy of the wake relative to the free stream making it easier to follow.

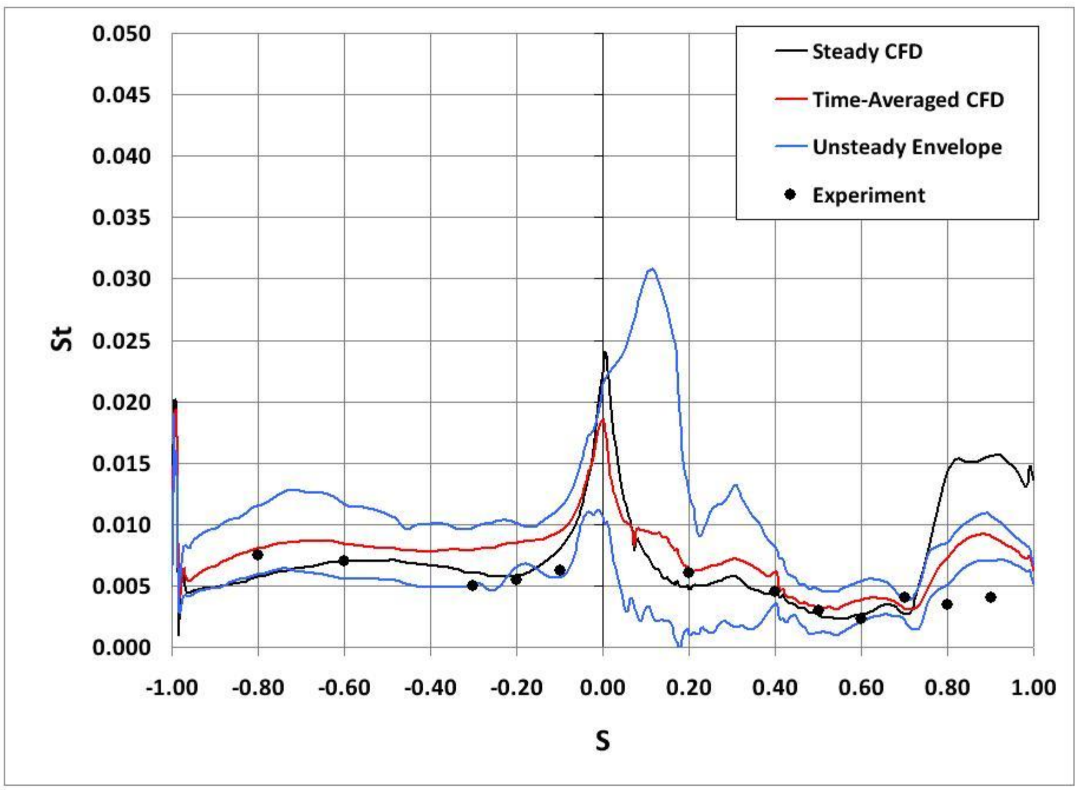

Figure 5.7 Stanton number distribution at rotor 15% span

Looking at figure 5.7, there is a sharp rise in Stanton number and pressure starting at *S=0.7,* on the suction side, at the 15% and mid-span locations. This is consistent with the rotor trailing edge shock. Downstream of the shock the heat flux drops as the boundary layer thickens once again. This abrupt rise due to the trailing edge shock is not visible at the 90% span location, possibly due to leakage at the tip that interacts with the trailing edge shock. At the 90% location (figure 5.9) there is however a sudden rise in Stanton number at *S=0.4.* This is not accompanied by a rise in pressure (figure 5.6). It appears that the increased heat flux is in a region where there is a thinning of the boundary layer that occurs as the subsonic flow in the region accelerates over the crown. This is accompanied by hot gases from the pressure side leaking onto the suction side through the tip gap. Figure 5.10 shows the flow features associated with this phenomenon.

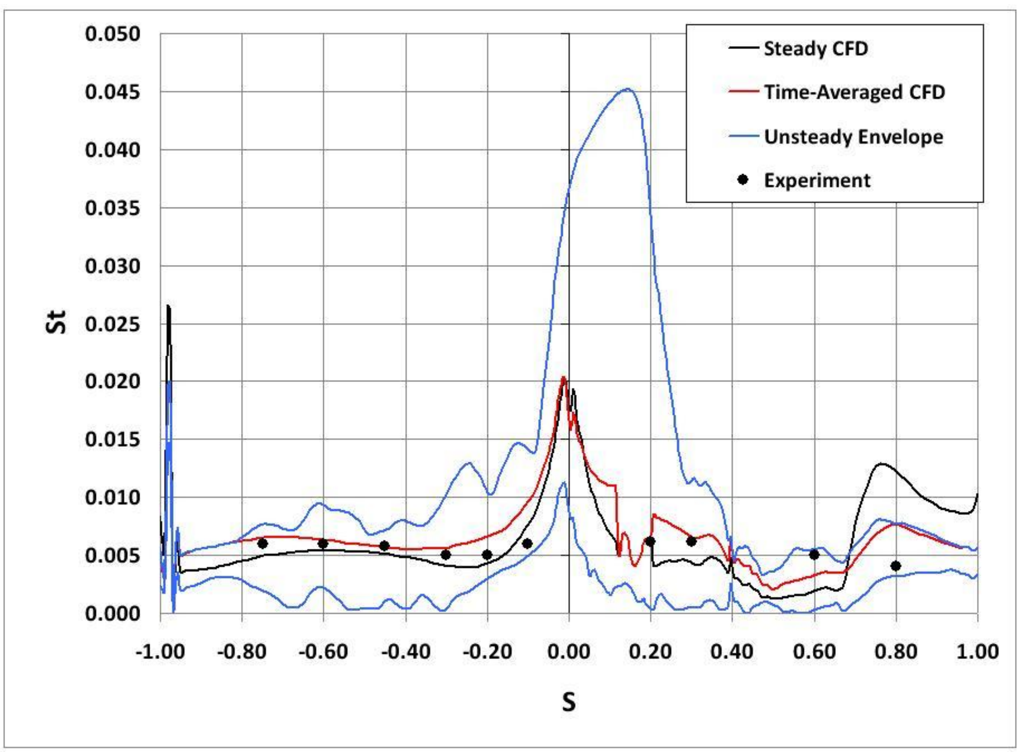

Figure 5.8 Stanton number distribution at rotor 50% span

Figure 5.11a shows the steady pressure distribution on the entire unfolded rotor blade. Figure 5.11b shows the time-average of unsteady pressure. It is clear that the effect of unsteadiness is observed mainly along the leading edge. Here, *R*, is the radial location and increases from hub to rotor tip.

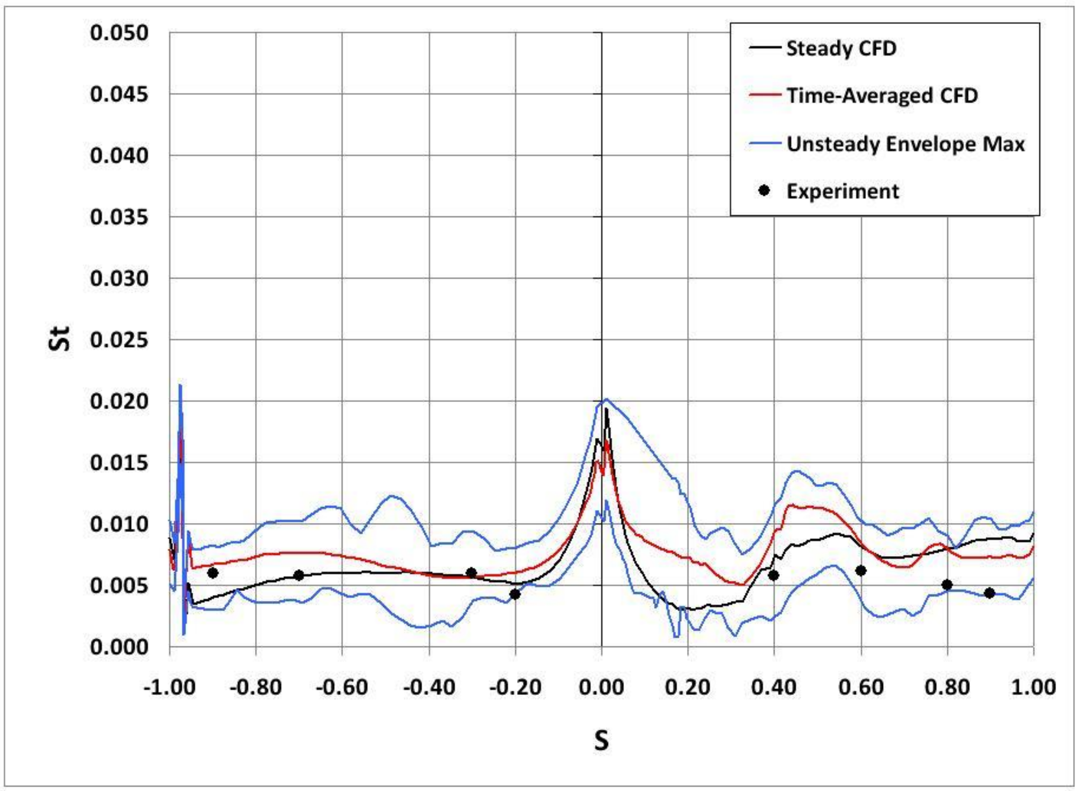

Figure 5.9 Stanton number distribution at rotor 90% span

Figure 5.12a shows the distribution of Stanton number on the rotor from the steady simulation and figure 5.12b shows the time-averaged Stanton number. Unlike in the case of pressure, the overall Stanton number levels are higher for the time-averaged case over most of the rotor blade surface. This observation is not consistent with that of Ameri et al. [14] who observed that the pressure side heat flux alone was higher. This could be due to the fact that unlike the simulations conducted in the present work, those of Ameri et al. [14] were for a lower stage loading. This would allow the wake to have an impact on the thermal loading downstream of the rotor leading edge and crown region. At the leading edge the steady simulation predicts higher heat transfer than the unsteady simulation and this is in agreement with figures 5.6 through 5.8.

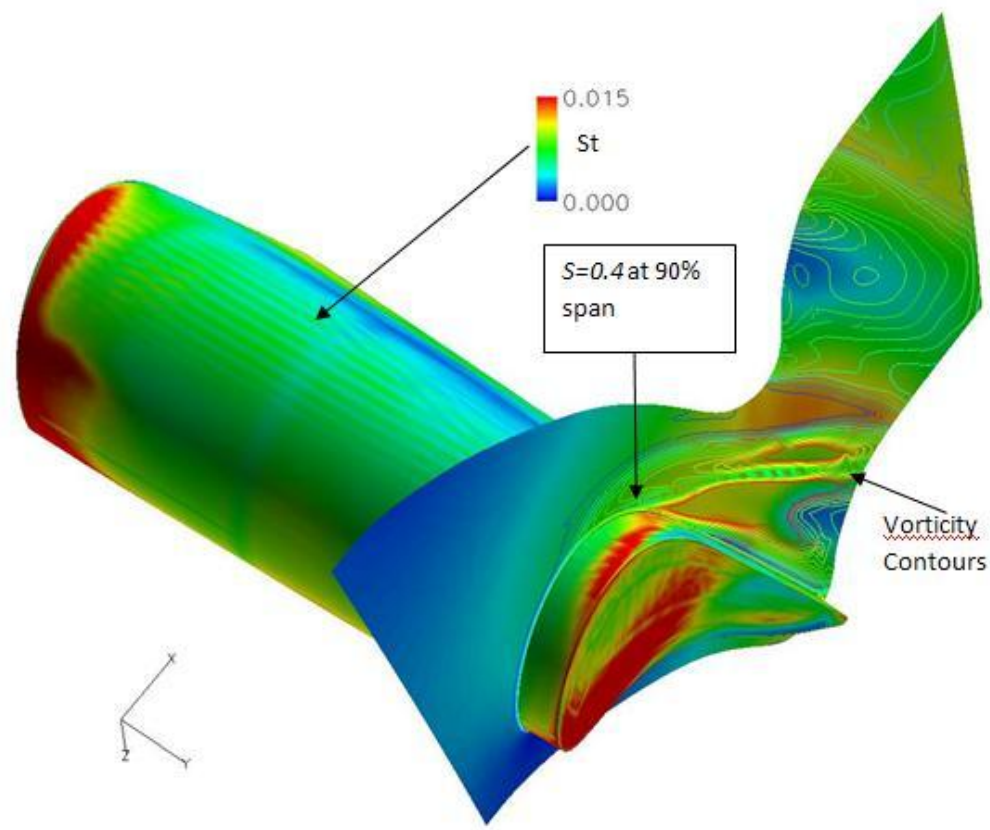

Figure 5.10 Stanton number rise due to leakage vortex

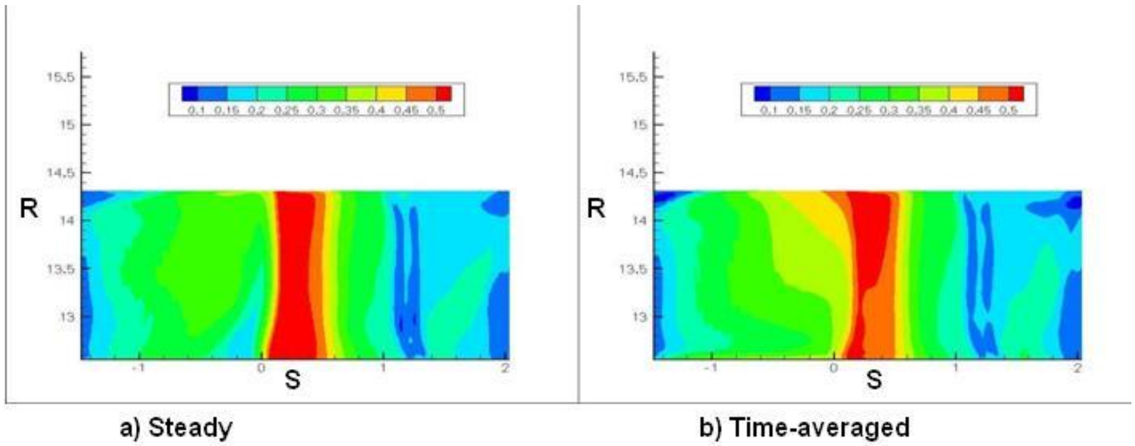

Figure 5.11 Pressure distribution on unfolded rotor blade surface

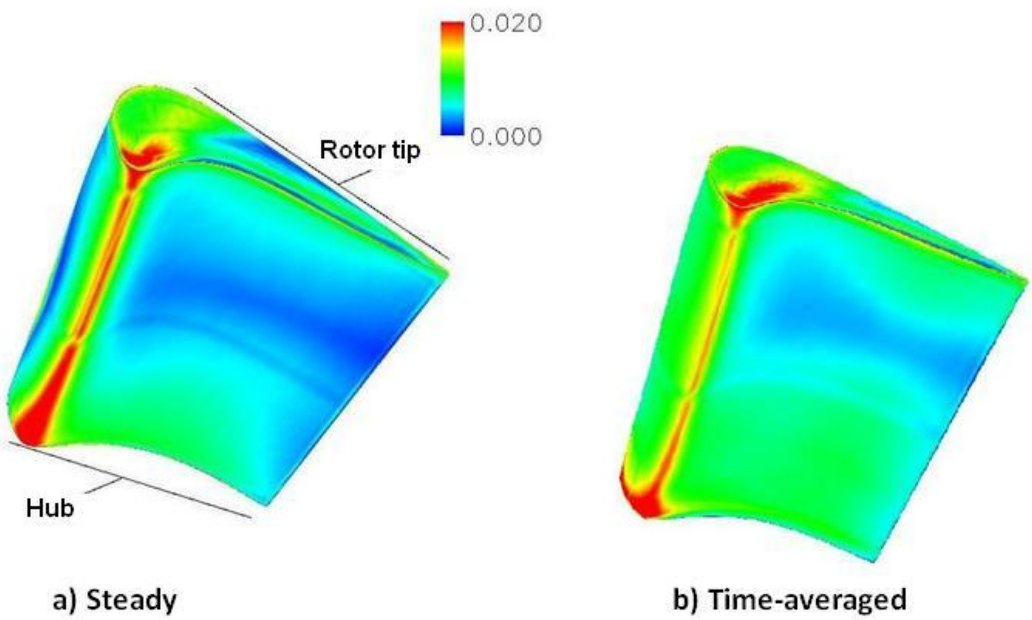

Figure 5.12 Comparison between steady and time-averaged Stanton number distribution on rotor blade pressure side.

Figure 5.13 shows streamlines over the suction side of the blade and the blade surface contours represent Stanton number. The heat transfer near the rotor tip is higher than over the remainder of the suction side. This is shown as a green streak starting near the rotor suction side leading edge and extending towards the trailing edge and radially towards the hub. This is caused by the scrubbing action of the tip leakage vortex as well as due to the high temperature gas within it which is sucked onto the suction side. The tip vortex can be seen and so can the streamlines near the hub that move radially toward the casing. The pattern of heat transfer distribution on the rotor blade (as seen in figures 3 and 5) is different for the steady case and for the time-averaged unsteady case. This could be caused due to thermal redistribution [14], [15].

Looking at figures 5.3 through 5.5 and figure 5.11, the pressure distribution appears to be radial for a large portion of the blade except near the tip and the hub where it is highly three dimensional due to the interaction of the passage flow with secondary flows from the hub and tip. The Stanton number, however exhibits a more three dimensional distribution. This is consistent with the findings of Tallman et al. [18]. Figure 5.14 shows the horseshoe vortex on the suction side of the rotor and the associated high Stanton number in the crown region of the rotor blade. The vectors show relative velocity. Secondary flow from the pressure side of the adjacent rotor blade can be seen traveling towards the suction side close to the hub (bottom left of figure 5.14) and towards the middle of the suction side passage.

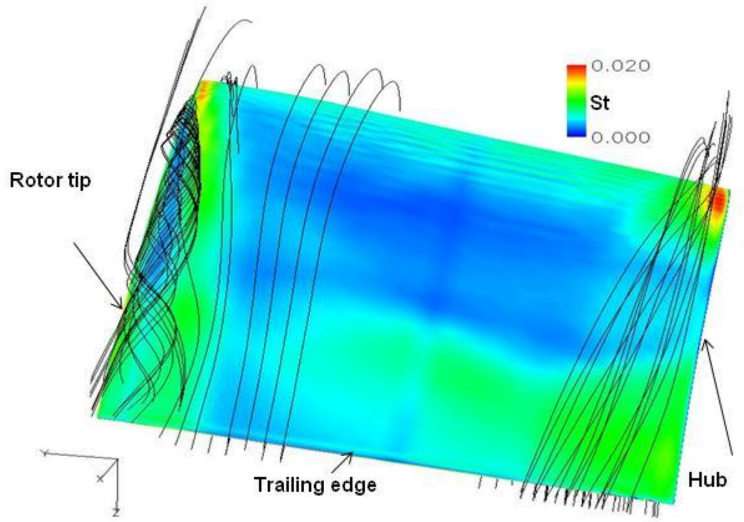

Figure 5.13 Streamlines of absolute velocity over suction side of rotor showing contours of Stanton number

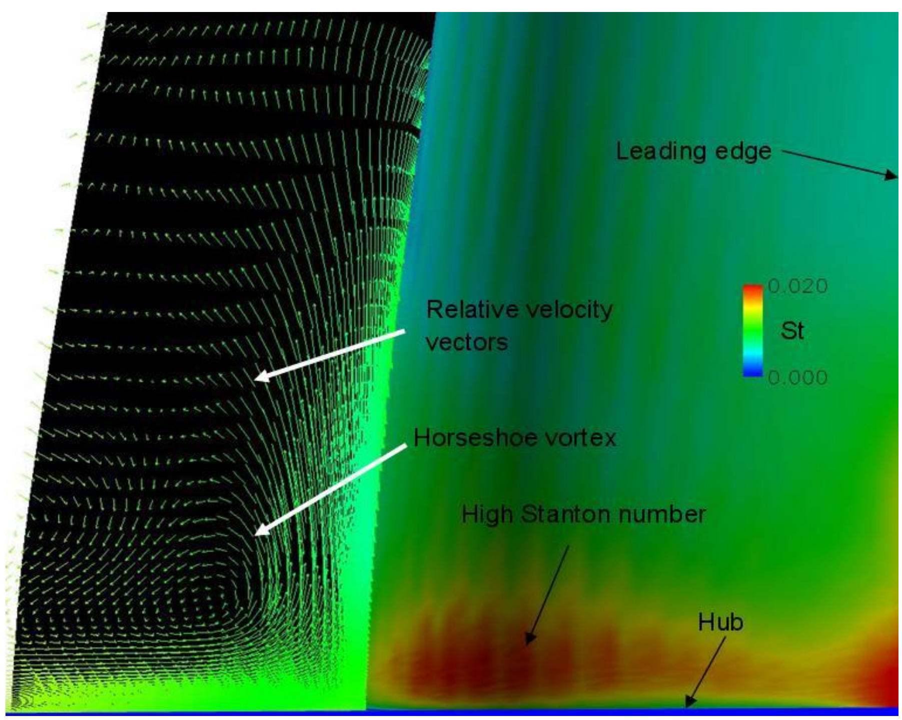

Figure 5.14 Horseshoe vortex looking downstream at suction side of blade near hub.

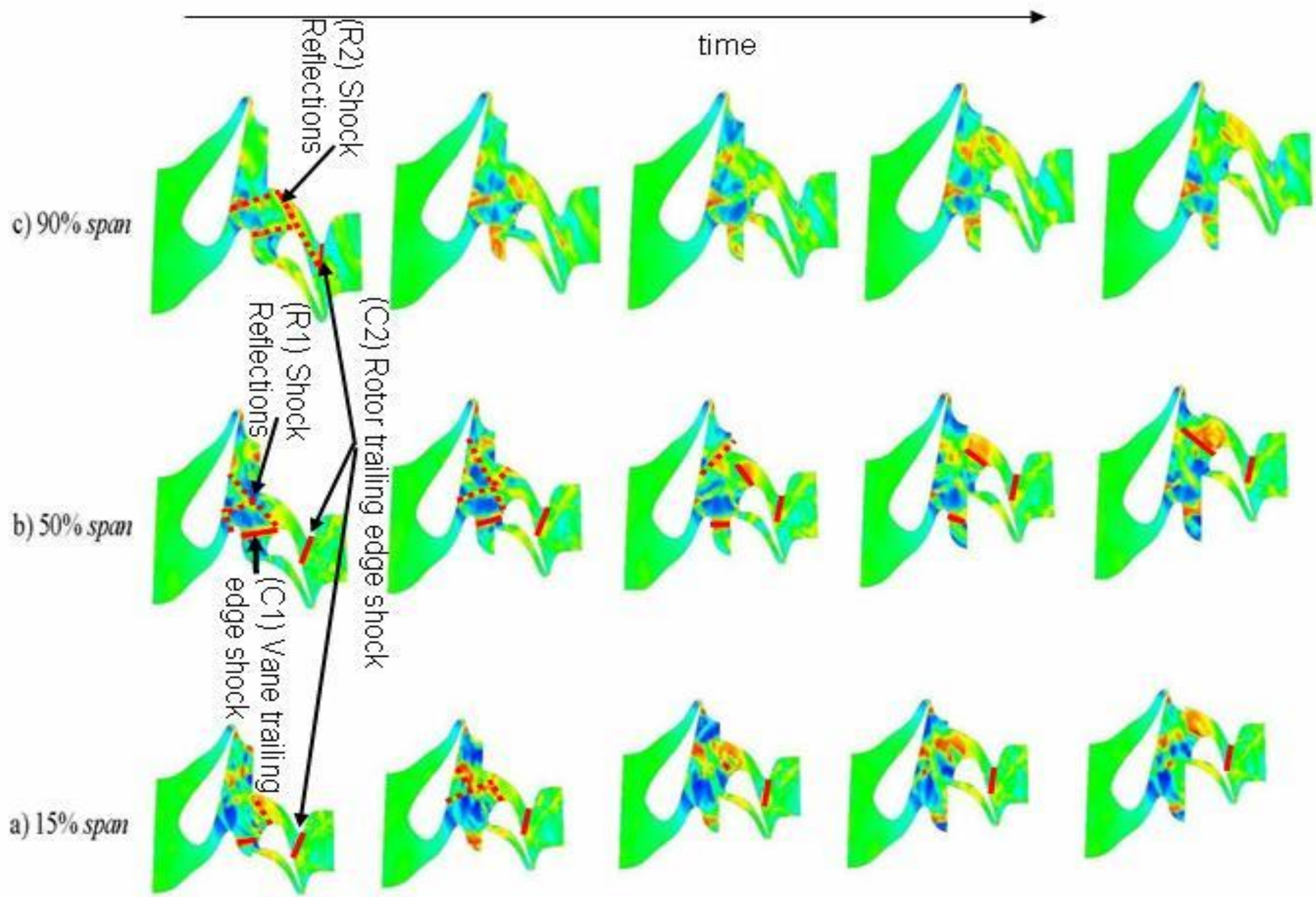

Figure 5.15. Snapshots of unsteady shock function at a) 15% span, b) 50% span and c) 90% span

Figure 5.15 shows filled-in-contours of shock function ($\vec{V} \cdot \nabla p$) at five different moments in time (time increasing from top to bottom). The three sections shown in this figure are at a) 15% span, b) 50% span and c) 90% span of the rotor blade. The shock function shows regions of large pressure gradients in the direction of velocity. So, the boundaries of regions colored in red are shocks while boundaries of regions colored in blue are expansions. Figure 5.16 shows filled-in-contours of shock function from the steady simulation at the same location. The steady solution shows that the shock, C1, is close to the crown of the rotor blade. In figures 5.15 and 5.16 some of the shocks and expansions have been marked with red and blue lines respectively. The shock at the rotor leading edge, C1, moves from the crown on the suction side down towards the leading edge and weakens as it does so. This phenomenon has been reported on by several authors including Denos et al. [11] and Giles [12]. Close to the tip region, the shock begins to weaken and does not travel as much from the crown towards the leading edge. The rotor trailing edge shock at 90% span interacts with the reflections of the shock from the upstream vane as well as the leakage vortex and dissipates before making contact with the suction side of the rotor. At the leading edge, the passing of the upstream vanes causes a series of expansions and shocks. There are several reflections of the shock back and forth between the rotor and the upstream stator. These are labeled R1 (dashed red lines) in figure 5.15. This is similar to the images shown in De la Loma et al. [52] that show incident and reflected shocks between the stator and rotor. One of these images is shown in figure 5.17. The rotor trailing edge shock, C3, is well defined in both the steady and unsteady simulations and appears to be a steady phenomenon. The leading edge shock weakens in strength from the hub to the tip.

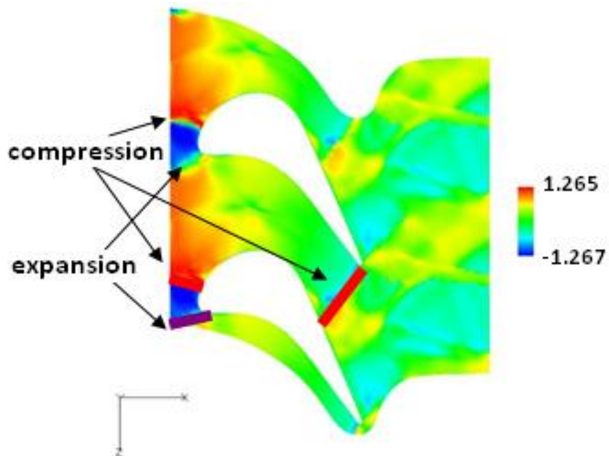

Figure 5.16 Steady shock function at rotor mid-span

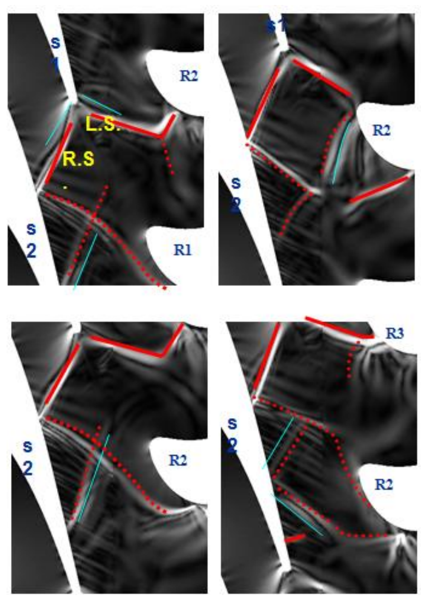

Figure 5.17 Schlieren visualization of stator-rotor shock interaction [52]

It should be noted that the shock function images are in the absolute frame of reference. This means that although the free stream flow undergoes several shocks and expansions, the rotor blade Stanton number itself is not necessarily affected by the interaction of the shocks. The periodic sweeping of the crown and leading edge by regions of high Stanton number as shown in figure 5.18 is however related to the sweeping of the vane trailing edge shock.

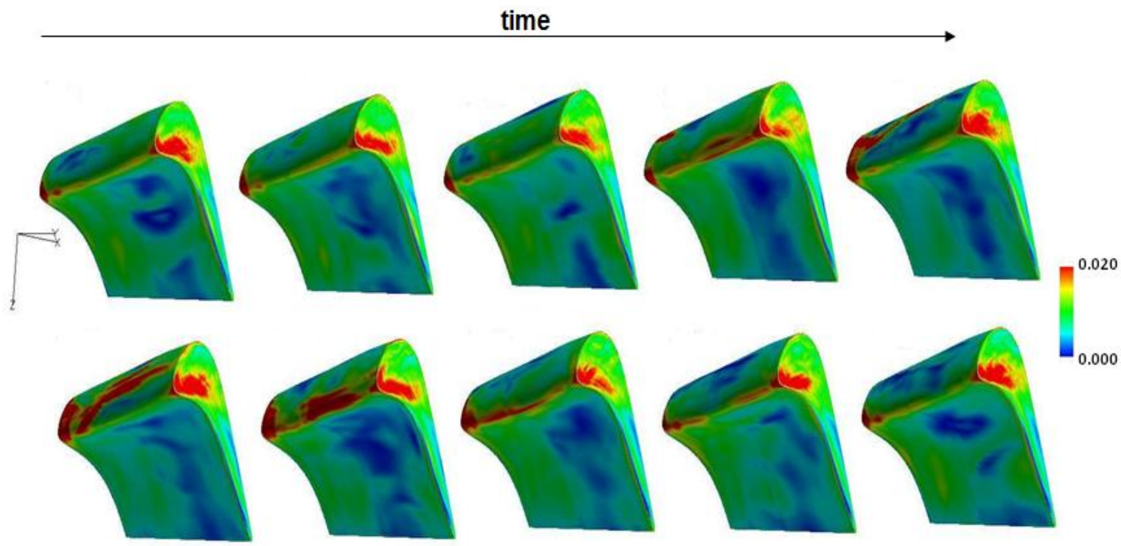

Figure 5.18 Stanton number at various instances in time on the rotor blade

Figure 5.18 shows Stanton number on the rotor surface at several instances in time. In the figure, the time sequence progresses from left to right on the upper row and then left to right on the lower row. It appears that at the hub and tip, the unsteady envelope is not as wide as elsewhere on the blade. The incoming thermal wake can be seen periodically washing over the suction side towards the leading edge causing a diffused spread of heat flux at the leading edge compared to the steady solution where heat flux is much more concentrated at the leading edge. The steady analogue in figure 5.12a shows a much higher heat transfer at the leading edge and lower heat transfer on the tip, near the leading edge. At the hub the heat transfer is much higher due to the interaction of the hub boundary layer with the passage flow, also known as the horseshoe vortex (see [53] and figure 5.14). This region seems to be unaffected by unsteady effects. The relative Mach number in the leading edge and crown regions of the rotor are very low. The high density gradients and associated shocks do not therefore have a significant impact on the heat flux in this region.

5.4 Tip flow and heat transfer

Tip heat transfer is thought to be largely a steady phenomenon dictated by tip geometry. In the experiments of Tallman et al. [18], tip heat flux was measured at several locations. Figure 5.19 shows these probe locations on the tip surface that is colored by Stanton number from the steady simulation. Figure 5.20 shows a comparison between simulated heat flux and heat flux measured from experiment at the probe locations shown in figure 5.19.

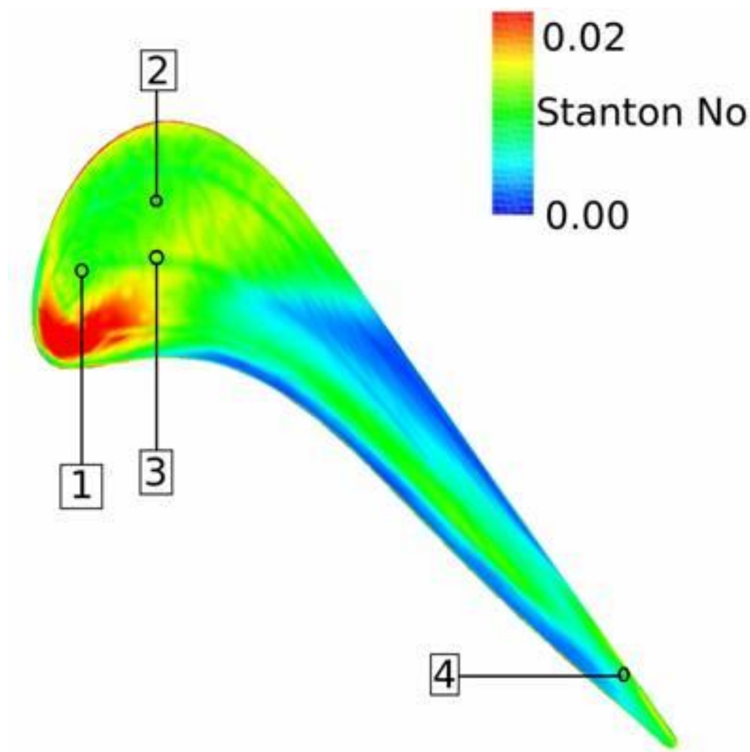

Figure 5.19 Location of probes to measure tip heat flux

Both the steady and time-averaged simulations over predict heat flux in the leading edge region of the tip while the predictions at the trailing edge lie within the two data points obtained from experiment. It is likely that the leading edge region of the tip is experiencing laminar or transitional flow (associated with strong pressure gradient in the streamwise direction.) The CFD simulation assumes that the flow is fully turbulent and thus over predicts heat flux near the leading edge. Closer to the trailing edge, the flow is turbulent and this leads to a better match between simulation and experiment.

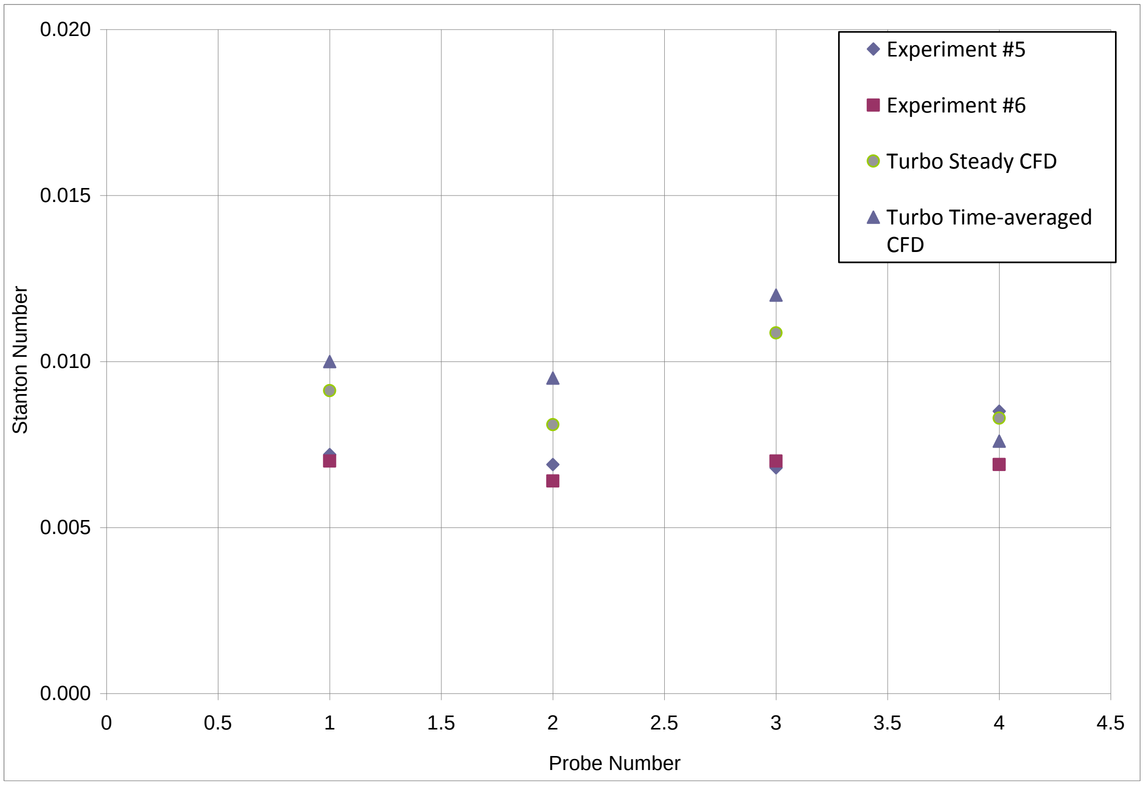

Figure 5.20 Tip heat flux comparison between CFD and experiment

The blue stripes of low Stanton number on the tip that are visible in figure 5.19 for the steady simulation, are also present in the results from the time-averaged simulation. The band of lower Stanton number at the entrance to the tip gap, from the pressure side is caused by separation bubbles in the tip gap. Figure 5.21 shows time averaged Stanton number on the tip surface along with two planes that are oriented in the streamwise direction.

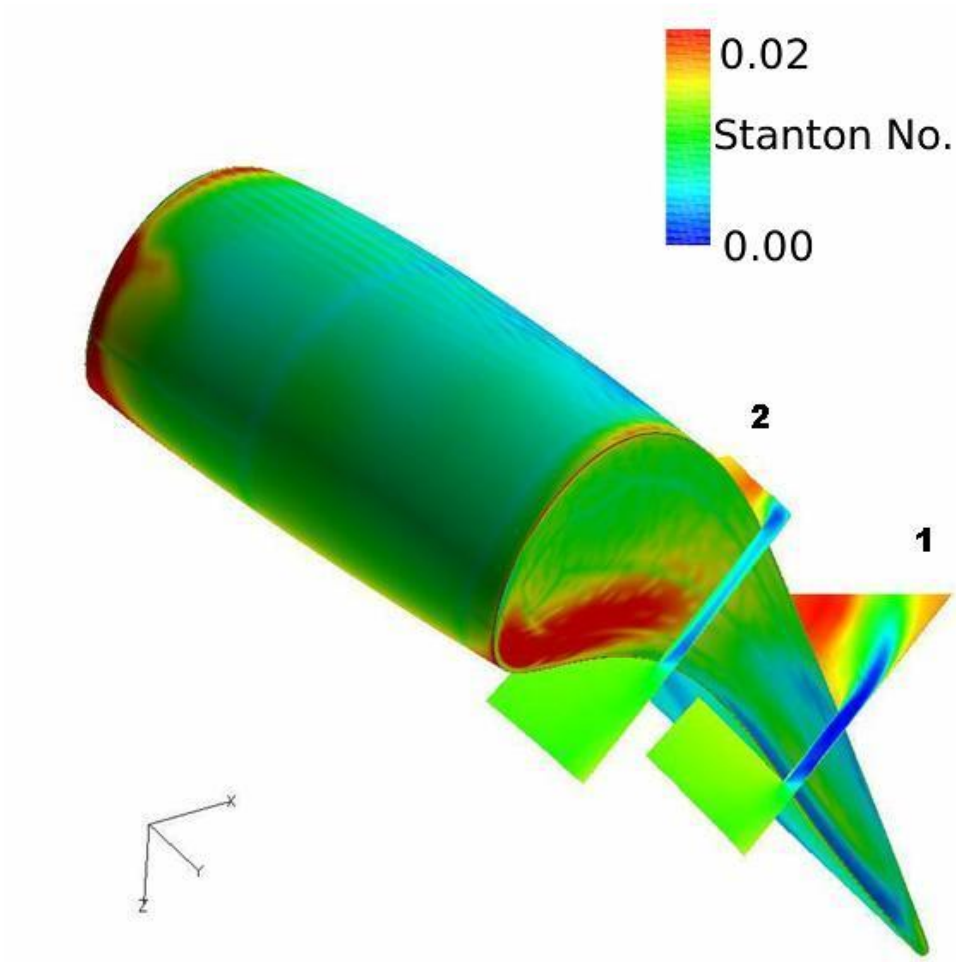

Figure 5.21 Time-averaged tip heat flux

Plane 1 is located in a region where the blue band of lower heat flux is present. Plane 2 is located in a region where the blue band of low heat flux on the tip is absent. Figure 5.22 shows a close-up view of flow along Plane 1. Plane 1 is colored by flow velocity. Blue and green indicate flow from pressure side to suction side and yellow and red indicate flow in the opposite direction (separated.)

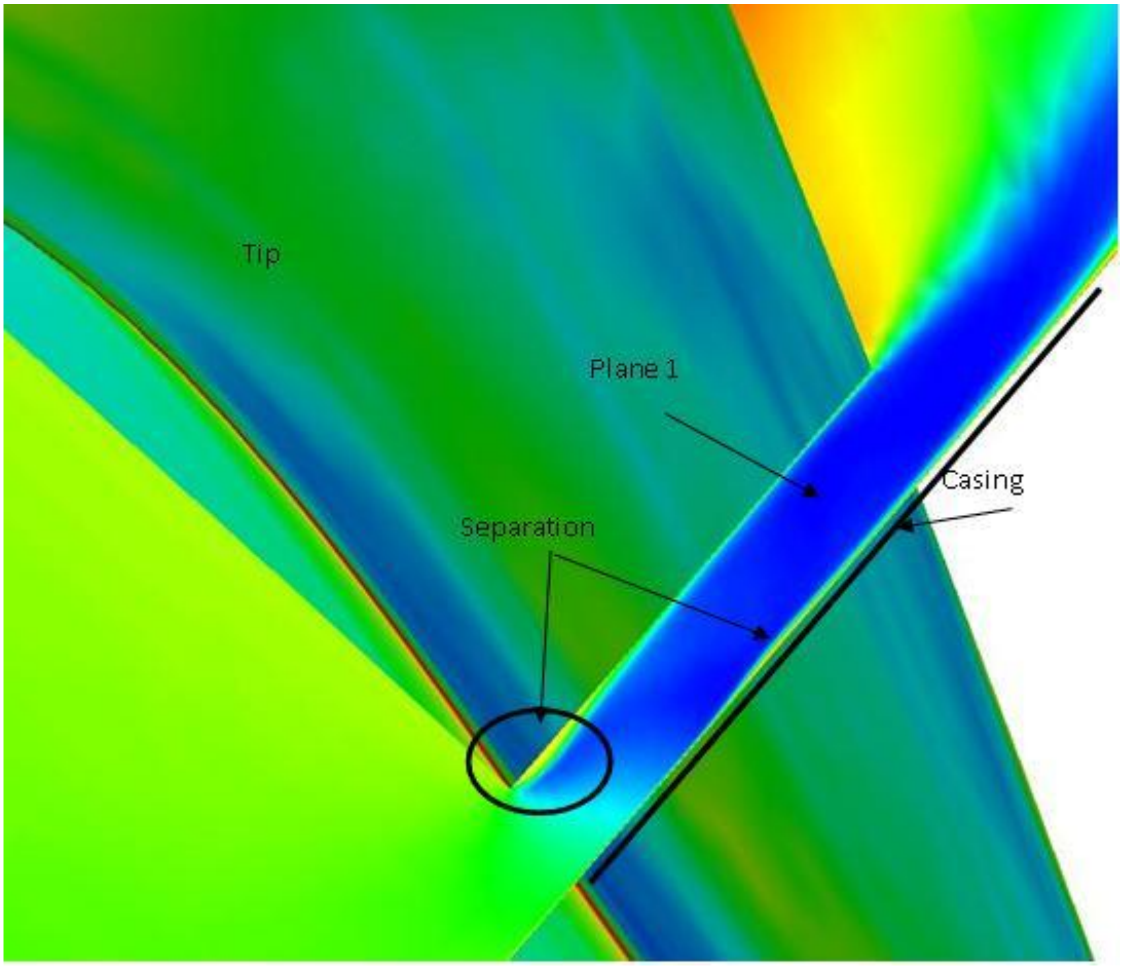

Figure 5.22 Plane 1 on the tip surface

Two distinct zones of separation are observed: one near the entrance to the tip gap form the pressure side and the other is midway through the tip gap on the casing. Figure 5.23 shows the region that is circled in figure 5.22 in greater detail to verify that the zone is in fact separated.

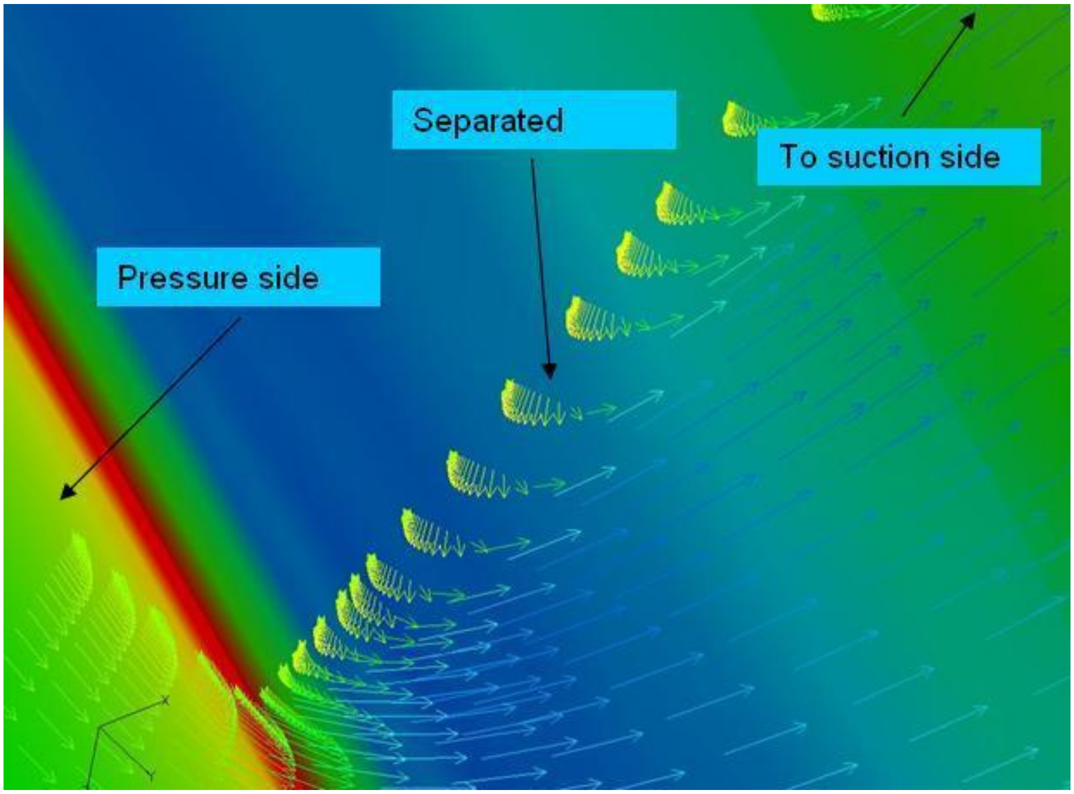

Figure 5.23 Zoomed in view of separated zone

The separation reduces the heat flux by keeping the hot flow from the pressure side away from the tip surface as well as by creating a much larger buffer zone between the tip and the hot gas than a boundary layer would. This separation zone is not seen in plane 2 that is shown in figure 5.24. The blue band on the tip surface that is closer to the tip exit, near the suction side of the blade, is caused by the development of the boundary layer on the tip surface as well a separation triggered by shock boundary layer interaction. The boundary layer is thickened due to the presence of shocks and this leads to a further reduction in surface heat flux. These shocks can be seen in figure 5.25 that shows density gradient contours along Plane 1 in the tip gap. The fluid from the pressure side over expands as it enters the tip gap and then goes through a series of shocks and expansions before a strong shock at the tip gap exit brings the pressure back to the level of the suction side.

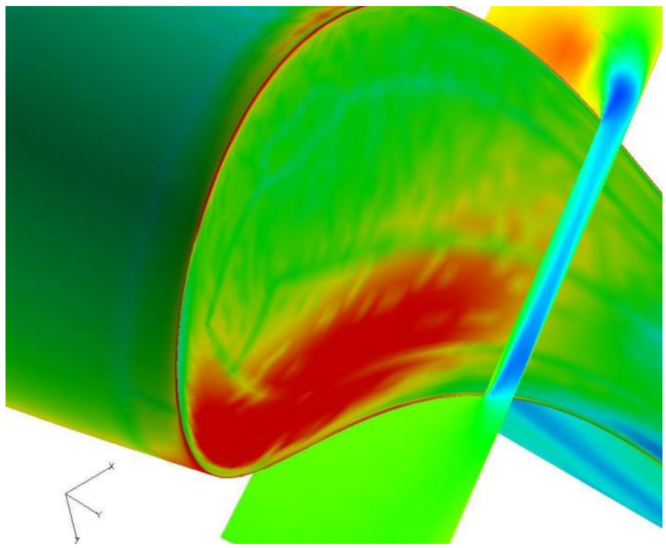

Figure 5.24 Plane 2 on the tip surface

While viewing videos of unsteady flow in the tip gap it was observed that there exists a region in the vicinity of Plane 1 where the heat flux rises to levels comparable to that at the leading edge. A snapshot from this video is shown in figure 5.26. Although the rise in heat flux is intermittent it could have a significant impact on the life of the blade material. The reattachment line is known to be associated with higher heat flux. However, the unsteadiness of this ‘hot spot’, as it shall henceforth be referred to, leads to the conclusion that there are other physical processes at work. It is interesting to note that the hot spot occurs downstream of an oblique shock. It also occurs when the shock is at its strongest. This is easily explained because a stronger shock would lead to the downstream relative Mach number being lower and therefore lead to a smaller boundary layer thickness. In addition, the stronger shock increases the temperature downstream of it causing higher heat flux to the surface.

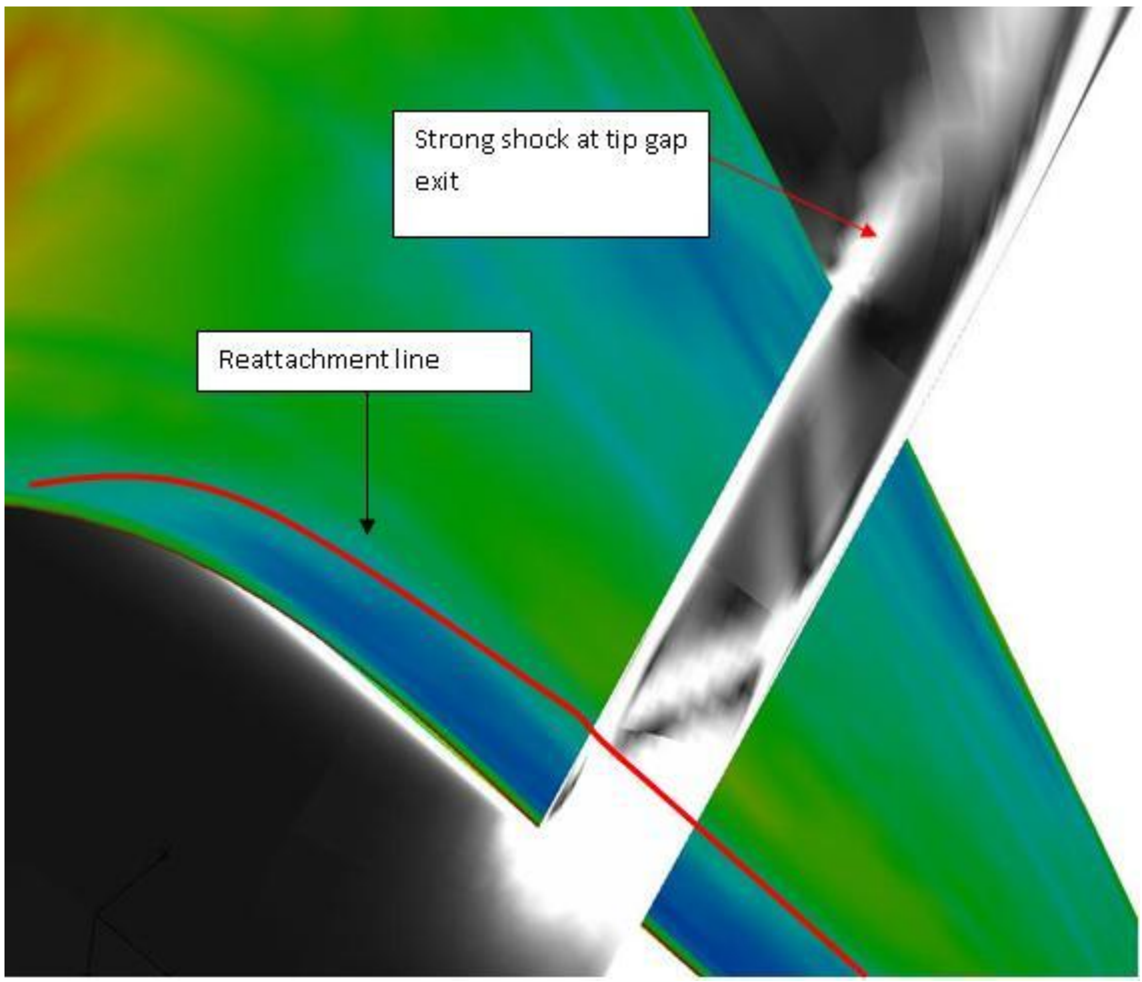

Figure 5.25 Compressions and expansions in the tip gap (Plane 1)

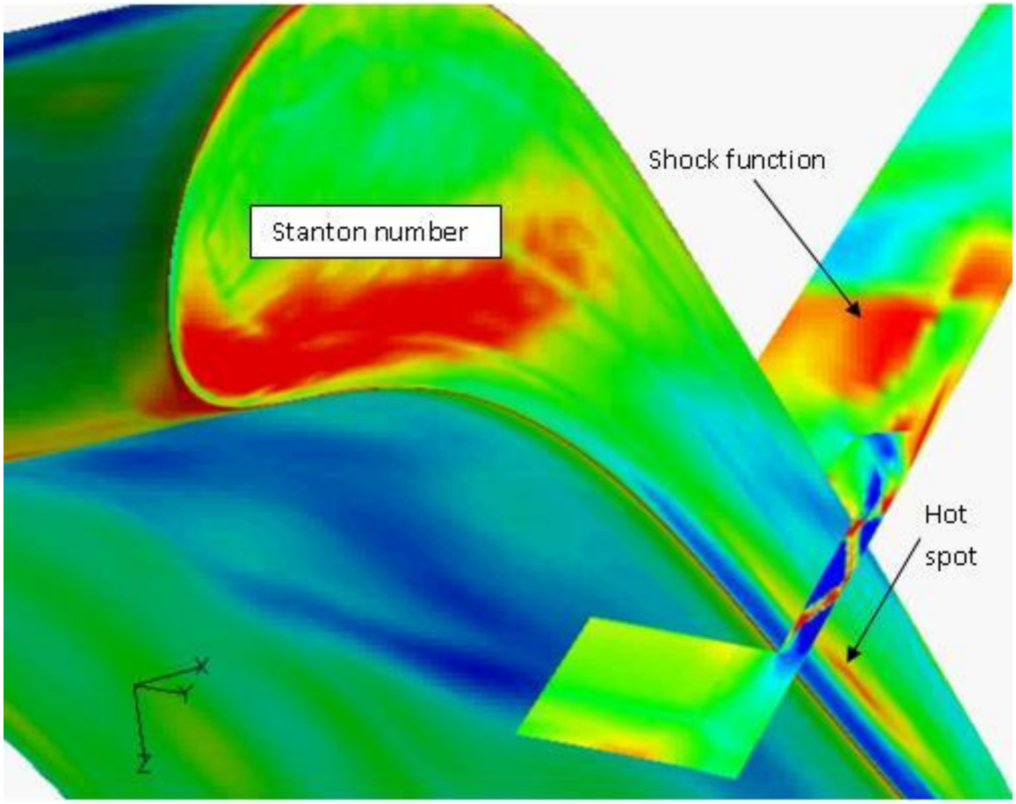

Figure 5.26 Discovery of ‘hot spot’

The levels of temperature, entropy, pressure and relative Mach number were analyzed before and during the hot spot. Table 5.1 shows the computed flow variables at two instances labeled 'before' and 'during' the hot spot. Station 2 refers to the tip gap entrance on the pressure side. Station 1 refers to the tip gap exit on the pressure side. Station 3 is located on the tip surface region where the hot spot is observed. The bubble height, δ_{bubble} is non-dimensionalized with tip gap height, *h*. Table 5.1 shows that an 8% drop in tip gap pressure ratio leads to a 25% drop in bubble height and a 64% increase in Stanton number on the tip surface at station 3. The stations referred to in table 5.1 are indicated in figures 5.27 and 5.28 that show density gradient in black and white with overlaid vorticity contours in the tip gap during the occurrence of the hot spot and before the occurrence of the hot spot respectively.

Table 5.1 Measurements across tip gap

Location	Station 1 Suction side				Station 2 Pressure side			Station 3 (surface)	Bubble height
	P_1	S_1	P_1/P_2	P_2	$M_{relative}$	S_2	S_1/S_2	St	δ_{bubble}/h
Before	0.167	0.35	0.41	0.41	0.6765	0.088	4.643	0.011	0.254
During	0.157	0.121	0.38	0.41	0.6917	0.031	12.31	0.018	0.1905
% difference	6.048	65.36	7.9	2.01	2.25	65.25	165	63.6364	25

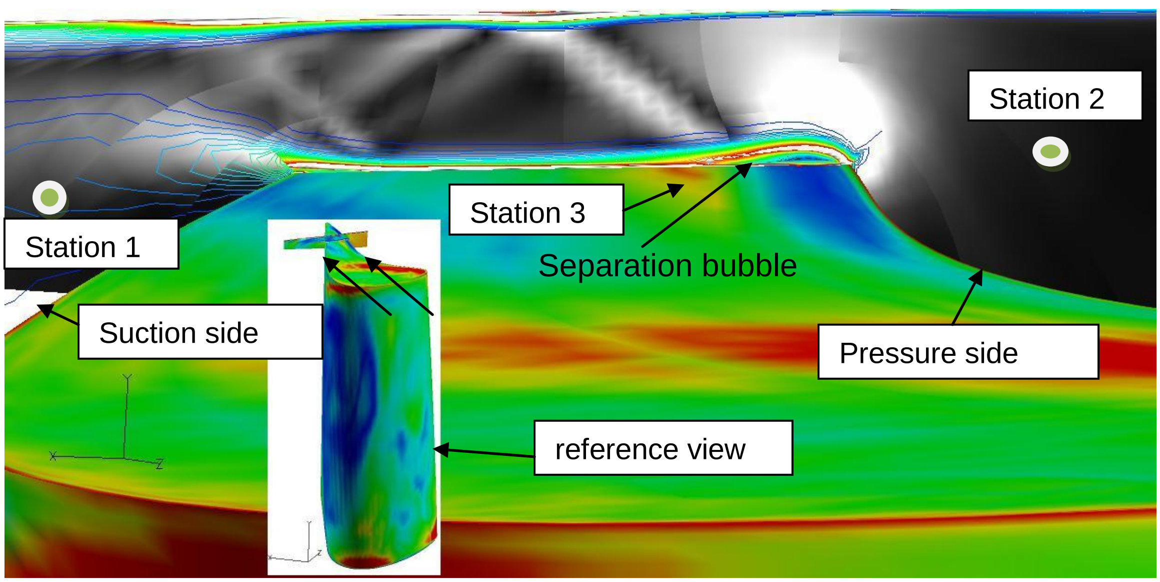

Figure 5.27 Tip gap during hot spot

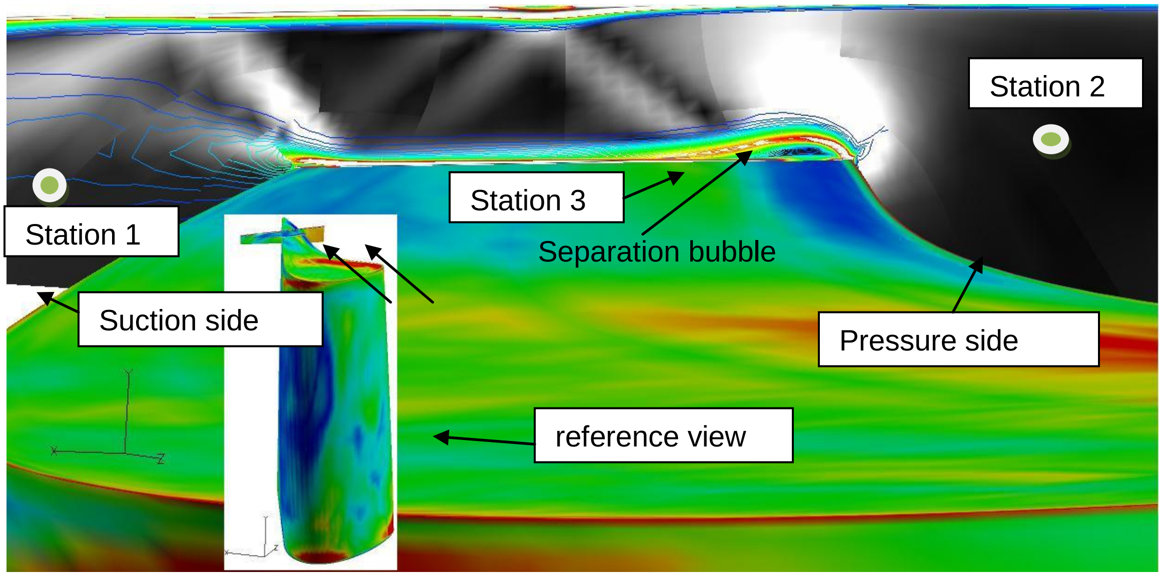

Figure 5.28 Tip gap before hot spot

The strength of the first oblique shock in the tip gap appears to be a strong function of separation bubble height. The bubble height depends on both the pressure ratio across the tip as well as the local Mach number. This is contrary to observations for subsonic flow regimes in the tip gap where separation and reattachment are brought about purely through the effects of turbulence. During the hot spot, the pressure ratio across the tip is higher than before the hot spot by approximately 8%. The relative Mach number entering the tip gap is also higher. This leads to the separation bubble being thinner at the tip entry during the hot spot and pushes the throat further into the tip gap. Once the throat is reached, the pressure ratio across the gap accelerates the flow much faster. The separation bubble thins more quickly at higher Mach numbers causing a more rapid expansion in effective tip area (see section 1.3, equations 1.10 and 1.11).

This in turn hastens reattachment by thinning the bubble height downstream of the throat. The higher the Mach number at reattachment, the stronger the shock and the greater the heat flux on the tip surface. The expansions that occur in the tip gap do increase the boundary layer thickness and therefore cause a reduction in heat flux further downstream in the tip gap. However, these expansions are weak and do not significantly change the pattern of heat flux on the tip surface. The shock at the tip gap exit triggers separation on the tip surface and causes a drop in heat flux. The primary oblique shock in the tip gap reflects off the casing and triggers another separation bubble on the casing. This separation bubble occurs downstream of the reattachment point on the tip surface and leads to a fairly constant area section in the tip gap that is terminated by a reflection from the casing separation bubble.

It is clear from table 5.1 that the hot spot is associated with periods of lower entropy in the free stream. In low Mach number flows, the entropy of the wake is usually higher than that of the surrounding fluid. However, because of the highly loaded nature of this stage, there is a large entropy rise in the free stream, downstream of the rotor inlet. This is also the reason why the temperature in the wake is higher than in the free stream (Although this has little effect downstream of the leading edge due to mixing). Following iso-surfaces of entropy, it was determined that the lower entropy is associated with the fluid from lower radial regions that is convected to the tip region due to unsteady radial pressure gradients. Figure 5.29 shows the streamline locations for the two instances in time: before the hot spot (top) and during the hot spot (bottom).

The existence of a throat leads to the conclusion that the flow through the tip gap is choked and that any rise in passage mass flow will reduce the relative tip losses. It is therefore possible to contour the tip gap in a manner that allows it to remain choked and simultaneously minimize tip heat flux. Ideally this could be accomplished by creating a diverging pathway for the tip flow to push the throat to the tip entrance. This would eliminate fluctuations of heat flux on the tip surface due to strengthening and weakening of oblique shocks. Alternatively, one could increase the separation bubble distance in the streamwise direction.

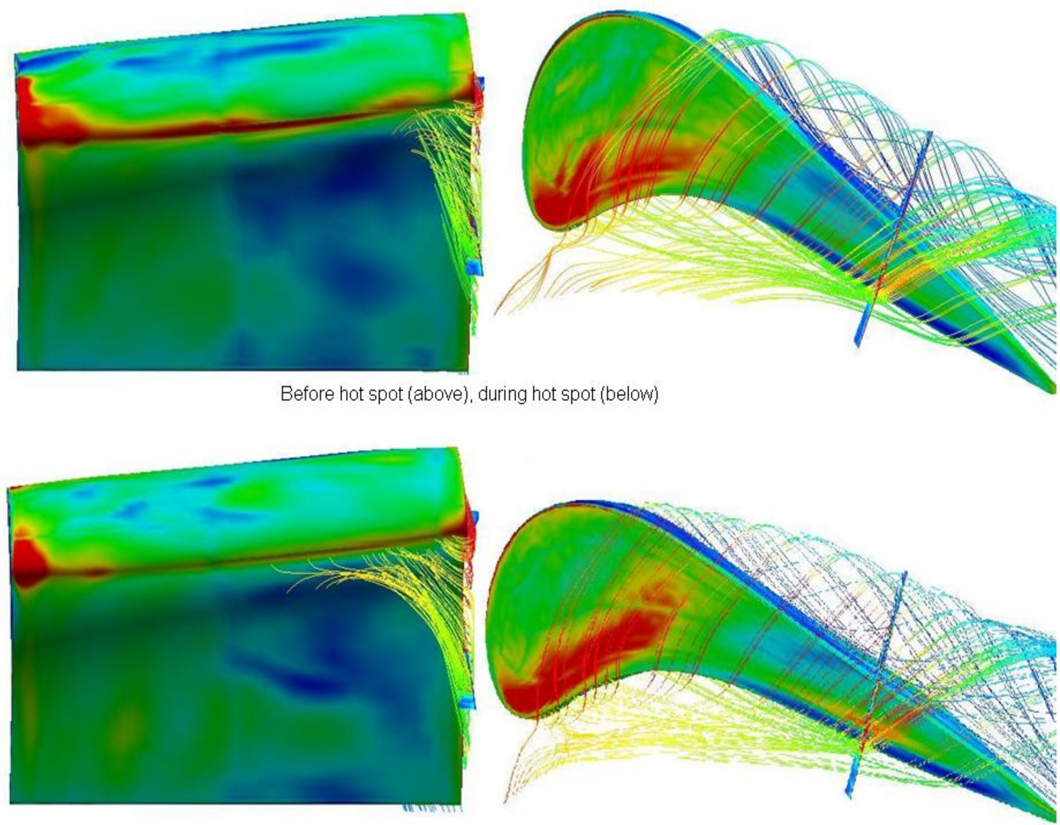

Figure 5.29 Streamlines through the tip gap before (top) and during (bottom) the hot spot

5.5 Endwall heat flux

Figure 5.30 shows the heat flux on the rotor hub for the steady (top) and time-averaged (bottom) simulations. The heat flux from the time-averaged simulation is higher than the heat flux from the steady simulation near the leading edge on the suction side while it is lower on the pressure side. This thermal redistribution has been discussed earlier in section 5.3.

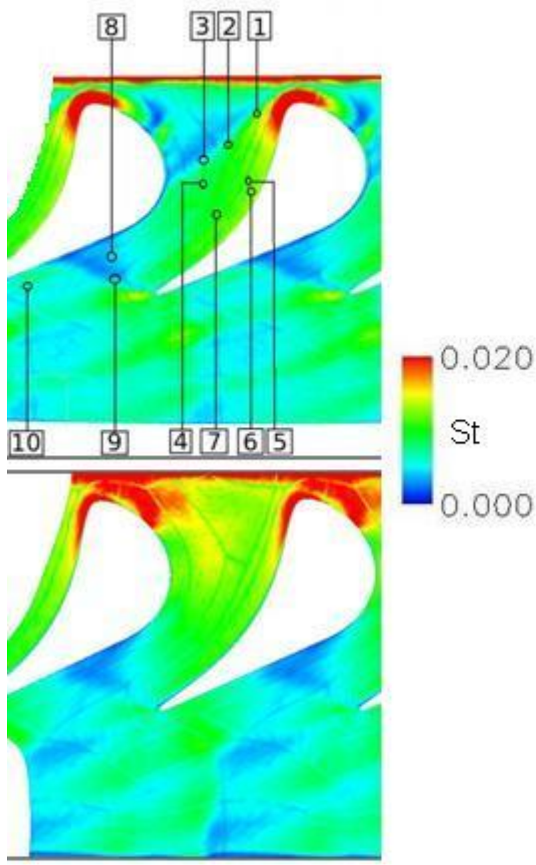

Figure 5.30 Hub heat flux for steady (top) and time-averaged (bottom) simulations

Figure 5.30 also shows the location of probes at which heat flux was measured during the experiment [18]. The pattern of heat transfer shown in figure 5.30 is consistent with the work of Ameri et al. [54]. Figure 5.31 shows a comparison between the heat flux predicted by CFD and that obtained by experiment.

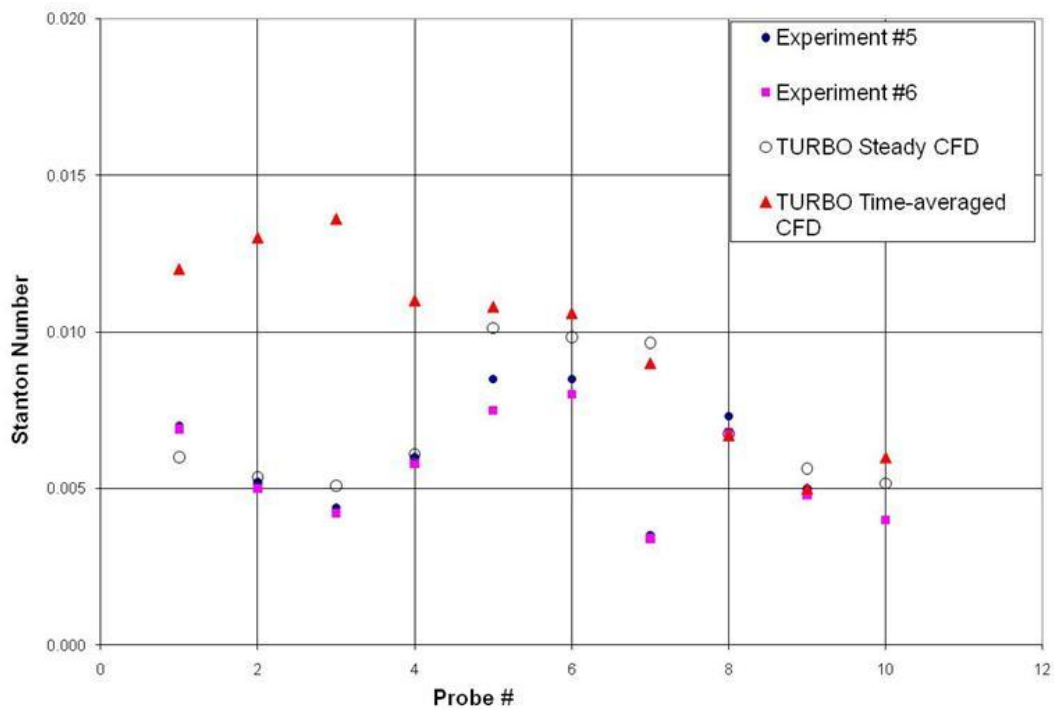

Figure 5.31 Hub heat flux: comparison between CFD and experiment

On the hub, near the leading edge, there is almost a 100% difference between the steady and time-averaged simulations. This is partly due to the effect of the wake that interacts with the hub boundary layer. Another reason for this difference is that the boundary layer for the steady simulation is rather flat. This is because the inlet profile is defined in a coarse manner that does not accurately capture the turbulent boundary layer in the manner that the time-averaged simulation does. This is why the heat flux computed by the steady simulation in the leading edge region of the hub matches the heat flux measured by experiment. The CFD simulation is fully turbulent and therefore the time-averaged simulation that is able to pass boundary layer information across the sliding interface, over predicts heat flux in the leading edge region of the hub. The 100% over prediction is indicative of the fact that the flow in this region is probably laminar. Toward the aft section of the hub the CFD predictions match very well with the experiment because the flow has now become fully turbulent. Figure 5.32 shows the shape of the inlet boundary layer for the steady (left) and the time-averaged (right) simulations.

Figure 5.33 shows heat flux on the rotor casing for the steady and time-averaged simulations. On the casing, due to the clearance flow the heat transfer is seen to be higher than on the hub especially in the region adjacent to the pressure side of the blade. This is probably because the hot air from the pressure side is being sucked towards the suction side and heats up the casing as it travels through the tip gap by the scrubbing action of the tip leakage flow. The blue strip that follows it is associated with the separation zone described in section 5.3 and illustrated in figure 5.22. The difference in blade passing frequency between the steady and time-averaged simulations also leads to a phase-shift in the heat transfer pattern on the casing as seen in figure 5.34 that shows the percent difference between steady and time-averaged heat flux predictions on the casing. Percent difference is computed as,

$$\Delta_{St} = \frac{St_{steady} - St_{time-averaged}}{St_{time-averaged}} \times 100$$

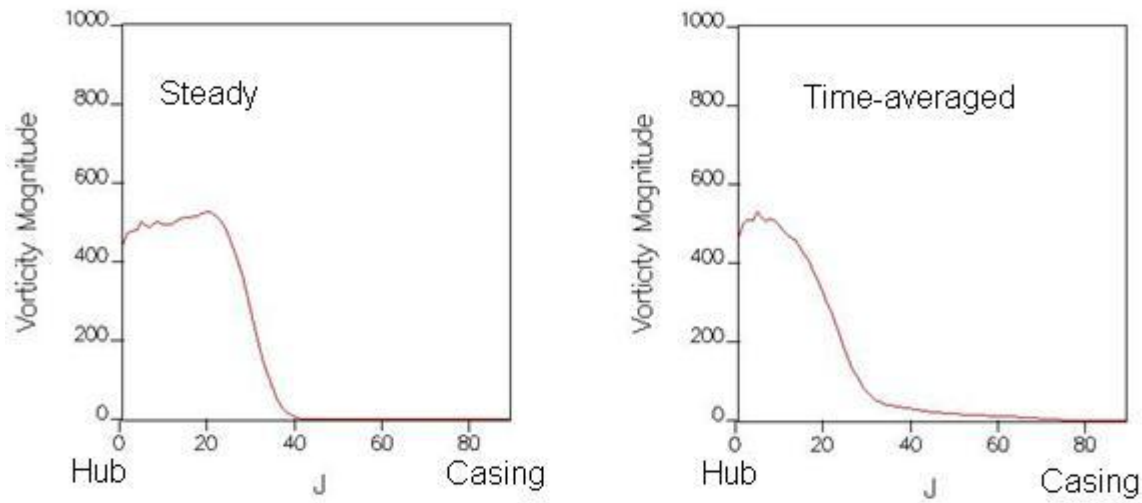

Figure 5.32 Boundary layer shape characterized by vorticity magnitude

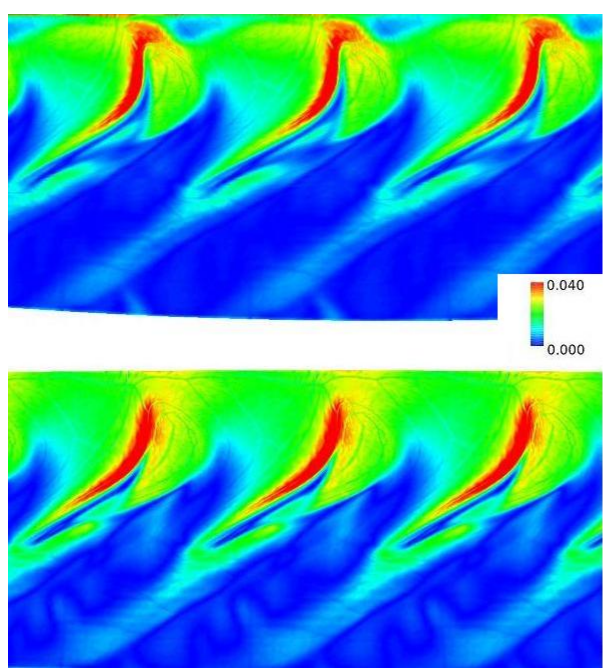

Figure 5.33 Stanton number on rotor casing for steady (top) and time-average (bottom) of unsteady simulations

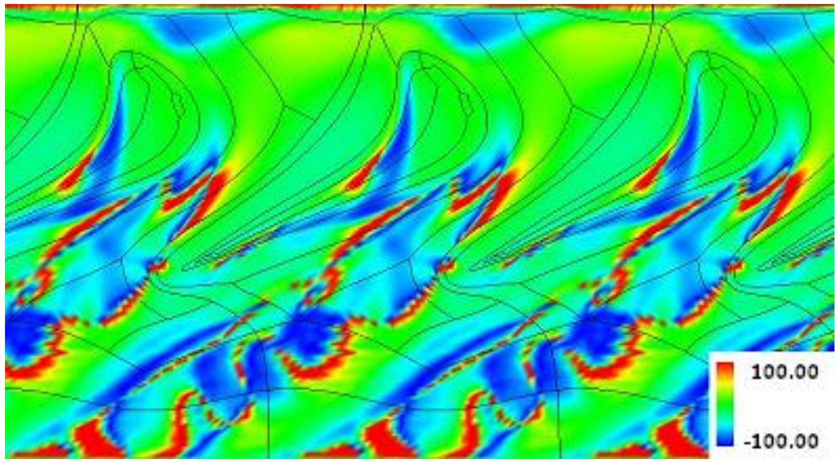

Figure 5.34 Percent difference between steady and time-averaged Stanton number on rotor casing

The heat flux distribution on the casing (figure 5.33) is similar to the work of Ameri et al. [54] who observe that the heat flux directly above the rotor tip gap entrance is much higher than elsewhere in the domain because of work transfer involved in the interaction of two frames in relative motion [55] [56]. Minimal effects of unsteadiness were observed on the hub and casing surfaces and this is in agreement with Ameri et al. [54]. In a simulation involving adiabatic walls, it is conceivable that the adiabatic wall temperature in some regions of the flow may rise above the stagnation temperature at the inlet to the stage. This is due to the fact that the rotation of the blade adds a rotational velocity component to the flow. This additional velocity manifests as an increased shear near the casing because the casing experiences flow in the absolute frame. The fluid near the casing thus experiences an increased enthalpy and thereby higher stagnation temperature than the stage inlet. This is true for both steady and unsteady simulations where two or more relative frames of motion are involved. Based on this analysis, one would expect a rise in stagnation temperature upstream of the leading edge as well. This region experiences large absolute velocity but the relative velocity is minimal. The shear work due to the rotation is thus converted to enthalpy of the fluid. The shear work and the enthalpy adjust to satisfy the energy equation because the pressure ratio across a stream tube that undergoes varying shear may remain constant in a relative frame of reference. The above discussion is borne out by the following thought experiment. Consider two stream tubes. The first stream tube is located near the casing at the tip gap entrance on the pressure side of the rotor and is oriented in the streamwise direction. The second stream tube is located near the tip surface. Assume that the thermal profile at the rotor blade row inlet is uniform with a stagnation temperature of unity. The energy equation requires that the internal energy convected into the stream tube be equal to the sum of the heat flux added to the tube, the pressure work done on the tube and work due to body forces and shear stresses. Assuming that the walls are adiabatic, it is clear to see that there is no effect of heat flux on the internal energy of the tubes. There are no body forces at work either. Assume that the pressure ratio across both tubes is comparable as are the absolute velocities. This means that the only difference in the internal energies of the two stream tubes is due to the shear work on them. Shear is related to velocity gradient and in the absolute frame of reference, the shear work on the fluid by the casing is approximately 6 times higher than the shear work on the fluid by the tip (or any surface rotating with the blade.) The Reynolds number in the relative frame is lower than in the absolute frame and this leads to a relatively thicker boundary layer. Coupled with a smaller velocity gradient across the boundary layer, this leads to the shear stress at the tip surface (second stream tube) being considerably smaller than at the casing. This is the reason why the stagnation temperature at the casing exceeds that at the tip. For the work presented in this dissertation (isothermal walls), the added work to the fluid manifests as large Stanton numbers on the casing at the tip gap entrance. This is evident from figure 5.33. The average Stanton number at the tip gap entrance on the casing is 0.4. This is twice as high as the largest Stanton number found on the blade surface. The above discussion assumed that the flow in the tip gap is subsonic in the relative frame (to avoid effects of shock-boundary layer interaction.) For the current study this is true in the leading edge to quarter chord region of the tip gap, above which the highest Stanton number on the casing is observed. In addition, the entropy at the tip entrance is fairly constant leading to an increase in stagnation pressure. This is accompanied by a rapid acceleration of flow across the tip gap.

Another way to understand this work transfer is to realize that the pressure ratio across the stage is analogous to a potential energy. It has the potential to do work on the rotor blade. When the pressure drives flow through the rotor passage, the geometry of the blade is able to harness the pressure to rotate the blade. At the tip, some of this work done on the blade is transferred to the tip leakage flow (the relative velocity in the tip gap is increased due to leakage.) The increased flow velocity creates higher shear stress on the casing. The effect would predominantly be observed at the tip gap entrance where the expansion into the tip gap peaks. In the event of a low stage loading the relative velocity in the tip gap is quite small compared to the rotational speed of the blade. This would cause lower values of shear stress on the casing and therefore lower heat flux. In summary, the work done by the flow on the blade is converted to kinetic energy of the blade. Some of the kinetic energy of the blade is transferred to the flow in the tip gap. This kinetic energy in the tip gap causes the shear work on the casing to increase (work is done on the casing by the flow.) This work results in an increase in internal energy because the pressure ratio across the tip can be assumed fairly uniform in the radial direction. The casing is fixed and therefore the work cannot be converted to kinetic energy. The only other avenue is for the work to manifest as a rise in thermal energy (enthalpy.) In general, any region of flow that has a significant relative velocity component in the tangential direction (direction of rotation) is likely to experience an increase in stagnation enthalpy. In the present study, a 5% increase in stagnation temperature upstream of the rotor was observed while the stagnation temperature at the entrance to the tip gap rose by as much as 11% over the stage inlet stagnation temperature. Table 5.2 shows the adiabatic wall temperature that could be expected on the leading edge of the blade as a function of recovery factor [8]. Table 5.3 shows the adiabatic wall temperature that could be expected on the casing, near the tip gap entrance of the blade as a function of recovery factor [8].

Table 5.2 Estimate of adiabatic wall temperature at rotor leading edge

Recovery	Leading edge			
Factor	T_0	M	T	T_{aw}
0.9	1.05	1.58	0.7	1.02
0.89	1.05	1.58	0.7	1.01
0.88	1.05	1.58	0.7	1.01
0.87	1.05	1.58	0.7	1
0.86	1.05	1.58	0.7	1
0.85	1.05	1.58	0.7	1
0.84	1.05	1.58	0.7	0.99
0.83	1.05	1.58	0.7	0.99

Table 5.3 Estimate of maximum casing adiabatic wall temperature

Recovery	Tip gap entrance			
Factor	T_0	M	T	T_{aw}
0.9	1.11	1.94	0.63	1.06
0.89	1.11	1.94	0.63	1.06
0.88	1.11	1.94	0.63	1.05
0.87	1.11	1.94	0.63	1.05
0.86	1.11	1.94	0.63	1.04
0.85	1.11	1.94	0.63	1.04
0.84	1.11	1.94	0.63	1.03
0.83	1.11	1.94	0.63	1.03

The adiabatic temperature is computed as [8],

$$T_{aw} = T \cdot (1 + \Re \cdot \frac{\gamma - 1}{2} \cdot M^2)$$

Here, $\Re$, is the recovery factor and the temperature, T, and absolute Mach number, M, are at locations in the free stream at which the stagnation temperature, T_0, is listed in tables 5.2 and 5.3. It is clear that at the leading edge, the effect of work transfer is not as evident. At the tip gap entrance, even assuming very low thermal recovery through the boundary layer, the adiabatic wall temperature is at least 3% higher than the inlet total temperature. At the leading edge this argument is not very accurate because the recovery factors are based on a one dimensional model. In the tip gap, however, the high speed flow lends itself to quasi one dimensional analysis. The predicted values of adiabatic wall temperature are in line with the simulations of Ameri et al. [54].

Chapter 6: Conclusions and Future Work

6.2 Conclusions

- A preprocessor was successfully developed and tested that acts as a conduit between the grid generation package GridProTM and TURBO.
- Wilcox's k-ω turbulence model [39] was successfully incorporated into TURBO and validated for the case of flow of a flat plate.
- Two turbulence models, the low Reynolds number k-ε model of Shih [24] and Wilcox's k-ω model [39] were compared by testing their ability to predict the film cooling effectiveness downstream of a cooling hole that jets into flow over a flat plate. The models were also used to predict heat flux at the mid-span of a high pressure turbine vane. The results from both tests were compared to experiment. It was found that the k-ε model is more suited to model heat flux.
- Unsteady stator-rotor interaction was studied by simulating flow and heat flux through a highly loaded transonic turbine stage. The results were compared to those from a steady simulation as well as to experiment.

- The effect of unsteadiness is most prominent at the leading edge of the blade and at the mid-span section of the rotor.
- Tangential redistribution of the thermal wake was observed in the leading edge region of the rotor. However, due to the presence of strong shocks in the region, the wake's influence is not thought to propagate downstream. In addition, because of the manner in which the heat flux was normalized to obtain Stanton number, it is uncertain how much of redistribution is caused due to differing thermal wake profiles and how much is simply due to the change in frequency of wake passage.
- A high degree of unsteadiness was also observed over a small region of the aft section of the rotor tip surface. This is due to radial unsteadiness that is a result of the highly three dimensional geometry. The unsteadiness manifests as a strengthening and weakening structure of oblique shocks and their reflections.
- A 'hot spot' was identified on the tip where the heat flux is comparable to the leading edge region. This spot is associated with the unsteady shock structure that was observed in the tip gap.
- The aft 70% of the tip gap is choked by the formation of a throat at the tip gap entrance. It is thought that this could be used to redesign the tip to push the choke point towards the tip gap exit near the suction side and thus attenuate the heating effect of the oblique shocks. In this case a prolonged separation zone would also be beneficial in the tip gap.

- The rotor surface pressure and heat flux predicted by the time-average of unsteady simulation match very well with experiment.
- On the tip and hub, the agreement with experiment was excellent in the aft region of the rotor blade. It is thought that the flow conditions during the experiment might have been laminar in the leading edge region of the rotor passage leading to lower heat flux values from experiment compared to the time-averaged simulation (fully turbulent).
- The hub and casing heat flux were found to be fairly insensitive to unsteadiness and this is in agreement with established literature.
- A complete three dimensional view of the flow through the rotor passage was realized showing the shock structures between the vane and the rotor as well as in the rotor passage.

6.3 Future work

While the analyses presented in this dissertation provided several useful insights into unsteady rotor physics, several questions remain unanswered. Specifically, it would be prudent to conduct a simulation with adiabatic wall boundary conditions in order to normalize heat flux with adiabatic wall temperature. This would show the true extent of the differences between the steady and unsteady simulation by comparing heat flux normalized by adiabatic wall temperature. Such a simulation is currently in progress. In addition, laminar solutions could show whether the flow in the leading edge region is laminar by comparing heat flux in this region to experiment. As has been suggested in this dissertation, tip geometry to choke the tip flow at the tip exit could prove beneficial in minimizing the tip surface heat flux for highly loaded turbine stages. It would be interesting to see whether this theory is borne out by performing a numerical simulation. To simplify the process of porting grid geometry from the grid generator to TURBO a graphical user interface for the preprocessor would be beneficial.

REFERENCES

[1] Cumpsty, N., "Jet Propulsion", Cambridge University Press, 2003.

[2] Hill, P., and Peterson, C., "Mechanics and Thermodynamics of Propulsion", Addison Wesley Publishing Company, 1992.

[3] Lewis, M.J., Quotation from Speech at Fundamental Aeronautics Program Annual Meeting 2009, October 2009.

[4] Mattingly, J.D., Heiser, W.H., and Pratt, D.T., "Aircraft Engine Design", Second Edition, AIAA Education Series, 2002.

[5] Young, A.D., "Boundary Layers", AIAA Education Series, 1989.

[6] Wilcox, D.C., "Turbulence Modeling for CFD", Second Edition, DCW Industries, March 2000.

[7] Pope, S.B., "Turbulent Flows", Cambridge University Press, 2005.

[8] Shapiro, A.H., "The Dynamics and Thermodynamics of Compressible Fluid Flows", The Ronald Press Company, 1954.

[9] Anderson, J.D., "Hypersonic and High Temperature Gas Dynamics", McGraw-Hill, Inc., 1989.

[10] Hodson, P. and Dawes, N., “On the Interpretation of Measured Profile Losses in Unsteady Wake-Turbine Blade Interaction studies,” ASME-96-GT-494, February 1996.

[11] Denos, R., Arts, T., Paniagua, G., Michelassi, V., and Martelli, F., “Investigation of the Unsteady Rotor Aerodynamics in a Transonic Turbine Stage,” ASME-2000-GT-435, January 2001.

[12] Giles, M.B., “Stator/Rotor Interaction in a Transonic Turbine Stage,” AIAA Paper no. 88-3093, 1988.

[13] Shang, T., and Epstein, A.H., “Analysis of Hot Streak Effects on Turbine Rotor Heat Load,” Journal of Turbomachinery, Vol. 119, pp 544-553, July 1997.

[14] Ameri, A.A., Rigby ,D.L., Steinthorsson, E., Heidmann, J., and Fabian, J.C., “Unsteady Analysis of Blade and Tip Heat Transfer as Influenced by the Upstream Momentum and Thermal Wakes,” ASME-GT2008-51242, June 2007.

[15] Kerrebrock, J.L., and Mikolajczak, A.A., “Intra-Stator Transport of Rotor Wakes and Its Effect on Compressor Performance,” Journal of Engineering for Power, Vol. 92, No. 4, October 1970, pp. 359-368.

[16] Bell, D.L., and He, L., “Three-Dimensional Unsteady Flow for an Oscillating Turbine Blade and the Influence of Tip Leakage,” ASME-98-GT-571, February 1998.

[17] Urbassik, R.M., Wolff, J.M., and Polanka, M.D., “Unsteady Aerodynamics and Interactions Between a High Pressure Turbine Vane and Rotor,” ASME-GT2004-53607, June 2004.

[18] Tallman, J.A., Haldeman, C.W., Dunn ,M.G., Tolpadi, A.K., and Bergholz, R.F., “Heat Transfer Measurements and Predictions for a Modern, High-Pressure, Transonic Turbine, Including Endwalls,” ASME-GT2006-90927, May 2006.

[19] Luk, D.F., “Steady Heat Transfer predictions for a Highly Loaded Single Stage Turbine with a Flat Tip,” Master’s Thesis, The Ohio State University, Columbus, Ohio, October 2008.

[20] Holmes, D.G., Mitchell, B.E., and Lorence, C.B., Three Dimensional Linearized Navier-Stokes Calculations for Flutter and Forced Response,” 8th International Symposium on Unsteady Aerodynamics and Aeroelasticity of Turbomachines, September 1997.

[21] Chen, J.P., and Whitfield, D.L., "Navier-Stokes Calculations for the Unsteady Flowfield of Turbomachinery," AIAA-93-0676, January 1993.

[22] Chen, J.P., and Barter, J., "Comparison of Time-Accurate Calculations for the Unsteady Interaction in Turbomachinery Stage," AIAA-98-3292, July 1998.

[23] Chen, J.P., and Briley, W.R., "A Parallel Flow Solver for Unsteady Multiple Blade Row Turbomachinery Simulations," ASME-2001-GT-0348. June 2001.

[24] Zhu, J., Shih, T.H., “A Turbulence Module for the NPARC Code,” NASA CR-198358, July 1995.

[25] Van Zante, D., Chen, J., Hathaway, M., and Chriss, R., “The Influence of Compressor Blade Row Interaction Modeling on Performance Estimates from Time-Accurate, Multistage, Navier-Stokes Simulations,” ASME-GT2005-68463, August 2006.

[26] Gerolymos, G.A., Michon, G.J., and Neubauer, J., “Analysis and Application of Chorochronic Periodicity in Turbomachinery Rotor/Stator Interaction Computations,” Journal of Propulsion and Power, Vol. 18, No. 6, November-December, 2002.

[27] Bunker, R.S., "A Review of Turbine Blade Tip Heat Transfer", Annals of the New York Academy of Science, Vol. 934, pp 64-79, January 2006.

[28] Ameri, A.A., "Turbine Blade Tip Design and Tip Clearance Treatment", Notes from von Karman Lecture Series 2004, June 2004.

[29] Zhou, C., and Hodson, H., "The Tip Leakage flow of an Unshrouded High Pressure Turbine Blade with Tip Cooling", ASME-GT2009-59637, June 2009.

[30] Ameri, A.A., Steinthorsson, E., Rigby, D.L., "Effect of Squealer Tip on Rotor Heat Transfer and Efficiency", Journal of Turbomachinery, Vol. 120, pp 753-759, October 1998.

[31] Ameri, A.A., Steinthorsson, E., Rigby, D.L., "Effects of Tip Clearance and Casing Recess on Heat Transfer and Stage Efficiency in Axial Turbines", Journal of Turbomachinery, Vol. 121, pp 683-693, October 1999.

[32] O'Dowd, D., Zhang, Q., Ligrani, P., He, L., Friedrichs, S., "Comparison of Heat Transfer Measurement Techniques on a Transonic Turbine Blade Tip", ASME-GT2009-59376, June 2009.

[33] Hofer, T., Arts, T., "Aerodynamic Investigation of the Tip Leakage Flow for Blades with Different Tip Squealer Geometries at Transonic Conditions", ASME-GT2009-59909, June 2009.

[34] Krishnababu, S.K., Dawes, W.N., Hodson, H.P., Lock, G.D., Hannis, J., Whitney, C., "Aero-Thermal Investigations of Tip Leakage Flow in Axial Flow Turbines, Part II -Effect of Relative Casing Motion", ASME 2007-GT-27957, May 2007.

[35] Wheeler, A.P.S., Atkins, R., He, L., "Turbine Blade Tip Heat Transfer in Low and High Speed Flows", ASME-GT2009-59404, June 2009.

[36] Abhari, R.S., Guenette, R.G., Epstein, A.H., and Giles, M.B., “Comparison of Time-Resolved Turbine Rotor Blade Heat Transfer Measurements and Numerical Calculations,” ASME-91-GT-268. March 1991.

[37] Herrick, G.P., “Facilitating Higher Fidelity Simulations of Axial Compressor Instability and Other Turbomachinery Flow Conditions,” PhD Thesis, Mississippi State University, May 2008.

[38] Roe, P.L., "Approximate Riemann Solvers, Parameter Vectors, and Difference Schemes", Journal of Computational Physics, vol. 43, pp 357-372, March 1981.

[39] Garg, V.K., Ameri, A., “Comparison of two-equation turbulence models for prediction of heat transfer on film cooled turbine blades”, AYT Corporation, Cleveland OH, 1997.

[40] Whitfield, D.L, Janus, J.M., "Three-Dimensional Unsteady Euler Equations Solution Using Flux Vector Splitting", Department of Aerospace Engineering, Mississippi State University, 1984.

[41] Chen, J.P., "Unsteady Three-Dimensional Thin-Layer Navier-Stokes Solutions For Turbomachinery In Transonic Flow", PhD Dissertation, Mississippi State, Mississippi, December 1991.

[42] http://www.gridpro.com/, Program Development Company, White Plains NY, 10601, USA.

[43] http://www.simcenter.msstate.edu/simcenter/docs/msu_turbo/, MSUTURBO Online Documentation, Engineering Research Center, MI 39762.

[44] Sinha, A.K., Bogard, D.G., and Crawford, M.E., “Film-Cooling Effectiveness Downstream of a Single Row of Holes with Variable Density Ratio,” Journal of Turbomachinery, Vol. 113, pp. 442-449, 1991.

[45] "Film Cooling Science and Technology for Gas Turbines", Book Edited by Bunker, R.S., and Arts, T., von Karman Institute for Fluid Dynamics, April 2007.

[46] Peterson, S.D. and Plesniak, M.W., "Evolution of Jets Emanating from Short Holes into Crossflow," Journal of Fluid Mechanics, Vol. 503, pp. 57-91, 2004.

[47] Bons, J.P., MacArthur, C.D., Rivir, R.B., "The Effect of High Freestream Turbulence on Film Cooling Effectiveness", ASME 94-GT-51, 1994.

[48] Lemmon, C.A., Kohli, A. and Thole, K.A., "Formation of Counter-Rotating Vortices in Film Cooling Flows", Pratt & Whitney, 400 Main Street, MS 169-02, East Hartford, CT 06108.

[49] El-Gabry, L., Heidmann, J. and Ameri, A., "Numerical Analysis of Film Cooling at High Blowing Ratio", NASA TM-2009-215517, April 2009.

[50] Thole, K.A., Sinha, A.K., Bogard, D.G., and Crawford, M.E., “Mean Temperature Measurements of Jets in Crossflow for Gas Turbine Film Cooling Applications,” Third International Symposium on Transport Phenomena and Dynamics of Rotating Machinery, 1990.

[51] Green, B.R., Barter, J.W., Haldeman, C.W., and Dunn, M.G., “Averaged and Time-Dependent Aerodynamics of a High Pressure Turbine Blade Tip Cavity and Stationary Shroud: Comparison of Computational and Experimental Results," ASME-2004-GT-53443, October 2005.

[52] De la Loma A., Paniagua G., Verrastro D., Adami P., 2007, “Transonic Turbine Stage Heat Transfer Investigation in Presence of Strong Shocks”. Proceedings of the ASME Turbo Expo 2007. ASME-GT2007-27101, May 2007.

[53] Sabatino, D.R., Smith, C.R., "Boundary Layer Influence on the Unsteady Horseshoe Vortex Flow and Surface Heat Transfer", ASME-GT2007-27633, May 2007.

[54] Ameri, A.A., and El-Gabry, L.A., " Comparison of Steady and Unsteady Heat Transfer Simulations of Hub and Endwall of a Turbine Blade Passage", 2009 ASME Heat Transfer Conference, July 2009.

[55] Thorpe, S.J., and Ainsworth, R., " The Effects of Blade Passing on the Heat Transfer Coefficient of the Over-tip Casing in a Transonic Turbine Stage,” Proc. 2006 ASME Turbo Expo, Paper GT2006-90534, May 2006.

[56] Thorpe, S.J., Miller, R.J., Yoshino, S., Ainsworth, R.W., and Harvey, N.W., “The Effect of Work Processes on the Casing Heat Transfer of a Transonic Turbine,” ASME Turbo Expo, Paper GT2005-68437, 2005.

[57] Nyhoff, L.R., Leestma, S.C., "Fortran 90 for Engineers and Scientists", Prentice Hall, Inc., 1997.

Appendix A: Governing equations

The figures in this appendix show equations and variables scanned from [41] that form the basis for TURBO. Nomenclature and descriptions of the variables in the figures are found in [41]. Figure A.1 shows the governing equations of fluid motion as presented in [41]. Figure A.2 shows the governing equations in vector form. This is the form that is transformed into computational space for incorporation into TURBO.

mass conservation
$$\frac{\partial \hat{\varrho}}{\partial \hat{t}} + \nabla \cdot (\hat{\varrho}\underline{\hat{v}}) = 0, \qquad (2\,.\,1)$$

momentum conservation
$$\frac{\partial}{\partial \hat{t}}(\hat{\varrho}\ \underline{\hat{v}}) + \nabla \cdot (\hat{\varrho}\ \underline{v}\ \underline{\hat{v}}) = \nabla \cdot (\tilde{\pi}), \qquad (2\,.\,2)$$

energy conservation
$$\frac{\partial \hat{e}}{\partial \hat{t}} + \nabla \cdot (\hat{e}\ \underline{\hat{v}}\ \underline{\hat{v}}) = -\nabla \cdot \underline{\hat{q}} + \nabla \cdot (\tilde{\pi} \cdot \underline{\hat{v}}), \qquad (2\,.\,3)$$

where $\tilde{\pi} = -\hat{p}\ \tilde{I} + \bar{\tau}$ is the stress tensor.

$\hat{p}$ is the thermodynamic static pressure.

$\bar{\tau} = \hat{\lambda}\ (div\ \underline{\tilde{v}})\ \tilde{I} + \hat{\mu}\ [(grad\ \underline{\hat{v}}) + (grad\ \underline{\hat{v}})^T]$ is the deviatoric term of $\tilde{\pi}$, which contains viscous shear stress.

$\hat{\lambda}$ and $\hat{\mu}$ are coefficients of viscosity.

$\hat{e} = \hat{\varrho}\ (\hat{e}_i + \frac{|\underline{\hat{v}}|^2}{2})$ is the total energy per unit volume.

$\hat{e}_i$ is the internal energy.

$\underline{\hat{q}}$ is the heat flux vector.

Continued...

Figure A.1 Equations governing fluid motion [41]

Figure A.1 continued

mass conservation

$$\frac{\partial\hat{\varrho}}{\partial\hat{t}} + \frac{\partial}{\partial\hat{x}}(\hat{\varrho}\hat{u}) + \frac{\partial}{\partial\hat{y}}(\hat{\varrho}\hat{v}) + \frac{\partial}{\partial\hat{z}}(\hat{\varrho}\hat{w}) = 0, \tag{2.4}$$

momentum conservation

$$\frac{\partial}{\partial\hat{t}}(\hat{\varrho}\hat{u}) + \frac{\partial}{\partial\hat{x}}(\hat{\varrho}\hat{u}^2 + \hat{p} - \hat{\tau}_{xx}) + \frac{\partial}{\partial\hat{y}}(\hat{\varrho}\hat{u}\hat{v} - \hat{\tau}_{xy}) + \frac{\partial}{\partial\hat{z}}(\hat{\varrho}\hat{u}\hat{w} - \hat{\tau}_{xz}) = 0, \tag{2.5}$$

$$\frac{\partial}{\partial\hat{t}}(\hat{\varrho}\hat{v}) + \frac{\partial}{\partial\hat{x}}(\hat{\varrho}\hat{u}\hat{v} - \hat{\tau}_{xy}) + \frac{\partial}{\partial\hat{y}}(\hat{\varrho}\hat{v}^2 + \hat{p} - \hat{\tau}_{yy}) + \frac{\partial}{\partial\hat{z}}(\hat{\varrho}\hat{v}\hat{w} - \hat{\tau}_{yz}) = 0, \tag{2.6}$$

$$\frac{\partial}{\partial\hat{t}}(\hat{\varrho}\hat{w}) + \frac{\partial}{\partial\hat{x}}(\hat{\varrho}\hat{u}\hat{w} - \hat{\tau}_{xz}) + \frac{\partial}{\partial\hat{y}}(\hat{\varrho}\hat{v}\hat{w} - \hat{\tau}_{yz}) + \frac{\partial}{\partial\hat{z}}(\hat{\varrho}\hat{w}^2 + \hat{p} - \hat{\tau}_{zz}) = 0. \tag{2.7}$$

energy conservation

$$\begin{aligned} &\frac{\partial\hat{e}}{\partial\hat{t}} + \frac{\partial}{\partial\hat{x}}[(\hat{e} + \hat{p})\hat{u} - \hat{u}\hat{\tau}_{xx} - \hat{v}\hat{\tau}_{xy} - \hat{w}\hat{\tau}_{xz} + \hat{q}_x] \\ &\quad + \frac{\partial}{\partial\hat{y}}[(\hat{e} + \hat{p})\hat{v} - \hat{u}\hat{\tau}_{xy} - \hat{v}\hat{\tau}_{yy} - \hat{w}\hat{\tau}_{yz} + \hat{q}_y] \\ &\quad + \frac{\partial}{\partial\hat{z}}[(\hat{e} + \hat{p})\hat{w} - \hat{u}\hat{\tau}_{xz} - \hat{v}\hat{\tau}_{yz} - \hat{w}\hat{\tau}_{zz} + \hat{q}_z] = 0. \end{aligned} \tag{2.8}$$

$$\frac{\partial \hat{q}}{\partial \hat{t}} + \frac{\partial \hat{f}}{\partial \hat{x}} + \frac{\partial \hat{g}}{\partial \hat{y}} + \frac{\partial \hat{h}}{\partial \hat{z}} = 0, \tag{2.19}$$

$$\hat{q} = \begin{bmatrix} \hat{\varrho} \\ \hat{\varrho}\hat{u} \\ \hat{\varrho}\hat{v} \\ \hat{\varrho}\hat{w} \\ \hat{e} \end{bmatrix} \tag{2.20}$$

$$\hat{f} = \begin{bmatrix} \hat{\varrho}\hat{u} \\ \hat{\varrho}\hat{u}^2 + \hat{p} - \hat{\tau}_{xx} \\ \hat{\varrho}\hat{u}\hat{v} - \hat{\tau}_{xy} \\ \hat{\varrho}\hat{u}\hat{w} - \hat{\tau}_{xz} \\ (\hat{e} + \hat{p})\hat{u} - \hat{u}\hat{\tau}_{xx} - \hat{v}\hat{\tau}_{xy} - \hat{w}\hat{\tau}_{xz} + \hat{q}_x \end{bmatrix} \tag{2.21}$$

$$\hat{g} = \begin{bmatrix} \hat{\varrho}\hat{v} \\ \hat{\varrho}\hat{u}\hat{v} - \hat{\tau}_{xy} \\ \hat{\varrho}\hat{v}^2 + \hat{p} - \hat{\tau}_{yy} \\ \hat{\varrho}\hat{v}\hat{w} - \hat{\tau}_{yz} \\ (\hat{e} + \hat{p})\hat{v} - \hat{u}\hat{\tau}_{xy} - \hat{v}\hat{\tau}_{yy} - \hat{w}\hat{\tau}_{yz} + \hat{q}_y \end{bmatrix} \tag{2.22}$$

Continued...

Figure A.2 Governing equations in vector form [41]

Figure A.2 continued

$$\hat{h} = \begin{bmatrix} \hat{\varrho}\hat{w} \\ \hat{\varrho}\hat{u}\hat{w} - \hat{\tau}_{xz} \\ \hat{\varrho}\hat{v}\hat{w} - \hat{\tau}_{yz} \\ \hat{\varrho}\hat{w}^2 + \hat{p} - \hat{\tau}_{zz} \\ (\hat{e} + \hat{p})\hat{w} - \hat{u}\hat{\tau}_{xz} - \hat{v}\hat{\tau}_{yz} - \hat{w}\hat{\tau}_{zz} + \hat{q}_z \end{bmatrix} \qquad (2.23)$$

$$x = \frac{\hat{x}}{\hat{R}}, \quad y = \frac{\hat{y}}{\hat{R}}, \quad z = \frac{\hat{z}}{\hat{R}}, \quad u = \frac{\hat{u}}{\hat{a}_o}, \quad v = \frac{\hat{v}}{\hat{a}_o}, \quad w = \frac{\hat{w}}{\hat{a}_o},$$

$$p = \frac{\hat{p}}{\hat{\varrho}_o \hat{a}_o^2}, \quad \varrho = \frac{\hat{\varrho}}{\hat{\varrho}_o}, \quad t = \frac{\hat{a}_o \hat{t}}{\hat{R}}, \quad e = \frac{\hat{e}}{\hat{\varrho}_o \hat{a}_o^2}, \quad \mu = \frac{\hat{\mu}}{\hat{\mu}_o}, \quad h = \frac{\hat{h}}{\hat{a}_o^2},$$

$$\tau_{ij} = \frac{\hat{\tau}_{ij}}{\hat{\varrho}_o \hat{a}_o^2}, \quad \tau_{wall} = \frac{\hat{\tau}_{wall}}{\left(\frac{\hat{\mu}_o \hat{a}_o}{\hat{R}}\right)}, \quad q_{x_i} = \frac{\hat{q}_{x_i}}{\hat{\varrho}_o \hat{a}_o^3}, \quad T = \frac{\hat{T}}{\hat{T}_o}.$$

Figure A.3 Nondimensional variables [41]

Figure A.3 shows the manner in which physical quantities are non-dimensionalized in TURBO using reference variables.

Appendix B: Preprocessor

B.1 Usage

This section defines the manner in which one may utilize a grid generated by GridProTM for the purpose of simulating a flow using TURBO. Once a grid is generated in GridProTM using a suitable topology [42] and by assigning the desired boundary conditions to the geometric surfaces, a file with the extension '.conn' is generated that is associated with the grid. This file contains the connectivity information required to link the blocks together. For the purposes of illustration, assume that the grid file is named 'grid.tmp' and the '.conn' file is named 'grid.tmp.conn'. Using the GridProTM command *mrgb* (see [42]) the '.conn' file is used to create a file with extension '.conn_n'. This file contains both the connectivity and boundary conditions required to completely define the computational domain. For example, typing the command 'mrgb grid.tmp -maxb 1' in a terminal will produce the file 'grid.tmp.tmp.conn_n' and a grid file 'grid.tmp.tmp' that is identical to grid.tmp. The parameter '-maxb' determines how many blocks of the original grid, 'grid.tmp', are to be merged to form the new grid, 'grid.tmp.tmp'. In the above example no merging takes place. The preprocessor uses the merged grid and '.conn_n' file along with input files to generate 'GU' files (grid files formatted for use with TURBO), 'input00', 'bc.in', 'dmap.in' and 'turbo.in' (these files are required as input for TURBO).

For details regarding these files and their formats refer to [43]. First, the GridProTM grid is converted to plot3d format. In this format it is easier to verify connectivity information and the grid can also be viewed in postprocessors such as FIELDVIEW. Once the connectivity information is verified, the plot3d file is converted to GU files (one GU file for every block.) The 'conn_n' file is used to create the TURBO boundary condition file, 'bc.in' and connectivity file, 'dmap.in'. The preprocessor can operate on multiple blade rows and is therefore capable of processing grids for unsteady simulations. If the simulation involves multiple blade rows, a 'turbo.in' file is generated that contains information on the sliding interface locations. In order to conform to the boundary condition specifications listed in section 1.5 the preprocessor checks blocks for the orientation of their computational coordinates and reorients them to satisfy the specifications. If it is unable to determine the correct block orientation a list of such blocks is printed out so that the user may manually inspect the blocks. If a manual inspection is required a separate utility called 'reorient.f' may be utilized to reorient the blocks in question. The reorienting operations are accompanied by suitable modifications to the boundary condition and connectivity files. In the event that a user would wish to run multiple blocks on a single processor, various schedule files are generated. These contain various groupings of blocks to allow the user to determine the most efficient way to run the simulation. Figure B.1 shows a flowchart of the process at a high level.

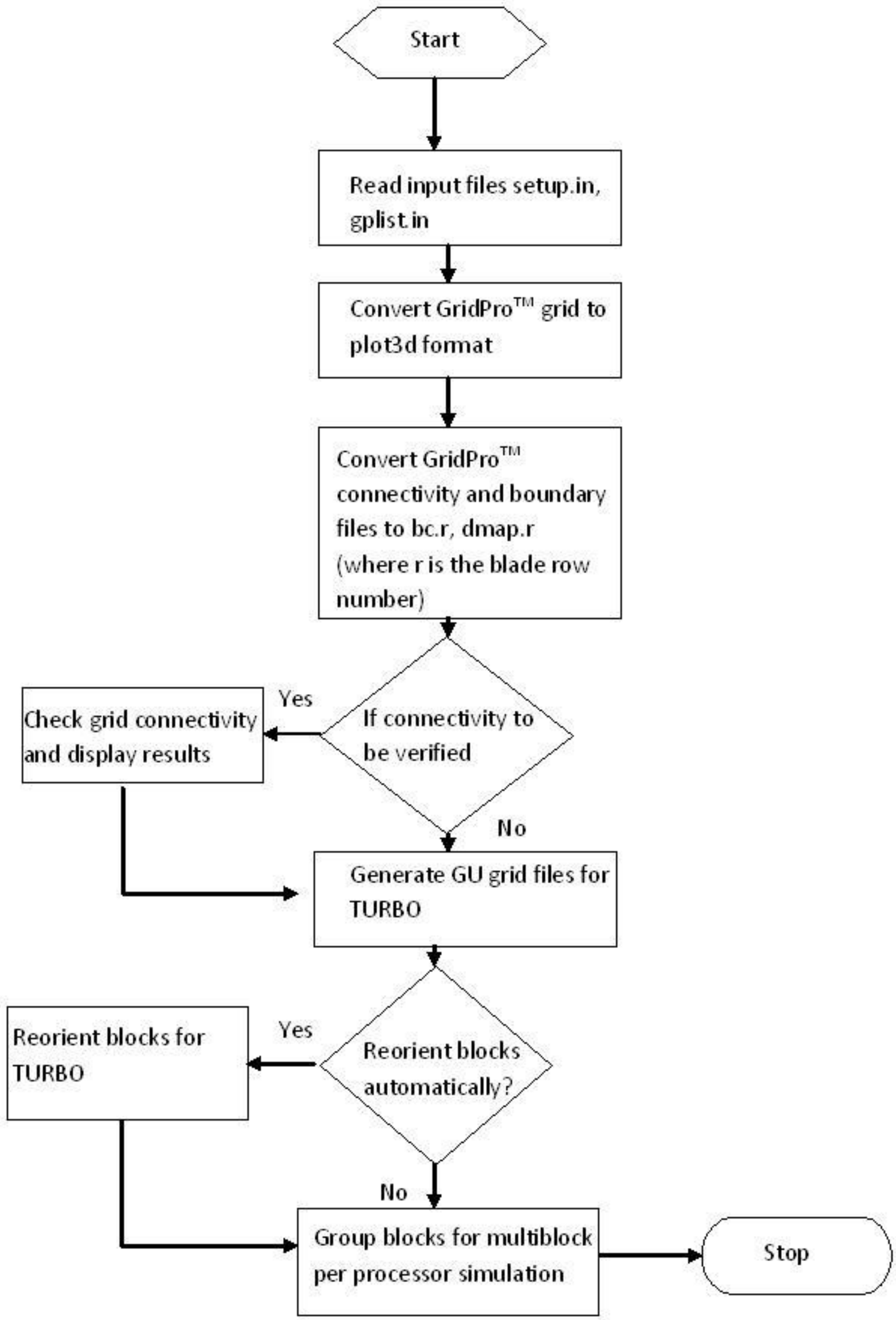

Figure B.1 Flowchart of major processes in preprocessor

B.2 Method for reorienting blocks

In order to determine whether a block requires reorientation the preprocessor cycles through the boundary conditions file and creates an array containing the block numbers of blocks that have one or more boundary condition. If a block contains an inlet boundary condition, the preprocessor attempts to determine the axial direction and reorients the block such that the inlet is on an imin face. It accomplishes this by searching for the direction of increasing *x*-coordinate. A similar procedure is used for a block containing an exit. The block containing an exit boundary condition is reoriented so that the exit lies on an i_{max} face. Next, the preprocessor looks for periodic faces and assigns faces with a 'ref_periodic_fwd' (see [43]) boundary condition to a k_{max} face and faces with a ref_periodic_bak boundary condition to a k_{min} face. Blocks that have already been operated on to align inlets and exits are manipulated in a way that ensures the inlet and exit faces are not changed. The preprocessor then attempts to determine the radial direction within every block in the grid that contains at least one no slip boundary condition and that has not been operated on before. If it is found that the extremities of a particular computational coordinate correspond to the minimum and maximum average radii within a block, the block is reoriented so that the face with the minimum radius is a j_{min} face and the face with the maximum average radius is a j_{max} face.

Once the GU files for a multiple blade row case are obtained it might be necessary to match the radial lines at the interface of the multiple rows. These are both sliding interfaces. According to TURBO specifications the radial lines at this interface must match. A simple interpolation may be performed across the interface to match the line in the radial direction (see [19])

B.3 Input files

In order to use the preprocessor, two input files are required. The first is named 'setup.in'. It contains a list of parameters that specify the input grid files for each blade row (row_names), the number of blades per blade row (num_blades), whether connectivity information should be verified (checkconn), tolerance to use for connectivity verification (conn_tol) and whether or not the preprocessor should attempt to reorient the blocks to satisfy TURBO specifications (turbo_friendly). The following table lists the variables and their possible values and formats that are specified in the namelist ([57]) of 'setup.in'.

Table B.1 Contents of preprocessor input file setup.in

Namelist	**SETUP_PARAMS**
variable names	Allowable values
num_blade_rows	Integer value indicating number of blade rows to be processed
num_blades	Integer array of blade counts for each blade row (int1 int2 ... or int1, int2, ...)
checkconn	0 or 1 (no connectivity checking or connectivity checking)
conn_tol	Real number indicating tolerance to use while checking connectivity
turbo_friendly	.TRUE. Or .FALSE. (reorient blocks to meet TURBO criteria or not)
row_names	List of grid file names for each blade row (grd1.tmp grd2.tmp ...)
	Assumes that corresponding connectivit files are named grd1.tmp.conn_n etc.

The second input file required to run the preprocessor is a file containing a mapping between GridPro™ and TURBO boundary conditions. The file is named 'gplist.in'. A sample file is shown in figure B.2.

```
&GP_PROPS
gslip=4
gno_slip=2
gno_slip_iso=8
grad_eq_exit=6
gperiodic=999
gpressure_exit=999
gplenum_in=999
gref_clearance=999
gts=3
gcvbc_in=7
gisentropic_in=5
gwb_steady_in=999
gwb_unsteady_in=999
gwb_steady_exit=999
gwb_unsteady_exit=999
gcvbc_sub_exit=999
gcvbc_super_exit=999
gslide=999
gslide_ts_i=10
gslide_ts_j=999
ginter_blk=1
/
&This file contains the property conversion list
&values to the left are TURBO BC names
&values to the right are gridpro values that have been assigned to boundaries
&properties that are not used are assigned 999.
&You only need to sepcify periodic or ts and NOT ref_preiodic or ref_ts
&The converter figures out whether to use ref_ and fwd or bak directions
```

Figure B.2 Contents of input file gplist.in

The variables to the left of the '=' are formed by adding the prefix 'g' to a TURBO boundary condition name. The value to the right of the '=' refers to the number assigned to the boundary condition in GridPro™. Boundary conditions that are not used in a simulation are assigned the value '999'.

B.4 Examples

This section shows the usage of the preprocessor through two examples. The first uses the geometry of chapter 4 while the second uses the geometry of chapter 5.

Example 1. Flat plate with film cooling hole

The geometry for this exercise is shown in figure B.3. Flow enters the domain from the left (minimum *x* face) and exits through the right (maximum *x*). There is an additional inlet at the minimum *y* face (plenum inlet). The grey inlet patch belongs to block 8 of the 19-block grid. The blue inlet patch belongs to block 9. The grey exit patch belongs to block 11 while the red exit patch belongs to block 12. Figures B.4a and B.4b show the contents of the input files setup.in and gplist.in respectively for this case. Figure B.5 shows the log file created after running the preprocessor.

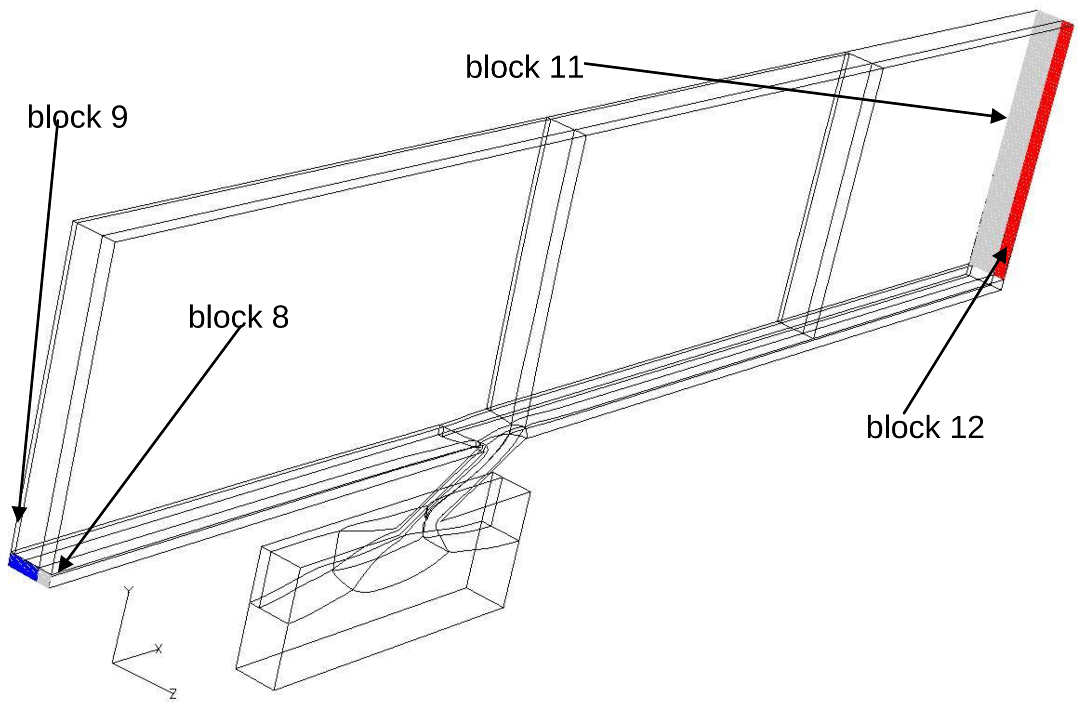

Figure B.3 Computational domain for example 1

```
&SETUP_PARAMS
num_blade_rows=1
num_blades=1
checkconn=1
conn_tol=0.0000001
turbo_friendly=.TRUE.
row_names=fine.tmp
/
```

a) setup.in

```
&GP_PROPS
gslip=4
gno_slip=2
gno_slip_iso=8
grad_eq_exit=6
gperiodic=999
gpressure_exit=999
gplenum_in=999
gref_clearance=999
gts=3
gcvbc_in=999
gisentropic_in=5
gwb_steady_in=999
gwb_unsteady_in=999
gwb_steady_exit=999
gwb_unsteady_exit=999
gcvbc_sub_exit=999
gcvbc_super_exit=999
gslide=999
gslide_ts_i=10
gslide_ts_j=999
ginter_blk=1
/
```

b) gplist.in

Figure B.4 Input parameters for example 1

```
Reading setup parameters from setup.in
Reading Setup Parameters from
setup.in

************Blade row            1  *********
Converting gridpro files to plot3d
 First read for sizes ...

 Writing number of blocks and sizes to
 fine.tmp.dat


 Now read to dump plot3d file ...
Converting conn_n to bc and dmap
         43  Block interfaces found
          0 Ref Periodics found
         50  Boundary conditions found
Verifying connectivity
Grid tolerance is set at   1.000000000000000E-007
Angle of periodicity is:   360.000000000000       degrees.
File opened succesfully
         19  Blocks found
Block#  ni   nj     nk
          1          45          69          25
          2          25          69          13
          3          13          77          45
          4          13         129          97
          5          25         129          97
          6           5         129          97
          7          45          41           5
          8          45          13          89
          9          45          29          89
         10          45          13          77
         11          97          65          29
         12          97          65          13
         13          45         193          13
         14         113          97          13
         15          45          25         217
         16         113          97          25
         17          45           5         217
         18           5          97         113
         19           5          41          17
Block #        Block extents      Block size
          1           1       77625       77625
          2       77626      100050       22425
          3      100051      145095       45045
          4      145096      307764      162669
          5      307765      620589      312825
          6      620590      683154       62565
          7      683155      692379        9225
          8      692380      744444       52065
          9      744445      860589      116145
```

Continued

Figure B.5 Output upon execution of preprocessor for example 1

Figure B.5 continued

```
         10      860590      905634       45045
         11      905635     1088479      182845
         12     1088480     1170444       81965
         13     1170445     1283349      112905
         14     1283350     1425842      142493
         15     1425843     1669967      244125
         16     1669968     1943992      274025
         17     1943993     1992817       48825
         18     1992818     2047622       54805
         19     2047623     2051107        3485
    2051107  data points will be read.
Plot3d File closed after reading
*************************************************
*****************Reading dmap.in*****************
  43
Connectivity has been verified for current row
Memory deallocation complete.
Writing GU files
Opening
 fine.tmp.p3d
                      as plot3d
         19  GU files written for BR           1 .
Combining bc and dmap files into bc.in and dmap.in
Making TURBO FRIENDLY
Blocks to change are:           8           9           11           12
         13           14           15           16           17           18
WARNING! UNABLE TO REORIENT BLOCK           8
Radial direction not detected. Manual inspection required.
WARNING! UNABLE TO REORIENT BLOCK          13
Radial direction not detected. Manual inspection required.
You should now have dmap.in, bc.in,GU files and tasklist.in(if turbo_friendly)
Creating pmap.in files for multiblock per processor options
Creating pmap files for multiblock per cpu simulations
=====================================================
Average_size|total_size|maximum_size|num_procs_recmnd
     107953     2051107      312825          7
=====================================================
 pmap.in.1.m3                                    has been created.
 pmap.in.2.m3                                    has been created.
 pmap.in.3.m3                                    has been created.
 pmap.in.4.m3                                    has been created.
 pmap.in.5.m3                                    has been created.
 pmap.in.6.m3                                    has been created.
 pmap.in.7.m3                                    has been created.
 pmap.in.1.m2                                    has been created.
 pmap.in.2.m2                                    has been created.
 pmap.in.3.m2                                    has been created.
 pmap.in.4.m2                                    has been created.
 pmap.in.5.m2                                    has been created.
 pmap.in.6.m2                                    has been created.
 pmap.in.7.m2                                    has been created.
===================End of all operations============
```

Blocks that will be

Warning because there is no radial

In figure B.5, the inlet blocks 8 and 9, and the exit blocks 11 and 12 are indicated as blocks that need to be reoriented. This is clear from looking at figure B.6 that shows an excerpt from the boundary condition file for this case.

8	2	1	1	1	1	13	89/
8	202	1	1	1	45	13	1/
8	1	1	13	1	45	13	89/
9	2	1	1	1	1	29	89/
9	1	1	1	1	45	1	89/
9	202	1	1	1	45	29	1/
10	2	1	1	1	1	13	77/
10	1	1	1	1	45	13	1/
10	1	1	13	1	45	13	77/
11	1	1	1	1	1	65	29/
11	1	1	1	1	97	65	1/
11	305	1	65	1	97	65	29/
12	1	1	1	1	1	65	13/
12	305	1	65	1	97	65	13/

a) before reorientation

8	2.00	1	1	45	89	13	45/
8	202.00	1	1	1	1	13	45/
8	1.00	1	13	1	89	13	45/
9	2.00	1	1	1	89	29	1/
9	1.00	1	29	1	89	29	45/
9	202.00	1	1	1	1	29	45/
10	2.00	1	1	1	1	77	13/
10	1.00	1	77	1	45	77	13/
10	1.00	1	1	13	45	77	13/
11	1.00	1	97	1	65	97	29/
11	1.00	1	1	1	65	97	1/
11	305.00	65	1	1	65	97	29/
12	1.00	1	97	1	65	97	13/
12	305.00	65	1	1	65	97	13/

b) after reorientation

Figure B.6 Result of block manipulation by preprocessor for example 1

Here, the first column refers to the block number and the second column is the boundary condition. Boundary condition number 202 is an inlet boundary and 305 is an exit boundary. The remaining columns are extents of the boundary within the block given in the order '*is js ks ie je ke*' [43]. The reoriented blocks have *is*=*ie* for the inlet and exit boundaries. This shows that they are at *i* faces. The inlets are at i_{min} faces while the exits are at i_{max} faces. The plenum boundary is not in the axial direction and must therefore be reoriented manually using a module of the preprocessor. The user provides the block number and the type of operation to perform as input to the reorientation module. The warning messages in figure B.5 are expected for this case because there is no radial direction. At the end of the output shown in figure B.5 a list of files with the prefix 'pmap' are shown to be generated. These files contain a schedule to allow multiple blocks to run in parallel on a single processor. Figure B.7 shows the contents of file 'pmap.report' that summarizes the contents of the files.

```
**********Using Method 3***********
====================================================
Load distribution for num_procs=        1
Processor        1  has size    2051107  and       19  blocks
Total blocks assigned =        19
Percentage diff between largest and smallest:   0.000000000000000E+000
====================================================
Load distribution for num_procs=        2
Processor        1  has size    1076385  and        5  blocks
Processor        2  has size     974722  and       14  blocks
Total blocks assigned =        19
Percentage diff between largest and smallest:   9.44485476850755
====================================================
Load distribution for num_procs=        3
Processor        1  has size     703240  and        4  blocks
Processor        2  has size     715009  and        5  blocks
Processor        3  has size     632858  and       10  blocks
Total blocks assigned =        19
Percentage diff between largest and smallest:   11.4895057265013
====================================================
Load distribution for num_procs=        4
Processor        1  has size     518095  and        3  blocks
Processor        2  has size     527375  and        3  blocks
Processor        3  has size     537697  and        5  blocks
Processor        4  has size     467940  and        8  blocks
Total blocks assigned =        19
Percentage diff between largest and smallest:   12.9732916493862
====================================================
Load distribution for num_procs=        5
Processor        1  has size     428970  and        2  blocks
Processor        2  has size     416518  and        2  blocks
Processor        3  has size     430455  and        3  blocks
Processor        4  has size     429329  and        5  blocks
Processor        5  has size     345835  and        7  blocks
Total blocks assigned =        19
Percentage diff between largest and smallest:   19.6582685762739
====================================================
Load distribution for num_procs=        6
Processor        1  has size     357870  and        2  blocks
Processor        2  has size     355990  and        2  blocks
Processor        3  has size     357030  and        2  blocks
Processor        4  has size     358224  and        4  blocks
Processor        5  has size     358688  and        4  blocks
Processor        6  has size     263305  and        5  blocks
Total blocks assigned =        19
Percentage diff between largest and smallest:   26.5921915425105
====================================================
Load distribution for num_procs=        7
Processor        1  has size     312825  and        1  blocks
Processor        2  has size     296450  and        2  blocks
Processor        3  has size     306690  and        2  blocks
Processor        4  has size     311700  and        4  blocks
Processor        5  has size     305162  and        2  blocks
Processor        6  has size     272495  and        3  blocks
Processor        7  has size     245785  and        5  blocks
Total blocks assigned =        19
Percentage diff between largest and smallest:   21.4305122672421
****************************************************
********************Using Method 2******************
....................................................
```

Best option

Figure B.7 Excerpt from pmap.report scheduling file

Example 2. OSU HPT

The geometry used in this example was utilized in the work reported on in chapter 5. Figure B.8 shows the blocks in this grid. The blue mesh represents the sliding interface boundary for the stator. The green and red meshes are periodic (time shift in this case) with each other.

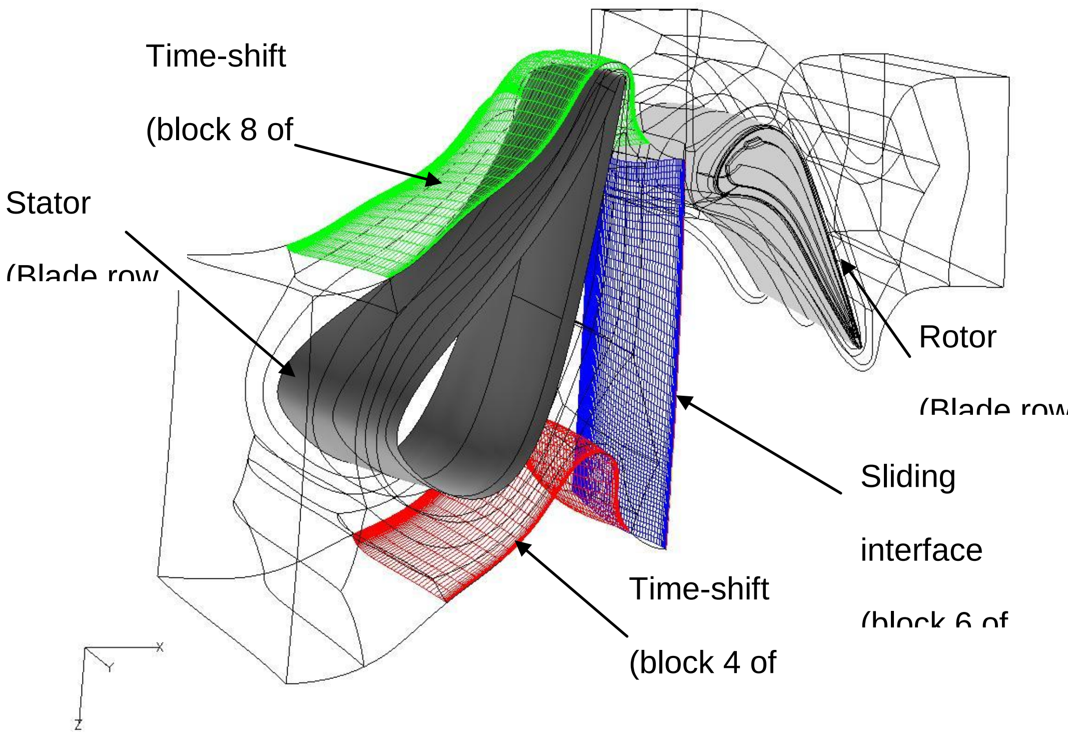

Figure B.8 Computational domain for example 2

Figure B.9 shows the contents of the input files for this example. There are now two blade rows in the input file and the blade count of each row is used to verify the connectivity of the time-shift (tangential) boundaries by calculating the angle through which a tangential boundary must be rotated to match its partner.

```
&SETUP_PARAMS
num_blade_rows=2
num_blades=38 72
checkconn=1
conn_tol=0.000001
turbo_friendly=.TRUE.
row_names= stator.tmp rotor.tmp
/
```

a) setup.in

```
&GP_PROPS
gslip=4
gno_slip=2
gno_slip_iso=8
grad_eq_exit=6
gperiodic=999
gpressure_exit=999
gplenum_in=999
gref_clearance=999
gts=3
gcvbc_in=999
gisentropic_in=5
gwb_steady_in=999
gwb_unsteady_in=999
gwb_steady_exit=999
gwb_unsteady_exit=999
gcvbc_sub_exit=999
gcvbc_super_exit=999
gslide=999
gslide_ts_i=10
gslide_ts_j=999
ginter_blk=1
/
```

b) gplist.in

Figure B.9 Input parameters for example 2

The log file from executing the preprocessor is shown in figure B.10. Due to the existence of multiple rows in this example, the interface file 'turbo.in' is also populated with necessary information [43]. Figure B.11 shows the results of reorienting the blocks to satisfy TURBO specifications that are listed in section 1.5 of chapter 1.

```
Reading setup parameters from setup.in
Reading Setup Parameters from
setup.in

************Blade row            1  *********
Converting gridpro files to plot3d
 First read for sizes ...

 Writing number of blocks and sizes to
 stator.tmp.dat


 Now read to dump plot3d file ...
Converting conn_n to bc and dmap
         34  Block interfaces found
          2 Ref Periodics found
         47  Boundary conditions found
Verifying connectivity
Grid tolerance is set at   1.000000000000000E-006
Angle of periodicity is:   9.47368421052632       degrees.
File opened succesfully
         11  Blocks found
Block#  ni   nj     nk
          1          67          27          109
          2         109          85           67
          3         109          17           67
          4           5         127           33
          5          17         127           17
          6           9         127           57
          7          13         127            9
          8          41         127            5
          9           5         127           57
         10          45         127            9
         11           5         127          109
Block #        Block extents       Block size
          1           1      197181       197181
          2      197182      817936       620755
          3      817937      942087       124151
          4      942088      963042        20955
          5      963043      999745        36703
          6      999746     1064896        65151
          7     1064897     1079755        14859
          8     1079756     1105790        26035
          9     1105791     1141985        36195
         10     1141986     1193420        51435
         11     1193421     1262635        69215
    1262635  data points will be read.
Plot3d File closed after reading
*************************************************
****************Reading dmap.in*****************
  34
Connectivity has been verified for current row
```

Continued

Figure B.10 Output upon execution of example 2

Figure B.10 continued

```
Memory deallocation complete.
Writing GU files
Opening
 stator.tmp.p3d
                      as plot3d
         11  GU files written for BR            1 .
************Blade row            2  *********
Converting gridpro files to plot3d
 First read for sizes ...

 Writing number of blocks and sizes to
 rotor.tmp.dat


 Now read to dump plot3d file ...
Converting conn_n to bc and dmap
         74  Block interfaces found
          3 Ref Periodics found
         55  Boundary conditions found
Verifying connectivity
Grid tolerance is set at   1.000000000000000E-006
Angle of periodicity is:   5.00000000000000       degrees.
File opened succesfully
         17  Blocks found
Block#  ni   nj     nk
          1          13         107          25
          2          17         107          37
          3          49         107           9
          4          17         107          17
          5          77          60           9
          6          61          60           9
          7           9          28         161
          8         107           5          89
          9           5          60           9
         10          13          33         161
         11           5         107          65
         12         161          33           9
         13          81         107          13
         14         161          37          68
         15         161          37          17
         16          28          13         161
         17         107          33          57
Block #        Block extents       Block size
          1           1       34775       34775
          2       34776      102078       67303
          3      102079      149265       47187
          4      149266      180188       30923
          5      180189      221768       41580
          6      221769      254708       32940
          7      254709      295280       40572
          8      295281      342895       47615
          9      342896      345595        2700
```

Continued

Figure B.10 continued

```
         10      345596      414664       69069
         11      414665      449439       34775
         12      449440      497256       47817
         13      497257      609927      112671
         14      609928     1015003      405076
         15     1015004     1116272      101269
         16     1116273     1174876       58604
         17     1174877     1376143      201267
    1376143  data points will be read.
Plot3d File closed after reading
*************************************************
*****************Reading dmap.in*****************
  74
Connectivity has been verified for current row
Memory deallocation complete.
Writing GU files
Opening
 rotor.tmp.p3d
                      as plot3d
         17  GU files written for BR            2 .
Combining bc and dmap files into bc.in and dmap.in
Making TURBO FRIENDLY
Blocks to change are:           4           8           6           7
         10          19          22          13          14          24
         12          28
writing turbo.in
You should now have dmap.in, bc.in,GU files and tasklist.in(if turbo_friendly)
Creating pmap.in files for multiblock per processor options
Creating pmap files for multiblock per cpu simulations
=====================================================
Average_size|total_size|maximum_size|num_procs_recmnd
      94242     2638778      620755           5
=====================================================
 pmap.in.1.m3                                     has been created.
 pmap.in.2.m3                                     has been created.
 pmap.in.3.m3                                     has been created.
 pmap.in.4.m3                                     has been created.
 pmap.in.5.m3                                     has been created.
 pmap.in.1.m2                                     has been created.
 pmap.in.2.m2                                     has been created.
 pmap.in.3.m2                                     has been created.
 pmap.in.4.m2                                     has been created.
 pmap.in.5.m2                                     has been created.
===================End of all operations============
```

4	-106	1	1	1	1	127	33/
8	-107	9	1	1	41	127	1/
4	2	1	1	1	5	1	33/
4	2	1	127	1	5	127	33/
5	2	1	1	1	17	1	17/
5	2	1	127	1	17	127	17/
6	402	1	1	1	1	127	57/
6	2	1	1	1	9	1	57/
6	106	1	101	1	5	127	1/
6	107	1	101	57	5	127	57/
6	106	1	85	1	5	101	1/

a) before reorientation

4	-102.00	1	1	5	33	127	5/
8	-102.00	9	1	1	41	127	1/
4	2.00	1	1	1	33	1	5/
4	2.00	1	127	1	33	127	5/
5	2.00	1	1	1	17	1	17/
5	2.00	1	127	1	17	127	17/
6	402.00	9	1	1	9	127	57/
6	2.00	1	1	1	9	1	57/
6	102.00	5	101	57	9	127	57/
6	102.00	5	101	1	9	127	1/
6	102.00	5	85	57	9	101	57/

b) after reorientation

Figure B.11 Result of block manipulation by preprocessor for example 2

Looking at figure B.11, it is clear that the tangential boundaries on blocks 4 and 8 have been placed on *k* faces in accordance to TURBO specifications. The boundary types -106 and -107 that are applicable to any computational coordinate face (*i,j,k*) are changed to boundary type -102 that only deals with the time-shift boundary condition on a *k*-face. The sliding interface on block 6 has been placed on an i_{max} face.

These examples have shown the functionality of the preprocessor. There are several independent utilities that have also been developed to perform various operations on grids. Future work would include the integration of these utilities into the preprocessor and the creation of Graphical User Interface to make the preprocessor more user friendly.

Appendix C: Comparison of Turbulence Models

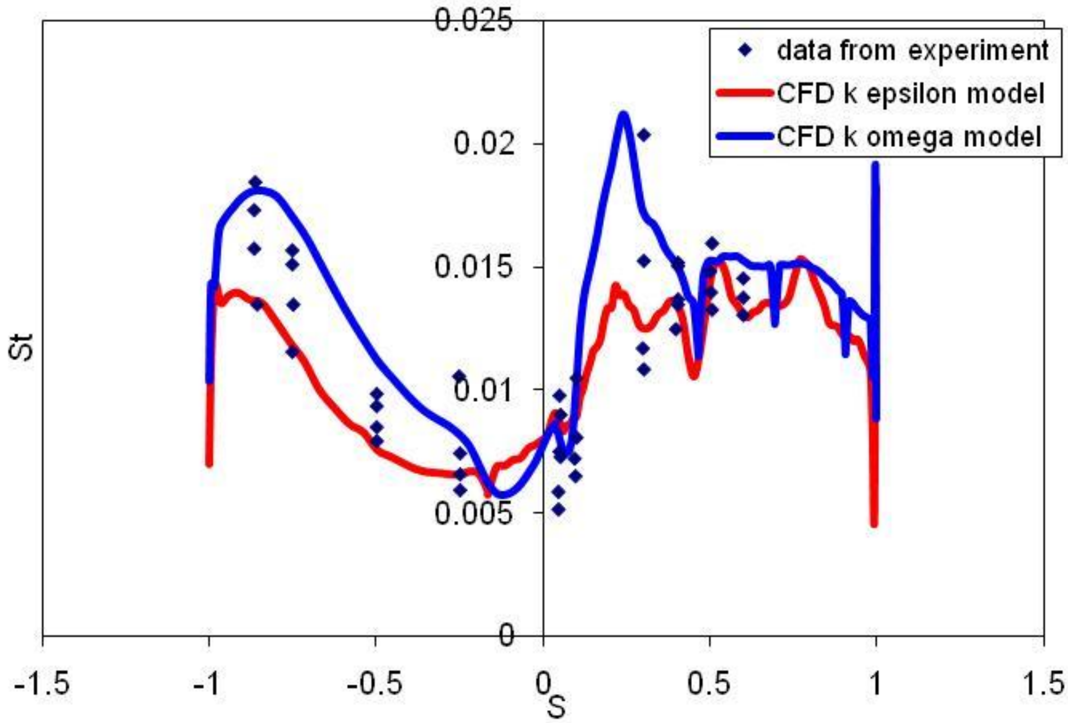

Figure C.1 Comparison of turbulence models for stator geometry of OSU HPT

Figure C.1 shows Stanton number profiles at the mid-span of the Stator geometry described in Chapter 5. Results are shown for the two turbulence models available in TURBO: k-ω (blue) [39] and k-ε (red) [24]. The discrete points are Stanton numbers obtained from experiment [18]. The abscissa is normalized distance along the stator mid-span section. The k-ε model is found to better fit the experiment and does not overshoot the Stanton number value near the leading edge unlike the k-ω model. While both models lie within the range of experimental sampling, the k-ω model is known to over predict heat transfer and mixing in regions of large acceleration and high strain rate.